

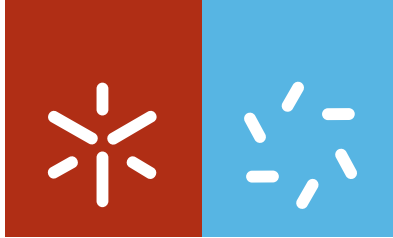
Universidade do Minho

Escola de Ciências

Emílio Sérgio Marins Vieira Pinto

Células solares e sensores de filme fino de silício depositados sobre substratos flexíveis

maio 2014



Universidade do Minho

Escola de Ciências

Emílio Sérgio Marins Vieira Pinto

Células solares e sensores de filme fino de silício depositados sobre substratos flexíveis

Programa Doutoral em Física (MAP-fis)

Trabalho realizado sob a orientação do

Doutor João Pedro dos Santos Hall Agorreta Alpuim

maio 2014

DECLARAÇÃO

Nome

Emílio Sérgio Marins Vieira Pinto

Endereço electrónico: es.marins@gmail.com

Título:

Células solares e sensores de filme fino de silício depositados sobre substratos flexíveis

Orientador(es):

Doutor João Pedro dos Santos Hall Agorreta Alpuim

Ano de conclusão: 2014

Designação do Doutoramento:

Doutoramento em Física

É AUTORIZADA A REPRODUÇÃO INTEGRAL DESTA TESE APENAS PARA EFEITOS DE INVESTIGAÇÃO,
MEDIANTE DECLARAÇÃO ESCRITA DO INTERESSADO, QUE A TAL SE COMPROMETE;

Universidade do Minho, 16/05/2014

Assinatura:

Emílio Sérgio Marins V. Pinto

STATEMENT OF INTEGRITY

I hereby declare having conducted my thesis with integrity. I confirm that I have not used plagiarism or any form of falsification of results in the process of the thesis elaboration.

I further declare that I have fully acknowledged the Code of Ethical Conduct of the University of Minho.

University of Minho, _____

Full name: Emílio Sérgio Martins Vieira Pinto

Signature: Emílio Sérgio Martins V. Pinto

Acknowledgements

First of all I thank my supervisor, Professor Pedro Alpuim, for the opportunity to do my PhD work in his group. I am very grateful for everything I have learned with him during the daily work and for his unflagging attitude to keep me motivated. More than that, his example of dedication to the work, discipline, competence and enthusiasm are things that I will take with me for my whole life!

I also thank Dr. Friedhelm Finger for the opportunity to complete this research at Forschungszentrum Jülich (IEK-5), where, besides enjoying the pleasant and cooperative work atmosphere, I have learned intensively under his careful and competent supervision.

I would like to thank all the colleagues and technicians that have helped in this work, at UM and IEK-5. Starting with the professors from the Department of Physics (UM): Luís Rebouta, for the TCO depositions; Carlos Tavares, for allowing the transmittance and reflectance measurements; Fátima Cerqueira, for the valuable help with the measurements and analysis of Raman and transmittance spectroscopy and Senentxu Lanceros-Mendez for supporting the characterization of the piezoresistive sensors. From IEK-5 I would like to acknowledge A. Schmalen, J. Wolff, M. Hülsbeck and W. Reetz for the technical support, A. Doumit, J. Worbs and H. Siekmann for the depositions of the front and back contacts, and my colleagues Stephan Michard, Tao Chen and Marek Warzecha for helping me with the depositions at CT2. Also, thanks to prof. Stefano Chiussi and Stefan Stefanov, from University of Vigo, for the laser treatment of plastic substrates.

To my friends from Jülich: Björn, Carolin, Damian, David, Elif, Etienne, Gaye, Gokhan, Hang, Jonas, Jorj, Juri, Kaining, Lihong, Marek, Max, Olga, Sacha, Ümit, Wanjiao, and all the others that I may have forgotten. Thank you all for the great moments we had together! Your companionship and friendship have made my stay in Jülich an unforgettable time!

Finally, thanks to my parents and sisters for all the support, love and encouragement, which were always present during all these years, despite the physical distance.

Título

“Células solares e sensores de filme fino de silício depositados sobre substratos flexíveis”

Resumo

Células solares flexíveis de filmes finos de silício são geralmente fabricadas a baixa temperatura sobre substratos de plástico ou a mais elevadas temperaturas sobre folhas de aço. Esta tese reporta o estudo da deposição de filmes finos sobre diferentes substratos de plástico, transparentes e coloridos, para células solares do tipo sobrestrato e substrato, respectivamente. Como objetivo co-lateral, os filmes dopados depositados sobre plástico foram usados como sensores de deformação, utilizando as suas propriedades piezo-resistivas.

Elevadas taxas de deposição dos filmes de silício depositados sobre plástico foram obtidas a baixa temperatura do substrato (150°C) por rf-PECVD. A influência de diferentes parâmetros de deposição sobre as propriedades e taxa de deposição dos filmes resultantes foram estudados e correlacionados.

Células solares de filmes finos de silício amorfo e microcristalino foram desenvolvidas a baixas temperaturas sobre plásticos. Eficiências de 5 – 6.5% foram alcançadas para as células amorfas e 7.5% para as células microcristalinas. Efeitos de aprisionamento da luz foram estudados através da texturização por ablação laser de substratos de plástico e corrosão úmida de TCO sobre plástico.

Filmes finos de silício microcristalino, depositados por HW-CVD, com fator piezoresistivo de -32.2, foram usados para fabricar sensores de deformação em uma membrana plástica muito fina (15 µm). Estruturas de teste em têxtil e a miniaturização dos sensores piezoresistivos depositados sobre substratos flexíveis de poliimida foram abordados.

Title

“Thin-film silicon solar cells and sensors deposited on flexible substrates”

Abstract

Flexible thin film silicon photovoltaics are usually done on low temperature plastic substrates or on stainless steel foil. This thesis reports on the study of thin film deposition on different plastic substrates, both transparent and colored, for superstrate and substrate solar cells, respectively. Some of the optimized doped layers deposited on plastics were used as strain gauges based on their piezo-resistive properties.

High-rate deposited silicon films on plastic were achieved at low substrate temperature (150°C) by standard Radio-frequency (13.56 MHz) Plasma Enhanced Chemical Vapor Deposition (rf-PECVD). The influence of different deposition parameters on the resulting film properties and deposition rate were studied and correlated.

Thin film silicon solar cells were developed at low temperatures on plastics. Efficiencies of 5 – 6.5% were achieved for amorphous cells deposited by rf-PECVD, and 7.5% for microcrystalline cells deposited at Very High Frequency (81.36 MHz) Plasma Enhanced Chemical Vapor Deposition (VHF-PECVD). Light trapping effects were studied by laser texturing of plastic substrates and wet etching of Transparent Conductive Oxide (TCO) on plastic.

Microcrystalline silicon thin films, prepared by hot-wire chemical vapor deposition, with a piezoresistive gauge factor of -32.2, were used to manufacture a thin *skin-like* piezo-resistor strain-sensing membrane. Test structures on textile and the miniaturization of the piezoresistive sensors deposited on flexible polyimide substrates were addressed.

Contents

1 Introduction	1
1.1 Photovoltaics and thin-film silicon solar cells.....	1
1.2 Piezoresistive sensors	12
1.3 Plastic substrates.....	14
1.4 Organization of the thesis	15
References	18
2 Experimental Techniques.....	23
2.1 Plasma Enhanced Chemical Vapor Deposition	23
2.2 Hot-Wire Chemical Vapor Deposition	30
2.3 CVD deposition systems	34
2.4 Optical transmittance spectroscopy	38
2.5 Structural and chemical characterization.....	42
2.6 Electrical Material Characterization	44
2.7 Solar Cell Characterization.....	48
2.8 Piezoresistance	51
References	53
3 High-rate deposition of microcrystalline silicon thin films on plastics	55
3.1 Introduction	56
3.2 Experimental details	57
3.3 Structural properties	58
3.4 Deposition rate.....	60
3.5 Opto-electronic properties	61
3.6 Doping	63
3.7 Conclusions	66
References	67
4 Amorphous silicon solar cells on flexible substrates	69

4.1 Introduction	70
4.2 Experimental details	70
4.3 Doped ZnO films	72
4.4 p-i-n superstrate solar cells on PEN	74
4.5 n-i-p substrate solar cells on PI	76
4.6 Laser texturing of PET substrates.....	78
4.7 Conclusions	85
References	86
5 Microcrystalline silicon solar cells on flexible PI substrate.....	87
5.1 Introduction	88
5.2 Experimental details	88
5.3 n-i-p solar cells on smooth PI substrate.....	90
5.4 n-i-p solar cells on PI with textured ZnO:Ga	92
5.5 Conclusions	94
References	95
6 Shape sensors based on piezoresistive doped $\mu\text{c-Si:H}$	97
6.1 Introduction	98
6.2 Experimental details	99
6.3 <i>skin-like</i> piezoresistive sensing membranes	103
6.4 Test structures for smart textiles.....	105
6.5 Sensor array fabrication.....	108
6.6 Conclusions	109
References	111
7 Conclusions	113
7.1 High-rate deposition of silicon thin films on plastics.....	113
7.2 Flexible thin film silicon solar cells	114
7.3 Flexible $\mu\text{c-Si:H}$ piezoresistive sensors	115

Chapter 1

1 Introduction

1.1 Photovoltaics and thin-film silicon solar cells

Photovoltaics (PV) is a fascinating field, that requires a multidisciplinary understanding of the direct conversion of sunlight to electricity, the photovoltaic effect. Photovoltaics, technically, holds the potential to fulfill the energy needs of humanity by using only renewable solar energy, but it is also controversial and detractors have argued that the manufacture of large-area low-cost semiconductor panels is virtually an impossible task. They now appear to have been wrong, as solar PV electricity at a few cents per kWh has proved to be a realistic target in sunny areas. This opens bright perspectives for producing a substantial part of our electricity needs with PV [1].

The last decade has been particularly exciting for the field of photovoltaics, with the global photovoltaic market growing at a dizzying pace. The production volume increased every year by 40 to 70% over the last decade [2]. This strong growth was stimulated by the perspective of short-term profit on markets with high feed-in tariffs; but once these tariffs started to decrease, PV industry showed that manufacturing costs could be decreased significantly year after year; the perception that green technologies will play an increasingly important role in a society plagued by excessive consumption of fossil fuels and faced with major climatic changes induced by human activity [1].

Until now, crystalline silicon (c-Si) PV technology, based on single crystal or polycrystalline silicon wafers, has dominated the photovoltaic market, with 88 % of the cell and module production in 2008 [2], and will probably continue to do so for several more years. This technology has benefited indirectly from past research and investments made by the semiconductor industry and, considered globally, it can be regarded as robust and reliable. However, although the prices of polysilicon and silicon have

dropped significantly in recent years, c-Si PV technology involves high energy and labor inputs which make it difficult for any significant progress in reducing production costs in the short term to occur [3]. Moreover, the growth of the crystalline silicon solar cell industry was limited by the availability of the so-called “Si feedstock” or purified polysilicon [4]. Indeed from 2005 onwards the PV industry has been using more purified polysilicon than the semiconductor industry.

This lack of purified silicon was one of the important factors that opened up a window of opportunity for thin-film PV technologies, which requires much less usage of active material, as layers with thicknesses of only a few hundreds of nanometers or a few micrometers are used, and the total number of processing steps is strongly reduced compared to the full production chain for crystalline silicon. This gives the prospect of very low production costs and significantly lower energy pay back times [5,6]. In addition, the more aesthetic aspect of thin-film modules and the possibility of manufacturing flexible, unbreakable modules, open up a full range of new PV solutions. The major challenge of manufacturing low-cost thin-film solar modules has been the up-scaling of lab processes to real “mass production” [1].

The “classical” thin-film PV technologies can be grouped in three large categories, based on different active absorber materials: copper-indium-gallium-selenide (CIGS) and variations thereof, cadmium telluride (CdTe) and, finally, hydrogenated amorphous silicon (a-Si:H)/microcrystalline silicon (μ c-Si:H) and their alloys.

Solutions based on the use of chalcopyrites (CIGS and derived compounds) are attractive because of their record efficiencies achieved. They are, at the laboratory scale, close to those of crystalline silicon. One of the major challenges is to control properly the deposition of the quaternary alloy used as absorber material in a reproducible way under mass production conditions. Also, for very large production volumes, indium availability might become a concern. Cadmium telluride technology also benefits from the medium to high efficiencies achieved at the laboratory scale and has the advantage of the very fast and relatively “easy” deposition techniques used for the CdTe absorber. Concerns about the availability of Te as well as acceptance issues linked to an intensive use of a cadmium-containing compound could become critical factors for this technology. Finally, thin-film silicon technologies (amorphous silicon, SiGe alloys, microcrystalline silicon), even though they have not so far demonstrated similarly high efficiencies at the laboratory scale, they do have the advantage of plentiful raw material supply (Si and Sn or Zn in the simplest version of a single-junction solar cell with SnO_2

or ZnO contact layers), what is essential for a market size reaching several hundred GW of PV modules annually. In such a context, thin-film silicon technology is currently the only option sustainable in the long run among the proven thin-film PV technologies [7], and will most likely play a key role, as it is today the only technology combining the advantage of virtually infinite resources with low material usage. Other reasons for the uniqueness of thin-film silicon are: (1) the basics are well established: this includes the control of doping levels, as well as reproducible fabrication processes for depositing device-quality layers; (2) no hazardous materials (such as Cd or Pb) are required in thin-film silicon technology, making it, if not safer, at least free from acceptance problems and/or regulatory risks; (3) the low temperature coefficient of down to $-0.2\ \%/^{\circ}\text{C}$ and the self-annealing effect of the amorphous silicon material should ensure that, for high module operating temperatures, the annual energy yield is superior by 5 to 10 % when compared to other types of thin-film or crystalline-silicon modules; finally, (4) a strong synergy with another industrial sector, the flat panel display industry, is present [1].

As a technology, a-Si:H based device fabrication has already proved to be mature enough to meet all industry demands. The history of thin-film silicon technology started over 30 years ago, with the fabrication of the first thin-film silicon solar cell based on a-Si:H [8]. Since then, research and development (R&D) efforts have led to single- and multi-junction solar cells and large-area modules based on a-Si:H and related alloys.

The demonstration in the mid 90's of a complete microcrystalline silicon cell made by very high-frequency (VHF) plasma enhanced chemical vapour deposition (PECVD) with an efficiency of 4.6% opened up a new area of photovoltaic development [9]. However, cell efficiencies were limited by low open circuit voltages and fill factors. The main advantage of these cells is the stability to light soaking and a better long wavelength response, when compared to a-Si:H cells. However, improvement in the efficiency of the single junction and application as a bottom cell in a tandem concept – a double junction consisting of a top a-Si:H cell and a bottom $\mu\text{c-Si:H}$ cell – which showed an initial efficiency of 13%, looked like a breakthrough in the low temperature process [10]. A quick adaptation of this concept and its translation into industrial production by Kaneka Corporation has established the technological viability of this low temperature process. This rapid adaptation was possible due to the maturity of the amorphous silicon technology, including the back reflector, the transparent conductive oxide (TCO), monolithic integration and encapsulation.

If the gases used for deposition of amorphous silicon are highly diluted in hydrogen, the deposit consists of regions of crystalline silicon immersed in an amorphous matrix [11]. This two phase material is known as “microcrystalline silicon” or sometimes as “nanocrystalline silicon”. The optical properties of the material resemble those of crystalline/polycrystalline silicon rather than amorphous silicon, hence it has utility in developing hybrid amorphous Si/microcrystalline Si tandem solar cells and modules (referred in the literature as ‘micromorph devices’), as described above. Trials indicate that these hybrid devices and modules rival triple-junction amorphous silicon in terms of efficiency and stability [12]. Furthermore, these solar cells deposited on flexible substrates, such as plastic and stainless steel sheets, have received much attention, because they combine quality and high efficiency of silicon thin-films and the flexibility, versatility and low cost of flexible substrate in-line deposition technology.

1.1.2 Basic principles and structure of thin-film silicon solar cells

The electronic defect density plays a crucial role in amorphous and microcrystalline thin film silicon-based devices. The metastable defects are believed to be dangling bonds formed by breaking weak Si-Si bonds in the random network. Doped layers contain much more defects than intrinsic layers (several orders of magnitude higher), giving rise to a peculiar doping mechanism identified for the first time by R. Street [13], called compensation, which will be discussed in section 3.6. Because of the very high dangling bond concentration in doped films, only intrinsic layers can be used as an absorber material [14]. Moreover a-Si:H suffers degradation upon exposure to sunlight because of a phenomenon known as the Staebler-Wronski effect [15], which causes a large increase in defect density.

Charge carrier mobility in amorphous silicon is much lower than in crystalline silicon, due to the amorphous random network which increases the number of scattering events when electrons or holes try to move by drift or diffusion. As a result of the low carrier mobility and low lifetime, collection cannot take place through diffusion. A strong drift field is an absolute requirement. This is achieved by sandwiching the intrinsic absorber layer between doped layers with opposite doping, thus increasing the width of the space-charge region. The doping level of the contacts and the thickness of the i-layer must be such that the entire i-layer is under depletion. As most of the

generation takes place close to the top surface and the hole mobility is much lower than electron mobility in a-Si:H, the device structure always features a p-doped layer on top, the side through which light enters the i-layer, while the bottom layer is n-doped. Indeed, in this way, most of the holes are generated close to the p-contact where they are majority carriers and no longer can recombine. In these structures the p-type layer is also called the window layer. Holes generated deeper in the i-layer have a higher probability of recombining and, therefore, a lower collection probability at the contacts. In contrast, electrons have a higher collection probability at the n-contact, after drifting throughout the i-layer. Due to the very low carrier lifetime in doped layers, all light absorbed in the p-layer is lost for conversion. To minimize this effect, not only the p-layer is kept very thin (~ 10 nm), but C can also be added so that the bandgap increases and the absorption decreases.

The device structures of amorphous silicon solar cells and microcrystalline silicon solar cells are very similar. Both, superstrate and substrate configurations are possible. Superstrate means that the light enters the solar cell through the supporting substrate, which requires a highly transparent substrate material and the presence of a transparent conductive oxide between the substrate and the active layer, usually, indium tin oxide (ITO), tin oxide (SnO_2), or Al and Ga doped zinc oxide (ZnO:Al/Ga) to collect the current from the positive contact. ITO is highly transparent and conductive but it is not very stable in the presence of atomic hydrogen generated during Si deposition from SiH_4 and H_2 , it uses In, a relatively rare element, as discussed above, and it is relatively expensive. Therefore, solutions based on SnO_2 or ZnO are preferred [14]. This configuration is also called p-i-n solar cell, referring to the sequence in which the different layers are deposited. The other option is to make cells in substrate configuration which enables the use of a wider range of substrate materials, since they do not need to be transparent. In this case, the optimized cell structure is an n-i-p configuration, for the reasons stated above.

The intrinsic layer thickness has to be chosen based on the mobility lifetime ($\mu\tau$) product after light-soaking. If the layer is too thick, part of it will not stay in the depletion condition and there will be large collection losses because holes generated deep in the layer recombine before being collected. If the layer is thinner, the distance to be covered before collection is shorter, and the electric field is stronger since the entire layer is depleted. Both effects have a positive impact on carrier collection. However, a thin layer implies that a large fraction of the light does not get absorbed, but is lost

through transmission or escape reflection. There is, therefore, an optimal thickness, which is around 300 nm for an amorphous i-layer, and thinner if efficient light-trapping schemes are used.

Similar consideration apply in the case of $\mu\text{c-Si:H}$ solar cell design. However, the optimal thickness of the microcrystalline i-layer is much larger than that for amorphous silicon cells, from 1 to 2 μm , due to the indirect bandgap of $\mu\text{c-Si:H}$ leading to a much lower absorption coefficient in the visible. But since the $\mu\tau$ product is much higher and there is much less or no light-induced degradation in $\mu\text{c-Si:H}$, the thickness of the i-layer can be increased without compromising the collection efficiency. In order to reach high energy-conversion efficiencies, the TCO is usually textured in order to increase the optical path in the cell. This is either the result of the natural morphology induced by the TCO deposition, or is achieved by subsequent etching [14].

It is possible to absorb the solar spectrum more efficiently and to improve cell efficiency by using multiple junction structures with different energy bandgap i-layers to produce double junction or triple junction structures.

Multijunction thin-film silicon solar cells consist in stacking two (tandem) or even three (triple) junction structures on top of each other, the different subcells being connected in series. This concept has the potential to increase device performance well beyond that of single junction devices, particularly when the materials are selected so as to better exploit the solar spectrum. Indeed, if a high bandgap material is used for the top cell, less thermalization losses will occur as a result of absorption of high energy photons. The longer wavelength photons, which are not absorbed in the top cell, are more efficiently absorbed in the bottom cell which consists of a lower bandgap material. Moreover the fraction of unused photons from the spectrum is lower for tandem cells as the cut-off wavelength is given by the optical bandgap of the lowest bandgap material. Whereas a-Si:H has a typical bandgap of 1.75 eV and absorbs mostly visible light, $\mu\text{c-Si:H}$ has a bandgap of 1.1 eV and absorbs also the near-infrared light.

There are different types of multijunction thin-film silicon solar cells, depending on the chosen configuration and layer type. In Figure 1.1, we show two structures of particular interest.

The structure in Figure 1.1(a) is that of a “micromorph” solar cell, also called “hybrid” solar cell. It is a device in superstrate configuration (sun light incident through the substrate), with an amorphous silicon top cell and a microcrystalline silicon bottom cell. The substrate is a TCO covered glass substrate. This combination was first

proposed by IMT [16] and is now regarded as one of the most promising concepts for thin-film solar modules. In Figure 1.1(b), a triple junction solar cell in substrate configuration is represented with an amorphous silicon top cell, an amorphous SiGe middle cell, and a microcrystalline silicon bottom cell. There is a large freedom concerning the substrate because it needs neither to be transparent nor to act as a front cover. A popular choice is a stainless steel foil, which is inexpensive and flexible, and which resists relatively high temperatures. An inconvenience is that it is conductive and is, therefore, ill-suited for a monolithic module concept. The substrate is usually covered by a metal layer with high reflection, such as a silver layer. The US company United Solar Ovonic was the first to commercialize triple-junction solar cells on flexible substrates. In parallel, several other companies started pilot lines for flexible modules based on amorphous silicon (e.g. VHF-Technologies, Powerfilm).

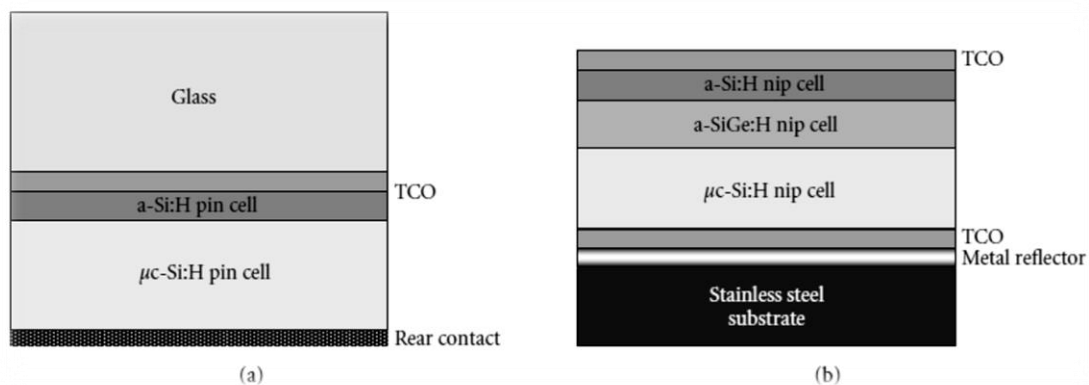


Figure 1.1: Schematic drawing of two types of tandem thin-film Si solar cells: (a) a “micromorph” or “hybrid” a-Si:H/ μ m-Si:H tandem cell, (b) a triple junction a-Si/a-SiGe:H/ μ c-Si:H solar cell.

To connect the cells in series, good tunnel junctions are required, which demands a good control of the doping level of the doped layers. Another crucial aspect is current matching. One has to ensure that all subcells have about the same short-circuit current density; otherwise, the subcells will operate far from their maximum power points, leading to large losses. In the subcell optimization, one has to take light induced degradation of the top cell into account. Indeed, the currents have to match after light-soaking, unless one only aims at a top initial efficiency.

1.1.3 Progresses and technological challenges in thin-film silicon solar cells on flexible substrates

As known, one of the targets of the PV industry is to reach grid parity, which is the point where electricity from PV origin will cost the same price as the electricity produced by conventional, non-renewable sources. To this, it is necessary to obtain higher conversion efficiency, while reducing the materials and production costs. There are many technological challenges, and several progresses have been achieved. In this section, we discuss one of the ways that show more promise to effectively cut costs which is fabrication of thin-film silicon solar cells on inexpensive flexible substrates.

Flexible substrates enable roll-to-roll rather than batch processes. An obvious low-cost choice of substrates would thus be plastic ones. However, the challenge of depositing thin-film silicon cells on plastic substrates is intrinsically linked to the maximum temperature that these substrates can endure. Therefore, another popular choice is the stainless steel foil, which is also inexpensive and flexible, and which survives higher working temperatures. Indeed, for the application of amorphous and microcrystalline films on flexible substrates, and to avoid incorporation of impurities from substrates and underlying layers, the process temperature has to be significantly reduced.

Unfortunately, the critical temperatures related to these two technologies (plastics and a-Si:H) make their simultaneous use difficult, as the properties of amorphous silicon when deposited by plasma enhanced chemical vapour deposition (PECVD), degrade dramatically near the softening temperatures of plastics. For example, the dangling bond density of a-Si:H (which can be strongly correlated to the efficiency of the solar cell) increases by an order of magnitude for each 50°C when descending below 200°C [19]. In this aspect, the growth temperature can be significantly reduced by using halogenated silane. This has been shown with the use of chlorinated silane source gases such as SiH₂Cl₂, SiHCl₃, and SiCl₄ with hydrogen dilution [17]. The dilution of SiF₄+H₂ in the plasma with He gas is shown to improve crystallinity and entirely microcrystalline films have been made by PECVD at a low substrate temperature of 120°C [18]. However, a high atomic hydrogen flux supplied to the surface of the growing film, is so far the most effective way of obtaining low-defect density amorphous silicon and high crystallinity at a low substrate temperature. Alpuim *et al.* [19] studied the deposition of microcrystalline silicon at a low substrate temperature (25-100°C) by low-pressure, low-power, radio frequency plasma enhanced chemical vapour deposition (rf-PECVD) and by hot wire chemical vapour deposition (HWCVD). They observed that the deposition rate is independent of T_{sub}. In rf-PECVD, more

hydrogen dilution is needed for the amorphous to $\mu\text{-Si}$ transition at low T_{sub} . However, in HWCVD the dilution is independent of temperature for such a transition to occur, which has been attributed to the high atomic hydrogen flux provided by the HWCVD technique. The other difference is that the transition is abrupt for rf-PECVD deposited films (within an interval of 1–2% of dilution) whereas the transition is gradual (dilution between 80% and 90%) for the HWCVD case. The parameter range for the deposition of $\mu\text{-Si}$ is seriously reduced in the case of rf-PECVD, upon reducing the substrate temperature.

In the same group, Filonovich *et. al.*, presented a study of the structural, optoelectronic and transport properties of a series of silicon films deposited in a parameter region, namely hydrogen dilution, corresponding to a transition from amorphous to microcrystalline silicon by HWCVD and rf-PECVD on plastic substrates at 150 °C. For certain hydrogen dilution values, these deposition conditions can lead to the formation of Si nanocrystals in the silane plasma and to a growth of polymorphous silicon film. This material has improved carrier transport properties (ambipolar diffusion length = 220 nm) and has showed a very high photosensitivity ($> 5 \times 10^6$). A n-i-p solar cell fabricated using this polymorphous Si as intrinsic layer deposited on plastic, has shown an efficiency of 5.5% [20].

Alpuim *et. al.*, has also used this polymorphous material to fabricate thin-film silicon solar cells in the p-i-n superstrate diode configuration on plastic substrates at a temperature of 150°C, using different absorbing i-layers [21]. A typical solar cell structure in this work has the following successive layers: PEN/GZO/p/buffer/i/n/metal. PEN is a transparent polymer (polyethylene naphthalate), GZO is a transparent conductive window layer made of zinc oxide doped with gallium and buffer is a high-bandgap ~ 10 nm-thick amorphous silicon layer, which was placed at the p-i interface in order to prevent electron back diffusion into the p-layer and to protect the p-layer from atomic hydrogen attack during the i-layer deposition. This is crucial when depositing the i-layer by HW, since the high concentration of atomic hydrogen produced by decomposition of SiH_4 and H_2 at the filament readily attacks the boron-doped layer and will destroy it in the absence of the protective buffer layer. Flexible solar cells deposited entirely by RF-PECVD on PEN had a conversion efficiency of 5.0%. Similar solar cells on PEN but with the i-layer deposited by HWCVD had efficiency 4.5%. Based on spectral response measurements under different applied biases they showed that the main losses in conversion efficiency are in the long wavelength part of the spectrum.

The mechanism that has limited the efficiency of the devices was recombination in the i-layer, as was elucidated by measurements done under different illumination levels.

Y. Wang *et.al.*, looked at the stability of microcrystalline silicon solar cells with a HWCVD buffer layer inserted between the p/i interface. They studied long-term stability under storage in ambient atmosphere and performed light soaking experiments. All cells were stable or degraded slightly after storage for 2 years in air, and they observed that solar cells with HWCVD buffer layer degrade less than solar cells without buffer layer at similar crystalline volume fraction [22]. Upon light soaking all cells showed efficiency degradation to more or less extent depending on crystal volume fraction of the i-layer and the presence of the buffer layer: the solar cell with high crystal volume fraction are nearly stable, cells with high amorphous volume fraction degrade by up to 20%.

Wide optical bandgap and highly conductive p-type window layers have always been an attractive focus for a-Si:H solar cells [23-25]. To fabricate a p-type wide bandgap layer the alloying effect is usually invoked. For instance, by forming a hydrogenated amorphous silicon carbide (a-SiC_x:H) [26], the bandgap of the a-SiC_x:H layer could reach 1.8–3.3 eV, depending on the carbon content (x), and this kind of p-layer has been successfully used in the superstrate structure of glass/TCO/p-i-n/metal solar cells. But the incorporation of C atoms into the film also induces more disordered structural defects that limit further improvements of the performance of the solar cells and even lead to speeding up the light induced degradation of the devices. By looking at this problem, Zhihua Hu, *et. al.*, in cooperation with the FCT-UNLisbon group, reported a wide bandgap and highly conductive p-type hydrogenated microcrystalline silicon (μ c-Si:H) window layer prepared with a conventional rf-PECVD system under large H dilution condition, moderate power density, high pressure and low substrate temperature. By using this kind of p-layer, a-Si:H solar cells on bare stainless steel foil in n-i-p sequence have been successfully prepared with a V_{oc} of 0.90 V, a fill factor of 0.70 and an efficiency of 9.0%, respectively [27].

Another decisive characteristic in the suitability of any deposition process for device application is the deposition rate. For standard radio-frequency (13.56 MHz) rf-PECVD, a trend of high growth rates at high substrate temperatures can be obtained. However, very high frequencies (VHF), or ion-assisted depositions allow a high growth rate at lower substrate temperatures but they raise the issue of uniformity across large deposition areas [28].

Mai *et al.* [29], used the VHF-PECVD (94.7 MHz) technique under high working pressure to deposit a $\mu\text{c-Si:H}$ single-junction p-i-n (1 μm thick) solar cell at a deposition rate of 1.1 nm/s, with a high efficiency of 9.8%. The $1\times 1\text{ cm}^2$ thermally evaporated Ag back contacts defined the solar cell area. Solar cells were deposited on texture-etched ZnO-coated glass substrates at 200°C.

J. R. Rath *et al.* [30] from the former University of Utrecht group, now at Eindhoven, have reported a cell on polymer foil, deposited by VHF-PECVD at 50 MHz, with initial active area (0.912 cm^2) efficiency of 7.69% ($V_{\text{oc}} = 0.834\text{ V}$, $\text{FF} = 0.70$) and a minimodule of $8\times 7.5\text{ cm}^2$ with initial aperture area efficiencies of 6.7% ($V_{\text{oc}} = 6.32\text{ V}$, $\text{FF} = 0.65$) have been achieved. They made this cell using the Helianthos concept of manufacturing [31]. The fabricated cell consisted of an amorphous silicon single junction, in p-i-n configuration, with ZnO:Al/Al as back reflector.

T. Söderström, *et al.*, [32] reported the achievement of simultaneously high J_{sc} and V_{oc} on textured substrates and the optimization of n-i-p a-Si:H solar cell on flexible substrate. They found optimum substrate morphology for light trapping and developed a cell design that simultaneously maintains good V_{oc} and FF . The benefits of a high-bandgap amorphous carbide n-layer were implemented in the a-Si:H solar cell on PEN substrate with the demonstration of an initial 8.8% efficiency, for an intrinsic layer thickness of 270 nm.

In order to reduce losses in double junction cells, caused by the degradation of the top cell, it has been proposed to introduce an intermediate reflector, typically a TCO layer, and to further reduce the thickness of the top cell. Very thin amorphous silicon cells show extremely limited degradation, but their current is very low due to limited absorption. By introducing an intermediate reflector (IR), the current can be maintained at a high value, enabling high efficiencies with minimal degradation. The process complexity is increased, but promising efficiencies have been achieved with this concept [33,34]. By using this approach, F.J. Haug *et al.*, from the IMT group reported tandem devices, on low-temperature plastics with an efficiency of 10.9% (initial), by the introduction of IR layers made either from ZnO or from a Si-O based material that is deposited in-situ by PECVD. The i-layer thickness was only 270 nm for the a-Si:H cell [35].

A specific issue with tandem cells is the risk of increased spectral sensitivity and its impact on the module energy yield. Indeed, losses related to current mismatch can be exacerbated by natural changes in spectrum (related to different times of the day or

different seasons) because the relative absorption in the subcells may change. It has been found that, indeed, multijunction cells are more spectrally sensitive than classical modules [36]. If the module is well designed, however, it reaches its optimal energy yield for the most relevant spectra. High relative performance in kWh/kWp/year has been reported for double and even triple junction modules [37,38]. An a-Si:H/a-Si:H tandem solar cell on stainless steel foil as substrate, with initial efficiency of 8.5% has been reported by M.K. van Veen *et. al.* [39].

Efficiencies of triple-junction thin-film solar cells on small area devices reach impressive values of around 15% initial and around 13% stabilized [40]. This triple-junction stack is deposited onto a thin, flexible stainless steel substrate coated with Ag/ZnO back reflector. Transparent-conductive indium-tin oxide (ITO) is deposited on top of the top cell, serving as the top contact as well as an antireflection coating. However, research and development is now focusing on upscaling the processes to large areas, producing minimodules and modules, and solving issues for industrial application, notably large-area TCO deposition and its texturization.

Reported efficiencies of thin film silicon solar cells on flexible substrates from several research groups are included in table 1.1 for reference.

Table 1.1 Reported efficiencies at AM1.5 light condition of thin film silicon solar cells on plastic substrates (from [65]).

Cell type	Substrate	Source	Eff. (%)
n-i-p (a-Si/a-SiGe/nc-Si) D	SS	United Solar Ovonic, USA	15.4
n-i-p (a-Si/a-SiGe) D	Kapton	Fuji Electric, Japan	10.1
n-i-p (a-Si) D	PEN	IMT, Switzerland	8.7
n-i-p (a-Si) D	E/DT	AIST, Japan	6
n-i-p (nc-Si) D	LCP	AIST, Japan	8.1
n-i-p (a-Si/a-Si) D	PET	Univ. Stuttgart, Germany	4.9
n-i-p (a-Si) D	PET	Univ. Utrecht, Netherlands	5.9
n-p (mono-Si) T	Plastics	Univ. Stuttgart, Germany	14.6
p-i-n (a-Si) T	Polyester	Univ. Utrecht/Nuon, Netherlands	7.7
p-i-n (a-Si/nc-Si) T	Polyester	Univ. Utrecht/Nuon, Netherlands	8.1
n-i-p (a-Si/a-SiGe/a-SiGe) DT	Polymer	United Solar Ovonic, USA	9.7%*

SS: stainless steel; E/DT: tetracyclododecene co-polymer; LCP: liquid crystal polymer; PEN: polyethylene naphthalate; PET: polyethylene terephthalate; Kapton: polyimide; *AM0 light condition; D: direct deposition; T: transfer method; DT: direct deposition + transfer.

1.2 Piezoresistive sensors

First discovered by Lord Kelvin in 1856, the piezoresistive effect is a widely used sensor principle. Simply put, an electrical resistor may change its resistance when it experiences a strain and deformation. This effect provides an easy and direct energy/signal transduction mechanism between the mechanical and the electrical domains. Today, it is used in the MEMS field for a wide variety of sensing applications,

including accelerometers, pressure sensors [41], gyro rotation rate sensors [42], tactile sensors [43], flow sensors, sensors for monitoring structural integrity of mechanical elements [44], and chemical/biological sensors.

The piezoresistive property of crystalline silicon (c-Si) was first reported by C. Smith [45]. Since then, many Si-based sensors use that property as their operation principle [46-49]. In particular, doped silicon exhibits remarkable piezoresistive response characteristics among all known piezoresistive materials [45]. By strict definition, piezoresistors refer to resistors whose resistivity changes with applied strain. Metal resistors change their resistance in response to strain mainly due to the shape deformation mechanism. Such resistors are technically called strain gauges. The resistivity of semiconductor silicon changes as a function of strain. Silicon is therefore a true piezoresistor.

Piezoresistive sensors measure strain from the relative resistance change of a Si transducer that is deformed to the strain to be measured. Piezoresistance in c-Si is highly anisotropic and is described by a set of coefficients that are the elements of the piezoresistive tensor, relating the change in electrical resistivity in a particular crystallographic direction to the components of the applied stress tensor.

Polycrystalline metallic strain-gauge sensors are also common but they are much less sensitive than their semiconductor counterparts [49]. This is because their operation is mainly based on resistance variation due to stress-induced dimensional changes and not on changes on the resistivity itself, as it is the case with Si (or Ge) sensors. In a semiconductor, volume changes due to strain affect both carrier concentration and carrier mobility, leading to resistance changes. But more important, in strained Si, potentials modify the band structure near the edge of the conduction and valence bands, leading to changes in carrier effective mass and/or occupancy of the density of states at energies close to the Fermi level. This mechanisms dramatically enhance the piezoresistive effect in semiconductors when compared to metals [45,49]. As the Fermi level position approaches the conduction or valence band edges the effect is expected to be enhanced and therefore piezoresistance is more important in doped than in intrinsic Si. However, both the physical origin and the corresponding values of the piezoresistive coefficients are very different in p- and n-type material [45-48].

The piezoresistive effect has also been found in thin polycrystalline silicon films [45, 50]. Due to the semi-crystalline nature of these films the reported effect is rather isotropic and it broadly averages the resistance changes of the randomly oriented

crystallites, thus retaining the signal of the largest c-Si piezoresistive coefficient. Moreover, grain boundaries also play a role in piezoresistance of microcrystalline films and their net effect is to attenuate resistivity changes occurring in the crystalline grains [53]. Physical models considering the role of intra-grain and intergrain mechanisms in the piezoresistive properties of 3C-SiC have been recently proposed [54].

The combination of standard large scale, low cost, semiconductor micro-fabrication methods with miniaturization of high sensitivity Si-based sensors on plastic substrates opens a richness of application possibilities [50].

Electromechanical and interferometric methods have the highest sensitivity to detect applied stress, of the order of 0.05 Pa [55]. The former may replace the latter in process control industries; it has been demonstrated that micron-sized polysilicon piezoresistive sensors, integrated at low cost in small chips, can simultaneously measure temperature, differential and absolute pressure [56]. Differential deformations of less than 100 nm and pressures of less than a few tenths of Pa have been detected in this way.

Another demonstration at the University of Peking, consisted in using polysilicon piezoresistive sensors, micro-fabricated into cantilever-arrays, to detect a few ppm of concentration of ammonia (NH₃) [57]. These chemical sensors have potential to low cost, water contamination control.

Another development consisted in using as position sensors, poly-crystalline diamond thin films, with a piezoresistive gauge factor of 28, for implantable cochlear probes [58].

The application of miniaturized Si-like piezoresistive sensors in biomedical instruments to measure pressure with values of the order of 10⁵ dyne/cm² (blood pressure in artery and intraocular eye), is becoming increasingly important. Because they operate at low frequency bandwidth, signal to 1/f noise should be maximized [59].

Recently, P. Alpuim *et al.* reported the piezoresistive response, under low-frequency oscillations, of n-type $\mu\text{c-Si:H}$ thin film microresistors fabricated by HWCVD at 150 °C on plastic substrates using standard lithographic techniques [60].

1.3 Plastic substrates

The substrate is a passive component in the device and is required to be mechanically stable, matching thermal expansion coefficient with deposited layers and to be inert during the device fabrication. Suitable substrates are selected for different

processes on the basis of these criteria. However, for mass production, the price is a leading factor when choosing the production technology. It turns out that whatever the production/deposition technology, and whatever the thin film solar cell material is, the total cost per watt is primarily determined by the cost of the substrate, and one of the most expensive materials used in the particular technology [61]. Choosing an inexpensive substrate will lead to cost effective production and lower cost per watt ratio.

Semiconductors have been deposited on plastic substrates since the 90s, but still offer a wide range of advantages in financial aspect over other conventional substrates for solar cells. Plastic is a flexible material and this makes it easy to produce solar cells of different shapes and for different applications. It is well-suited for monolithic series connections of cells to a module [62].

An important disadvantage is that it requires low processing temperature. Moreover, the surface softness of plastics can create problems of mismatch with the film, as can the thermal expansion coefficient if it differs from the coefficient of the deposited film [63]. However, previous experience of deposition on selected plastic substrates shows that silicon films have normally a very good adhesion to the substrate and that residual stresses are limited by plastic deformation of the substrate surface thus avoiding film delamination [50,60].

PET (polyethylene terephthalate) is a common inexpensive transparent plastic with a wide range of applications and a potential solar cell substrate (can be used in superstrate configuration although long term stability to UV-radiation is an issue. The same is true for PEN).

PEN (polyethylene naphthalate) is a similar polyester, that has a higher upper working temperature. PEN starts to shrink at 190 °C and is certified for electrical use up to 155 °C (upper working temperature). The thermal expansion coefficient is $20\text{-}21 \times 10^{-6} \text{ K}^{-1}$. Its primary use is for electronic devices.

PI (polyimide) is mainly used for capacitors, insulation, circuit boards, in aerospace and vacuum technology. It has an upper working temperature of 250-320 °C and a thermal expansion $30\text{-}40 \times 10^{-6} \text{ K}^{-1}$. It is significantly more expensive than PET and PEN but allows the use of high substrate temperatures [64].

1.4 Organization of the thesis

The work in this thesis can be divided in three parts: (1) the development of high-rate deposited intrinsic and doped layers on plastics (2) the development of flexible thin film silicon solar cells on transparent and opaque plastic substrates and (3) the fabrication of strain gauge sensors based on the piezo-resistive properties of the doped layers deposited on plastics.

The thesis is organized in seven chapters. An introduction to the topic in which this thesis is inserted and a discussion of the state-of-the-art are done in the first chapter. The last chapter summarizes the conclusions obtained in this work.

Chapter 2 describes the deposition and characterization techniques used during this work. We used Plasma Enhanced Chemical Vapor Deposition (rf and VHF) and Hot Wire CVD for the deposition of silicon thin films. In this part are also discussed the main mechanisms of films growth and the role of hydrogen in these processes. The description of the characterization techniques covers the structural and optoelectronic techniques used for the thin films analysis and the techniques used for solar cell characterization. The results and discussions concerning the studies realized in this thesis are organized in the remaining chapters as follows:

High-rate deposited intrinsic and doped layers on plastics

Chapter 3 presents and discusses the results about the structural and optoelectronic properties of a-Si:H and $\mu\text{-Si:H}$ intrinsic and doped layers deposited by rf-PECVD on plastic (PEN) at 150 °C. The study is focused in the optimization of the layers by studying the influence of deposition pressure and power coupled to the plasma on the deposition rate and film electronic quality.

Flexible thin film silicon solar cells

Chapter 4 deals with the development of amorphous silicon solar cells at a substrate temperature of 150 °C on PEN/TCO, in the superstrate p-i-n configuration, and on PI foils at a substrate temperature of 200 °C, in the substrate n-i-p configuration. The results about room temperature deposited doped ZnO films on plastic substrates are also shown in this chapter. Their optical, electronic and structural properties were correlated and optimized. Also, light trapping effects were explored by laser texturing plastic substrates. Their haze, total transmittance and reflectance were compared with those of untextured substrates.

Chapter 5 shows the development of microcrystalline thin film silicon solar cells at a substrate temperature of 200 °C, in the substrate n-i-p configuration on PI foils. It also shows the achievement of textured back reflectors for the solar cells on PI, by wet etching of a TCO layer followed by a highly reflective Ag/ZnO double layer coating. Solar cells on flat and textured glass and PI are compared and the results discussed. These results were obtained at Forschungszentrum Jülich (IEK-5).

Flexible strain gauge sensors

Chapter 6 describes the manufacture and characterization of a thin *skin-like* piezoresistor strain-sensing membrane and the miniaturization of piezoresistive sensor arrays based on n-type hydrogenated microcrystalline silicon thin films ($\mu\text{-Si:H}$) deposited on flexible polyimide substrates (PI). The $\mu\text{-Si:H}$ thin films were prepared by hot-wire chemical vapor deposition, and had a piezoresistive gauge factor of -32.2.

The main results showed in the chapters of this thesis were presented to the scientific community in international conferences and published in international scientific journals widely disseminated in their research area. The publications related to this thesis were:

Chapter 3:

- **E. Marins**, V. Guduru, M. Ribeiro, F. Cerqueira, A. Bouattour and P. Alpuim. High-rate deposition of nano-crystalline silicon thin films on plastics. *Phys. Status Solidi C* V. 8, No. 3, p. 846–849, 2011.

Chapter 4:

- P. Alpuim, A. Samantilleke, **E. Marins**, F. Oliveira, M.F. Cerqueira, L. Rebouta, S. Stefanov, S. Chiussi, C. Serra, J.E. Bourée. Amorphous silicon thin-film solar cells deposited on flexible substrates using different zinc oxide layers. *Phys. Status Solidi C* V. 7, No. 3–4, p. 1061–1064, 2010.

Chapter 5:

- **E. Marins**, M. Warzecha, S. Michard, J. Hotovy, W. Boettler, P. Alpuim and F. Finger. Flexible n-i-p thin film silicon solar cells on polyimide foils with textured ZnO:Ga back reflector. *Thin Solid Films*, V. 571, p. 9-12, 2014.

Chapter 6:

- P. Alpuim, **E. Marins**, P.F. Rocha, I.G. Trindade, M.A. Carvalho, S. Lanceros-Mendez. Ultra-Sensitive Shape Sensor Test Structures Based on Piezo-Resistive Doped Nanocrystalline Silicon. *Vacuum*, V. 83, p. 1279–1282, 2009.
- P. Alpuim, V. Correia, **E. Marins**, J.G. Rocha, I.G. Trindade and S. Lanceros-Mendez. Piezoresistive silicon thin film sensor array for biomedical applications. *Thin Solid Films*, V. 519, p. 4574–4577, 2011.

References

- [1] A. Shah, ed., Thin-film Silicon Solar Cells, First edition, EPFL Press, 2010.
- [2] Photon International, March 2009, p. 170.
- [3] M.A. Green, Physica E: Low-dimensional Systems and Nanostructures, **14** (2002) p. 65.
- [4] A. Müller, B. Ghosh, R. Sonnenschein, P. Woditsch, Materials Science and Engineering: B, **134** (2006) p. 257.
- [5] V. Fthenakis, S. Gualtero, R. van der Meulen, H.C. Kim, Materials Research Society Symposium Proceedings, **1041** (2008) p. 25.
- [6] V. Fthenakis, H.C. Kim, E. Alsema, Environmental Science and Technology, **42** (2008) p. 2168.
- [7] C. Wadia, A.P. Alivisatos, D.M. Kammen, Environmental Science and Technology, **43** (2009) p. 2072.
- [8] D.E. Carlson and C.R. Wronski, Appl. Phys. Lett., **28** (1976) p. 671.
- [9] J. Meier, R. Flückiger, H. Keppner, A. Shah, Appl. Phys. Lett., **65** (1994) p. 860.
- [10] J. Meier, P. Torres, R. Platz, S. Dubail, U. Kroll, J.A.A. Selvan, N.P. Vaucher, Ch. Hof, D. Fischer, H. Keppner, A. Shah, K.-D. Ufert, P. Giannoules, J. Koehler, Mater. Res. Soc. Symp. Proc., **420** (1996) p. 3.
- [11] T. Baba, et al., In Proceedings of the 13th European Photovoltaic Solar Energy Conference, Nice, France (1995) p.1708.
- [12] A. Shah, H. Schade, M. Vanecek, J. Meier, E. Vallat-Sauvain, N.Wyrsh, U. Kroll, C. Droz and J. Bailat, In Proceedings of the Technical Digest of the 14th International Photovoltaic Science and Engineering Conference, Bangkok, Thailand (2004) p. 39.
- [13] R.A. Street, J. Zesch, M.J. Thompson, Appl. Phys. Lett., **43** (1983) p. 672.
- [14] Guy Beaucarne, Advances in OptoElectronics, (2007), Article ID 36970.
- [15] D.L. Staebler, C.R. Wronski, Appl. Phys. Lett., **31** (1977) p. 292.
- [16] J. Meier, S. Dubail, R. Flückiger, D. Fischer, H. Keppner, and A. Shah, In Proceedings of the 1st IEEE World Conference on Photovoltaic Energy Conversion, Hawaii, USA, **1** (1994), p. 409.
- [17] H. Liu, S. Jung, Y. Fujimura, Y. Toyoshima, H. Shirai, Jpn. J. Appl. Phys. **40** (2001) p. L215.
- [18] G. Cicala, P. Capezzuto, G. Bruno, J. Vac. Sci. Technol. A, **19** (2001) p. 515.
- [19] P. Alpuim, V. Chu, J.P. Conde, J. Appl. Phys. **86** (1999) p. 3812.
- [20] S.A. Filonovich, P. Alpuim, L. Rebouta, J.-E. Bourée, Y. M. Soro, Journal of Non-Crystalline Solids, **354** (2008) p. 2376.

- [21] P. Alpuim, G.M. Junior, S.A. Filonovich, P. Roca i Cabarrocas, J.-E. Bouree, E.V. Johnson, Y.M. Soro, 23rd European Photovoltaic Solar Energy Conference and Exhibition (23rd EU PVSEC), Valencia, Spain (2008) p. 2455.
- [22] Y. Wang, X. Geng, H. Stiebig and F. Finger, *Thin Solid Films*, **516** (2008) p. 733.
- [23] H. Sannomiya, K. Nomoto, A. Chida, Y. Nakata, Y. Yamamoto, 1st IEEE World Conference on Photovoltaic Energy Conversion, Hawaii, USA (1994) p. 405.
- [24] M. Topic, F. Smole, J. Furlan, In *Proceeding of 25th PVSC*, Washington DC, USA (1996) p. 1109.
- [25] X. Deng, S.J. Jones, T. Liu, M. Izu, S.R. Ovshinsky, In *Proceeding of 26th PVSC*, Anaheim, CA, USA (1997) p. 591.
- [26] Y. Hattori, D. Kruangam, K. Katoh, Y. Nitta, H. Okomoto, Y. Hamakawa, In *Tech. Dig. Int. PVSEC-3*, Tokyo, Japan (1987) p. 171.
- [27] Z. Hu, Xianbo Liao, Hongwei Diao, Yi Cai, Shibin Zhang, Elvira Fortunato, Rodrigo Martins, *Journal of Non-Crystalline Solids*, **352** (2006) p. 1900.
- [28] J.K. Rath, *Solar Energy Materials & Solar Cells*, **76** (2003) p. 431.
- [29] Y. Mai, S. Klein, R. Carius, J. Wolff, A. Lambertz, and F. Finger, *J. Appl. Phys.* **97** (2005) p. 114913.
- [30] J.K. Rath, Y. Liu, A. Borreman, E.A.G. Hamers, R. Schlatmann, G.J. Jongerden, R.E.I. Schropp, *Journal of Non-Crystalline Solids*, **354** (2008) p. 2381.
- [31] E. Middelmann, et. al., In *Proceedings of the 2nd World Conference and Exhibition on Photovoltaic Solar Energy Conversion (WCPEC-2)*, Vienna, Austria (1998) p. 816.
- [32] T. Söderström, F.-J. Haug, V. Terrazzoni-Daudrix, and C. Ballif, *J. Appl. Phys.* **103** (2008) p. 114509.
- [33] C. Ballif, J. Bailat, D. Dominé, et al., In *Proceedings of the 21st European Photovoltaic Solar Energy Conference*, Dresden, Germany (2006) p. 1552.
- [34] K. Yamamoto, A. Nakajima, M. Yoshimi, et al., In *Technical Digest of the 15th International Photovoltaic Science and Engineering Conference (PVSEC '05)*, Shanghai, China, **1** (2005) p. 529.
- [35] F.-J. Haug, T. Söderström, M. Python, V. Terrazzoni-Daudrix, X. Niquille, C. Ballif, *Solar Energy Materials and Solar Cells*, **93** (2009) p. 884.
- [36] T. Minemoto, M. Toda, S. Nagae, et al., *Solar Energy Materials and Solar Cells*, **91**, no. 2-3 (2007) p. 120.
- [37] A. V. Shah, H. Schade, M. Vanecek, *Progress in Photovoltaics: Research and Applications*, **12**, no. 2-3, (2004) p. 113.
- [38] M. van Cleef, P. Lippens, and P. Call, In *Proceedings of the 17th European Photovoltaic Solar Energy Conference*, Munich, Germany (2001).
- [39] M.K. van Veen, R.E. Schropp, *Thin Solid Films*, **403–404** (2002) p. 135.

- [40] J. Yang, Baojie Yan, Subhendu Guha, *Thin Solid Films*, **487** (2005) p. 162.
- [41] S. Sugiyama, M. Takigawa, and I. Igarashi, *Sensors and Actuators A*, **4** (1983) p. 113.
- [42] F. Gretillat, M.-A. Gretillat, and N.F. de Rooij, *Journal of Microelectromechanical Systems*, **8** (1999) p. 243.
- [43] B.J. Kane, M.R. Cutkosky and T.A. Kovacs, *Journal of Microelectromechanical Systems*, **9** (2000) p. 425.
- [44] C. Hautamaki, et al., *Journal of Microelectromechanical Systems*, **8** (1999) p. 272.
- [45] C.S. Smith, *Physics Review*, **94** (1954) p. 42.
- [46] W.G. Pfann and R. N. Thurston, *J. Appl. Phys.* **32** (1961) p. 2008.
- [47] O.N. Tufte, P.W. Chapman and D. Long, *J. Appl. Phys.* **33** (1962) p. 3322.
- [48] I. Goroff, L. Kleinman, *Phys. Rev.* **132** (1961) p. 1080.
- [49] M. Elwenspoek, R. Wiegerink, *Mechanical Microsensors*, Springer, New York (2001) p.87.
- [50] P. Alpuim, V. Chu, J.P. Conde, *IEEE Sensors J.* **2** (2002) p. 336.
- [51] S. Nishida, M. Konagai, K. Takahashi, *Jpn. J. Appl. Phys.* **25** (1986) p. 17.
- [52] P. Alpuim, S. Lanceros-Mendez, V. Sencadas, M. Andrade, S.A. Filonovich, communication to the E-MRS Spring Meeting (E-MRS - IUMRS - ICEM 06), May 29 - June 2, Nice, France (2006).
- [53] L. Fang, W. L. Wang, P. D. Ding, K. J. Liao and J. Wang, *J. Appl. Phys.* **86** (1999) p. 5185.
- [54] M. Eickhoff, M. Stutzmann, *J. Appl. Phys.* **96** (2004) p. 2878.
- [55] Milton Ohring, "The materials Science of Thin Films", Chapter 9.4, Academic Press Inc. (1992) p. 421.
- [56] R. Pryputniewicz et al., In *Proceedings of Internat. Symp. On Microscale Systems*, Orlando FL, USA (2000) p. 76.
- [57] Yu Xiao-Mei et al., *Chin. Phys. Lett.*, **20** (2003) p. 1637.
- [58] Y. Tang, M. Aslam, J. Wang and K. Wise, "Fabrication and test of Poly-Crystalline Diamond Piezoresistive Sensors for Cochlear Implant Probe", report ECE department, Michigan State University.
- [59] B. Bae, B. Flachsbarth, K. Park and M. Shannon, *J. Micromech. Microeng.* **14** (2004) p. 1597.
- [60] P. Alpuim, V. Correia, E. Marins, J.G. Rocha, I.G. Trindade and S. Lanceros-Mendez, *Thin Solid Films*, **519** (2011) p. 4574.
- [61] K. L. Chopra, P. D. Paulson, and V. Dutta, *Thin-Film Solar Cells: An Overview*, *Progress in Photovoltaics: Research and Applications*, **12** (2004) p. 69.
- [62] M. Kimming, Master's thesis, Lund University (2005).

-
- [63] F. Sarto, M. Alvisi, E. Melissano, A. Rizzo, S. Scaglione, and L. Vasanelli, *Thin Solid Films*, **346(1)** (1999) p. 196.
- [64] Q. Wang, E. Iwaniczko, J. Yang, K. Lord, S. Guha, K. Wang, and D. Han, In *Proceedings of 29th IEEE PV Specialists Conference*, New Orleans, Louisiana, USA (2002) p. 1222.
- [65] J.K. Rath, M. Brinza, Y. Liu, A. Borreman and R.E.I.Schropp, *Solar Energy Materials & Solar Cells*, **94** (2010) p. 1534.

Chapter 2

2 Experimental Techniques

The techniques that have been used for the deposition and characterization of the a-Si:H and $\mu\text{c-Si:H}$ layers and solar cells, are described in this chapter.

2.1 Plasma Enhanced Chemical Vapor Deposition

In general, thin films may be fabricated either by physical vapor deposition (e.g., evaporation or sputtering) of the bulk material, or by chemical vapor deposition from the decomposition of suitable gases that contain the desired film material.

Historically both evaporation and sputtering of elemental silicon were used to obtain thin films of amorphous silicon. However, these films contained high defect concentration, mostly caused by poorly coordinated Si atoms, i.e. by so-called "dangling-bonds". Due to these high defect concentrations, the gap states density between the valence and conduction bands far exceeds the dopant densities that can be typically achieved. Therefore, this material is not suitable for use in an electronic semiconductor device, which inherently requires the presence of *n*- and/or *p*-type regions.

The high density of defect states can be somewhat reduced through post-hydrogenation by heating the films in a hydrogen atmosphere, or, in the case of sputtering, by adding hydrogen to the sputtering gas. However, these methods of preparation have not proved successful in the further development of suitable materials for electronic applications. Since it was recognized that silicon films deposited at low temperatures require the presence of hydrogen to "saturate" or "passivate" the dangling bonds, Chemical Vapor Deposition (CVD) methods have been

chosen with a source containing both silicon and hydrogen, which is then decomposed by supplying thermal or electrical energy to generally form hydrogenated amorphous silicon (a-Si:H) films. Thus, in 1969, the decomposition of silane (SiH_4) in a glow discharge yielded hydrogenated amorphous silicon films with good photoconductivity [1], indicating a defect concentration well below the generated photocarrier concentration. Adding a dopant gas to the silane, glow discharge deposition has opened the way for the effective doping of a-Si:H thin films [2], and hence for the possibility of creating electronic thin-film devices.

Since then the development of Si-based thin films for PV applications has largely remained based on the decomposition of silane as the Si precursor source material. Other gases have also been used, like the chlorinated silane source gases such as SiH_2Cl_2 , SiHCl_3 , and SiCl_4 , in order to reduced the growth temperature. Several forms of energy supply for the decomposition of the reactant gases have been developed, namely:

- electrical energy, supplied in a glow discharge (plasma) for plasma-enhanced chemical vapor deposition (PECVD):
- thermal energy by heating a filament, for thermo-catalytic chemical vapor deposition (Cat-CVD), more commonly called Hot-Wire CVD (HWCVD).
- Photo-CVD or Laser-CVD (radiant energy)

PECVD is conducted in a plasma reactor that, in the parallel plate capacitive geometry, usually consists of

- a vacuum chamber, equipped with an inlet for the reaction gases, and pumps to remove unreacted and reacted gases;
- a pair of parallel electrodes, one grounded and acting as the support for the substrate to be coated, and the other connected to an electrical power supply, and possibly also acting as a shower head to uniformly distribute the reaction gases;
- a gas handling system;
- substrate heating.

This arrangement, schematically shown in Figure 2.1, facilitates the sequential deposition of the entire semiconductor structure, either in a single-junction or a multi-junction (tandem or triple cell) configuration, as *pin* or *pin/pin* etc. To this end, not only silane is used (as is basically sufficient for the intrinsic *i*-layer), but also doping gases containing boron and phosphorus, such as diborane (B_2H_6) or trimethylboron [$\text{B}(\text{CH}_3)_3$], and phosphine (PH_3), for depositing *p*- and *n*-layers, respectively. Additionally, the

energy gaps of the semiconductor film may be varied by adding gases containing other group-IV elements, specifically

- methane (CH_4) in order to alloy with carbon and, thus, to increase the energy gap of the p -layer to create a window layer;
- germane (GeH_4) in order to alloy with germanium and, thus, to decrease the energy gap of the i -layer for enhanced red-response, particularly for multi-junction cell structures.

PECVD is an extremely complex process involving a multitude of interactions between the plasma, chemical reactions of the gases and their reaction products, as well as interactions with the surrounding surfaces, ultimately including the substrate to be coated.

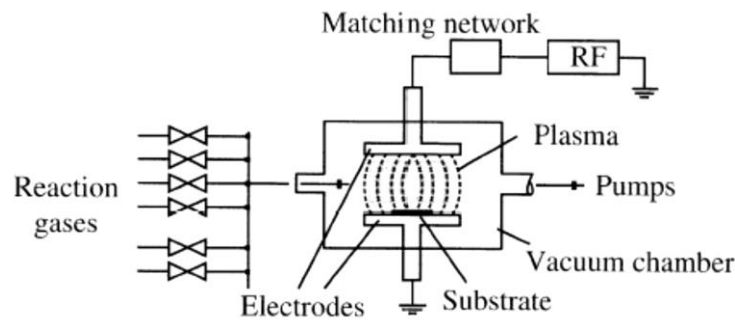


Fig. 2.1: Schematic of PECVD reactor (from [3])

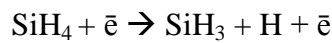
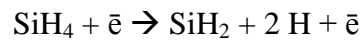
The application of a sufficiently high RF voltage (typically at the industrial frequency of 13.56 MHz) to a capacitive configuration of parallel electrodes in a container filled with gas at low pressure leads to the generation of a low-pressure plasma, also designated as “cold plasma” or “glow discharge (GD)”. The plasma reactions occur while the gas and the parts exposed to the plasma remain at relatively low temperatures. The plasma is ignited by the generation of electrons and ions, due to the ionization of gas molecules (initiated by ever-present cosmic rays), followed by subsequent secondary electron emission from the electrodes, and further ionizations with charge carrier multiplication. The ignition of the plasma may sometimes require high voltage pulses supplied from a Tesla coil via a high-voltage feedthrough.

The plasma contains electrons, positive and negative ions, as well as neutral atoms, molecules, free radicals, and metastable species. Basically, the described formation of electrons and ions leads to various interactions with the gases, and gives rise to chemical reactions and the formation of radicals and other reactive molecular fragments.

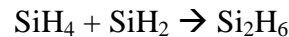
Both concentration gradients and electrical fields support a mass transport by diffusion and drift, respectively. Thereby interactions of various species including chemical reactions with the substrate surface are initiated, and specific temperature-dependent sticking coefficients and reaction activation energies determine the composition and structure of the film that is deposited.

Based on the use of the source gases silane (SiH_4 , also called, more specifically, “monosilane”) and hydrogen (H_2), the main chemical reactions may be grouped into three categories [3]:

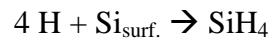
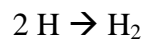
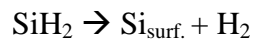
- electron impact dissociation, with the reactions



- reactions with radicals



- surface reactions that occur on the substrate, as well as on plasma-exposed surfaces in the reactor; these reactions refer to the deposition of silicon radicals, to etching by atomic hydrogen, and to hydrogen recombination at the surface:



$\text{Si}_{\text{surf.}}$ refers to an a-Si:H or a $\mu\text{c-Si:H}$ layer surface. One should note that the amount of hydrogen needed to saturate dangling bonds is typically less than 1% of the total hydrogen content in the film. The amount of hydrogen being incorporated into the deposited silicon film is typically in the range 10-15 atom% or more, if deposition occurs at low substrate temperature. However, the actual hydrogen content in the deposited film ($\text{Si}_{\text{surf.}}$) is not apparent in the chemical reactions given above. For the surface reactions, the availability of SiH_2 and atomic hydrogen mainly determines the balance between film growth and etching. This balance governs the degree of

crystallinity from amorphous to microcrystalline silicon.

These reactions, in addition to those between higher silanes Si_nH_m not shown here, take place with different rate constants that are pressure- and temperature-dependent.

Other PECVD processes use Very High Frequency (VHF) plasma excitation in the range of 30-300 MHz and will be discussed later in section 2.1.2.

PECVD can also be done using remote plasma, often inductively coupled to the electrodes which are designed like antennas or coils. In remote plasmas the reactor region where the plasma is generated is different from the region where the substrate is placed. This allows to inject different reactant gases in different regions of the reactor, namely in the plasma cavity and in the deposition chamber region. Both regions are in vacuum and are connected by an aperture. The advantage of such geometries is to avoid contact between the film growing surface and the plasma thus avoiding surface damage by ion bombardment.

2.1.1 Electrical plasma properties

The voltage required for plasma ignition depends on the gas pressure p and on the electrode spacing d ; it is determined by the Paschen curve; a curve which features a minimum for the ignition voltage at a specific value of $p \times d$ [3].

An electric potential distribution between the electrodes is established; it depends on the applied RF voltage U_{RF} , and on the areas of the electrodes (including grounded shields or reactor parts exposed to the plasma). The potential distribution is given by the energy distributions of the electrons and ions that are exposed to the electric fields between the electrodes. These electric fields are set up in the vicinity of the electrodes. The basic mechanism is as follows: electrons have much higher thermal velocities than ions, and can, thus, reach the electrodes faster, leaving the ions behind. To preserve overall charge neutrality and to render net currents zero, electric fields develop near the electrodes, retarding electrons and accelerating ions. These fields in front of the electrodes extend over relatively small distances (typically in the order of a fraction of a millimeter), which are determined by the resulting space charge densities. These regions in front of the electrodes are positively charged, are composed mostly of ions, and represent the so-called “sheaths”, as illustrated in figure 2.2. The sheaths are responsible for ion bombardment. At higher plasma excitation frequencies the sheaths become

thinner; this also means lower energies for the ion bombardment.

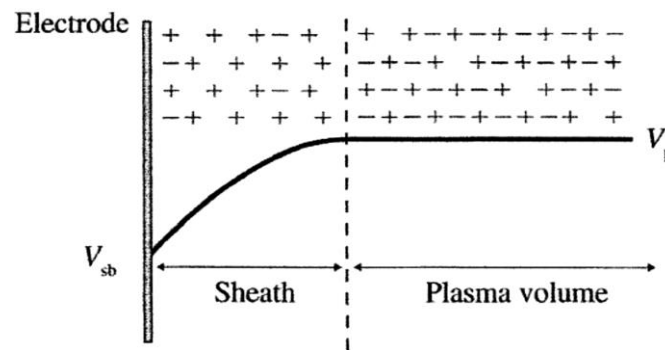


Fig. 2.2: Positive space charge region (so-called sheath), and field-free plasma volume (also called plasma bulk) (From [3]).

As a result of the generated fields, the following time-averaged potentials are assumed (see fig. 2.3):

- the so-called self-bias V_{sb} for the RF-powered electrode;
- zero potential for the grounded electrode; it is to the grounded electrode that one normally fixes the substrate to be deposited. The substrate surface is separated from the grounded electrode surface by the substrate thickness (i.e. usually by the glass thickness), and takes on (in case of an electrically isolating substrate) a certain relatively small potential, which is not specifically shown in figure 2.3;
- the plasma potential V_p ; since, due to their thermal velocities, more electrons than positive ions leave the plasma, the bulk of the plasma between the sheaths assumes a positive plasma potential V_p ;
- the potential differences across the sheaths (sheath voltages); these are U_c in front of the RF-powered electrode, and U_A in front of the grounded electrode, respectively.

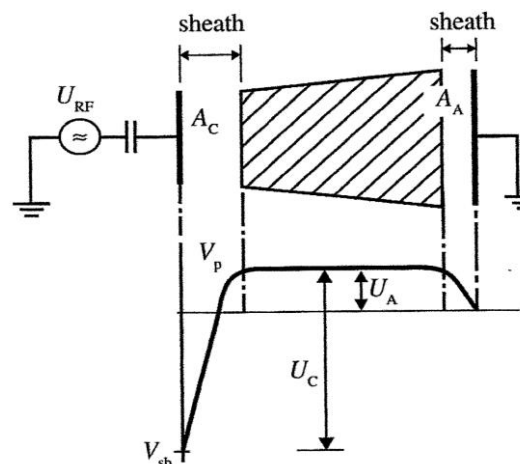


Fig. 2.3: Potentials and sheath voltages in a plasma reactor (from [3]).

2.1.2 VHF plasma excitation

The frequency of 13.56 MHz (generally called “rf”, radio frequency) corresponds to the standard frequency reserved by the International Electrotechnical Commission (IEC) for Industrial High-Frequency Applications. It is therefore also the frequency that has traditionally been most widely used. However, benefits in applying higher frequencies extending into the range of 30-300 MHz (generally called “VHF”, very high frequency) have been recognized for quite some time [4]. As a result, the use of higher excitation frequencies has led to higher deposition rates, without sacrificing film quality. The ion energies become lower with higher plasma frequencies, while at the same time higher deposition rates are achieved.

All attempts to raise the deposition rate by increasing the plasma power are generally limited by the onset of powder formation within the gas phase. At higher frequencies the electric fields of the plasma discharge are smaller, and also the composition of the radicals may be less conducive to gas-phase polymerization. In effect higher deposition rates at VHF are clearly compatible with powder-free plasmas. However, to obtain uniform deposition across large areas the VHF technology faces problems, and several approaches aimed at combining the higher deposition rates, due to higher plasma excitation frequencies, with acceptable deposition uniformities over large areas have been attempted.

Depending on the ion energy, ion bombardment affects the quality of the growing film in two ways:

- For ion energies larger than the threshold energy for defect generation (approximately 15 eV), which typically applies to reactor operation at the standard RF, ion bombardment creates damage by breaking bonds, and by forming weak bonds and microvoids.
- At higher frequencies, ion energies remain lower, i.e. below the threshold energy for defect generation. These lower ion energies give rise to an increased surface mobility of the deposited species on the growing film, and thus provide for rearrangements of deposited species and more orderly film growth.

2.2 Hot-Wire Chemical Vapor Deposition

As an alternative to PECVD, Hot-Wire Chemical Vapor Deposition (HWCVD), also known as catalytic CVD (Cat-CVD) has emerged since the eighties as a new method to deposit thin-film silicon and related materials. The technique has attracted attention from academia and industry due to the higher film deposition rates attainable and to the fact that it relies on an inherently ion bombardment-free process for film growth.

2.2.1 Description of the HWCVD technique

In the HWCVD technique, the source gases (SiH_4 , C_2H_2 , H_2 , ...) are introduced into a vacuum chamber, and a metallic filament (more often tungsten, but any refractory metal will do, e.g. Ta, Mo) is heated up to a high temperature (1700 °C to 2500 °C) providing thereby the surface for heterogeneous thermal decomposition of the gases into radical species. The filament acts as catalyst, and therefore the process is also called “catalytic chemical vapor deposition (Cat-CVD)” [5]. The radicals thus generated diffuse in the vacuum until they reach the substrate where they induce film growth on the temperature-controlled substrate, which is facing the filament. A schematic view of a hot-wire deposition chamber is shown in figure 2.4.

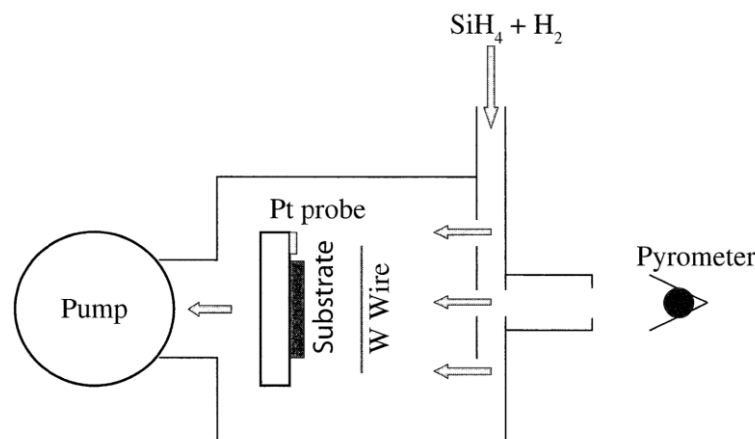


Fig. 2.4: Schematic arrangement of a HWCVD reactor (from [3]).

The wire temperature is determined by using a single-wavelength, disappearing-filament optical pyrometer (by levelling the brightness of the incandescent object with that of the inner lamp), with corrections made for effective emissivity. Different

spectroscopic techniques, such as threshold ionization mass spectrometry, single-photon ionization or laser-induced fluorescence, can be attached to the reactor for probing the radicals produced by hot-wire decomposition. The most important advantages of the HWCVD process, as compared to the PECVD process are:

- Since the technique is thermal and catalytic in nature, and relies on a heated metal filament to decompose the gas species, there are no ions (or are present in a very small concentration) and electric fields present. Therefore, the substrate and the growing film are not damaged by energetic ion bombardment. This is important for depositing passivation or gas barrier films on organic devices. This can also be important when depositing the first part of the i-layer in pin-type solar cells, so as to avoid damage of the critical p/i-interface.
- Due to its high decomposition efficiency, the technique has the potential for high deposition rates (up to 10 nm/s).
- Due to the low pressures that are used for gas phase decomposition (some mTorr), a high flux of atomic hydrogen can be obtained; this can be useful for material etching, for removing dangling bonds, and for enhancing the abstraction of H atoms from the growing surface (leading, thereby, to a low H-content in the films and to a premature $\alpha \rightarrow \mu\text{c}$ transition). At the same time, the formation of SiH_3 , as growth pre-cursor, is favored due to H abstraction from SiH_4 : $\text{H} + \text{SiH}_4 \rightarrow \text{SiH}_3 + \text{H}_2$.
- Since no plasma is needed, the substrate is decoupled from the deposition process, enabling substrates to be easily introduced and removed from the deposition chamber without disturbing the deposition. Moreover, step coverage (conformal film deposition) is excellent [7], and uniformity can easily be optimized.
- It is a method that is easily scalable by expanding the spanned area of the catalyst; this fact is particularly important for industrial implementation.

2.2.2 Filament materials

Over the last years, tungsten (W), which was previously the filament material most frequently used, has gradually been replaced by tantalum (Ta), essentially when silane flow is used. The replacement was motivated by the following consideration: to avoid

filament aging, it is important to avoid the formation of silicides on the filament surface. Now, the formation of Ta-silicide takes place at lower temperatures (only up to 1750 °C under silane flow) when compared to the formation of W-silicide (up to 1850°C) [8]. Apart from these two materials, ruthenium (Ru), rhenium (Re), iridium (Ir), molybdenum (Mo), graphite (C) and a nickel-chromium alloy (NiCr) have also been used occasionally as filament materials [3].

2.2.3 Types of materials deposited by HWCVD

The great majority of research activities on Hot-Wire deposition have so far been devoted to gas phase and deposition chemistry of silicon-related materials: hydrogenated amorphous silicon, microcrystalline silicon, polysilicon, epitaxial silicon, silicon alloys with carbon, nitrogen and germanium. This research has also been done in view of applying these materials, for instance, in solar cells and thin film transistors. Since 2004, an increasing variety of thin-film materials have been obtained with the HWCVD method, namely: silicon dioxide, aluminum oxide, aluminum nitride, Si-O-C, Si-N-C alloys, diamond, carbon nanotubes, nanowalls or nanoparticles. Moreover, transition metal oxide nanoparticles have been synthesized for applications like gas sensors or electrochromic windows. A novel HWCVD variant, called “initiated CVD (iCVD)”, appeared in 2006, and has spread rapidly [9]. It was demonstrated to be a convenient single-step fabrication method to produce high-quality polymer thin films.

2.2.4 Mechanisms of the deposition process

Looking specifically at the deposition of a-Si:H layers, several researchers have attempted to undertake a systematic study of the deposition process mechanisms for HWCVD [10-13]. Optimum conditions for the deposition of amorphous silicon films have been obtained [11] for a particular value of the gas phase parameter $p \times L$, i.e. for $p \times L \sim 20-75$ mTorr.cm, where p is the silane chamber pressure in mTorr, and L is the distance in cm between filament and substrate. They postulated that this optimum results from the need to increase the pressure to a level where most Si atoms react with SiH₄ before reaching the substrate, while avoiding excessive gas phase reactions that can lead, at still higher pressures, to the formation of large radicals, such as Si₂H₆ and

Si_3H_8 . SiH_3 is considered to be a “good” film growth pre-cursor [14] because it has high surface mobility and has the longest lifetime among the various SiH_n -type species; in contrast to SiH_2 , it does not lead to the formation of large radicals.

The formation of radicals (especially of those radicals that are growth precursors) is an essential point when studying the deposition of thin-film silicon layers. Radical formation has been studied by various methods, as follows:

The nature and the flux of radicals desorbed from a hot filament depend on the filament temperature and on the gas pressure in the reactor. In the case of a tungsten filament heated at 1900 °C in a low pressure of silane, most of the authors agree that, using different detection methods, one does detect different radical species, namely Si, H and SiH_3 . Using threshold ionization mass spectrometry, H and Si were found as primary radicals with a small contribution of SiH_3 [10, 15] for a large range of temperatures (1450 to 2700 °C) and for H_2 pressures up to 0.1 Torr, whereas using single-photon ionization with a vacuum ultraviolet laser, gas-phase species identified were Si, SiH, and Si_2H_6 [12]. In the latter case H was not detected because the ionization potential for H exceeded the photon energy of the laser. Moreover, considering newly replaced (“virgin”) filaments, the small activation energy (8 kcal/mol) then observed for SiH_3 formation suggested that the process was “catalyzed” [13].

The absolute density of H-atoms in the gas phase has been determined by combining a two-photon laser-induced fluorescence technique and a vacuum ultraviolet (Lyman α) absorption technique [16]. At high temperatures of the tungsten wire (~1930 °C), the absolute density of H-atoms reached values that were as high as $1.0 \times 10^{14} \text{ cm}^{-3}$. These values are two orders of magnitude higher than those obtained by PECVD under comparable conditions. The effective enthalpy for the H-atom formation from H_2 on the catalyst surface was determined to be 57.1 kcal/mol [16] and should be compared with the effective bond dissociation energy of gas-phase H_2 molecules, which is 109.5 kcal/mol. This result established clearly the catalytic nature of the hot-wire CVD process.

As concerns the mechanism of H-atom formation by HWCVD, it was demonstrated that this mechanism proceeded via dissociative adsorption at bare sites followed by desorption at hydrogenated sites on the hot wire surface [17].

2.2.5 Filament aging

It has been suggested [18] that the electronic properties of a-Si:H deposited by HWCVD are related to radical chemistries, and that the differences observed in thin-film properties are linked to the differences between a “virgin” wire and an aged wire. For an aged wire, the SiH₃ signal exhibited an activation energy of 106 kcal/mol: a value that is much higher than the 8 kcal/mol observed for a “virgin” wire. This suggests that the aging of the wire leads to a drastic reduction of its catalytic activity [13]. Also SiH and SiH₂ are now more abundant than SiH₃, in contrast with the results obtained when a “virgin” filament is used [13].

To gain insight into the nature of the changes occurring at the wire surface, scanning electron micrographs and Auger electron spectroscopy were used to characterize the surface morphology of heat-treated and aged wires, and to measure the Si concentrations at the surface and in the interior of the wire, respectively. A Si concentration of 15 at.% was observed at the surface of an aged wire, corresponding to a two-phase equilibrium between tungsten silicide (W₅Si₃) and tungsten, whereas approximately 2 at.% Si concentration was measured in the interior of the wire, a value that is comparable to the equilibrium solid solubility of Si in W [13].

Using a tantalum filament exposed to a silane pressure of 0.25 Torr [19], the formation of a Ta₅Si₃ shell (as determined by X-ray diffraction) of 20 μm thickness was observed. After 4 hours of annealing of the filament in vacuum at high temperature (2100 °C), the tantalum silicide was completely removed. This regeneration procedure was shown to greatly enhance the lifetime of the Ta filaments.

Based on these results, a Ta filament was used in all HWCVD depositions in the present work.

2.3 CVD deposition systems

2.3.1 The CVD deposition system at Universidade do Minho

Figure 2.5 shows a picture of the CVD deposition system used at Universidade do Minho for the development of silicon thin films, piezoresistive sensors and solar cells. The CVD deposition system consists of twin chambers in cylindrical format, made of stainless steel, with *conflat* flanges and metallic seals of copper gaskets, for rf-PECVD

and HWCVD deposition. These two chambers are connected in series with a load lock chamber. A manually controlled transfer arm is used for loading and unloading a single sample holder each time.

The pumping systems are independent for the three chambers and consist of turbomolecular pumps backed by rotary pumps. Gate valves isolate the chambers from each other and from the pumps, when necessary. The chambers are pumped by turbomolecular pumps, assisted by rotary vane pumps. The base pressure in each chamber is lower than 10^{-7} Torr. The pressure is measured by Penning and Pirani gauges, and controlled by a manual needle valve.

The gas supply to the chambers is carried out in the cross-flow mode by stainless steel gas lines and the flow is controlled by Mass Flow Controllers (MFC). The substrate temperature is controlled by a Eurotherm unit connected to a thermocouple and a heater.

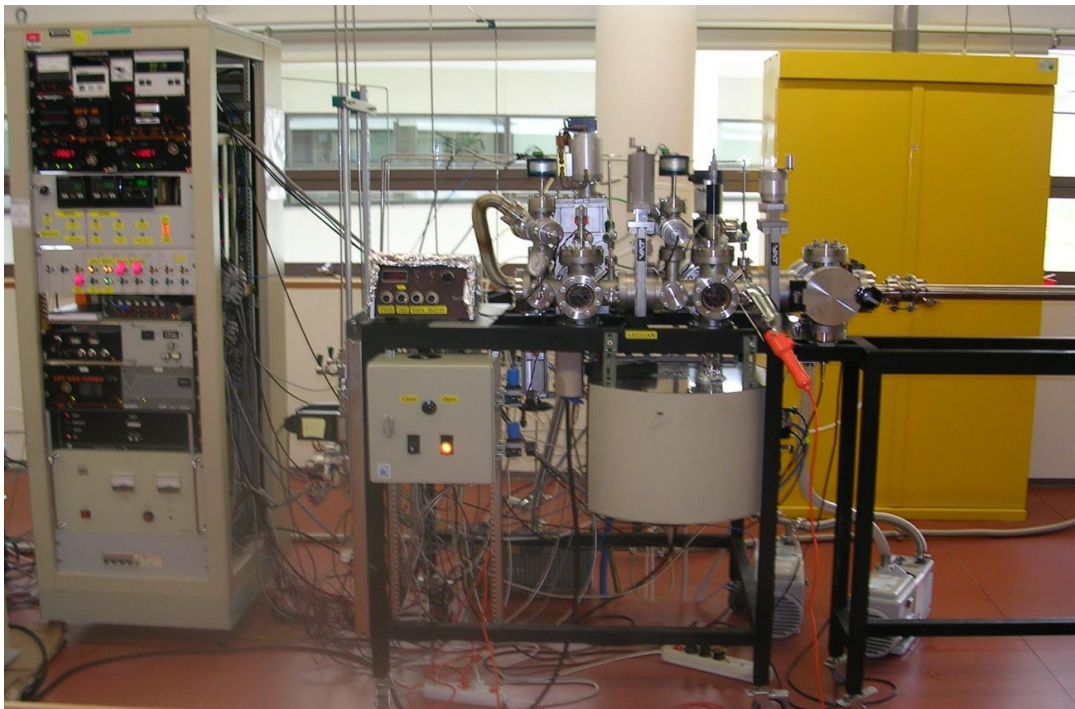


Fig. 2.5: The CVD deposition system at Universidade do Minho consists of two UHV chambers assisted by a load lock chamber. The chamber in left is for HWCVD depositions, and the chamber in the right is for rf-PECVD depositions.

In the rf-PECVD chamber (right side in fig 2.5), a conventional design with two parallel capacitive electrodes is used for the radio-frequency (13.56 MHz) discharge. The power is supplied through the lower electrode. The sample is attached to the upper electrode, which is kept in earth potential by a feedthrough connected outside the

system. The power source is connected to a tune unit with a variable reactance, which is adjustable in order to eliminate the power reflected by the circuit.

In the HWCVD chamber (left side in fig. 2.5), the substrate holder is placed 5 cm above a single tantalum filament ($\varnothing = 0.5$ mm, 14 cm long) that is bent in S shape and fixed at its ends by support bars and ceramic pieces. The filament is resistively heated for deposition, using a DC power supply that pyrolytically decompose the reactant gases at the filament surface.

2.3.2 The CVD deposition system at Forschungszentrum Jülich

Figure 2.6 shows a drawing of the cluster tool deposition system used to prepare individual layers and solar cells at Forschungszentrum Jülich [42]. The deposition system is a multi-chamber system, it consists in total of seven chambers, which are connected to the transfer chamber (TC). The transport of the samples between the chambers is carried out by a robotic arm located in the transfer chamber. The loading chamber MC1 can simultaneously load six substrates of 10×10 cm². The substrates are driven individually without breaking the vacuum, from the loading chamber into the transfer chamber and to the deposition chambers. The heater station (HS) which, in contrast to the other chambers, is not separated from the transfer chamber by a gate valve, is used to pre-heat the substrates before each deposition. Alternatively, the substrates are pre-heated in an unused deposition chamber. Chamber MC2 is another loading chamber, loaded with one single substrate. In the event of a possible expansion of the deposition system, another cluster tool can be connected through the chamber MC2, which might be used as the transfer chamber between two cluster tool deposition systems. The chambers PC1, PC2 and PC3 are identically structured PECVD process chambers. Chamber PC1 is used to deposit doped layers. In chamber PC2 intrinsic layers are deposited, chamber PC3 is adapted for the processing of silicon alloys. Chamber PC4 is a HWCVD process chamber for the deposition of intrinsic microcrystalline layers. PC5 is a sputtering chamber used for TCO deposition. With exception of the HS chamber, all the process chambers have a multistage pumping system, which consists of a turbo-molecular pump, roots pump and a rotary vane pump. By this configuration, pressures are in the range of Ultra High Vacuum. The pressure is

measured by Penning and Pirani gauges, which depending on the measurement range will automatically switch between each other.

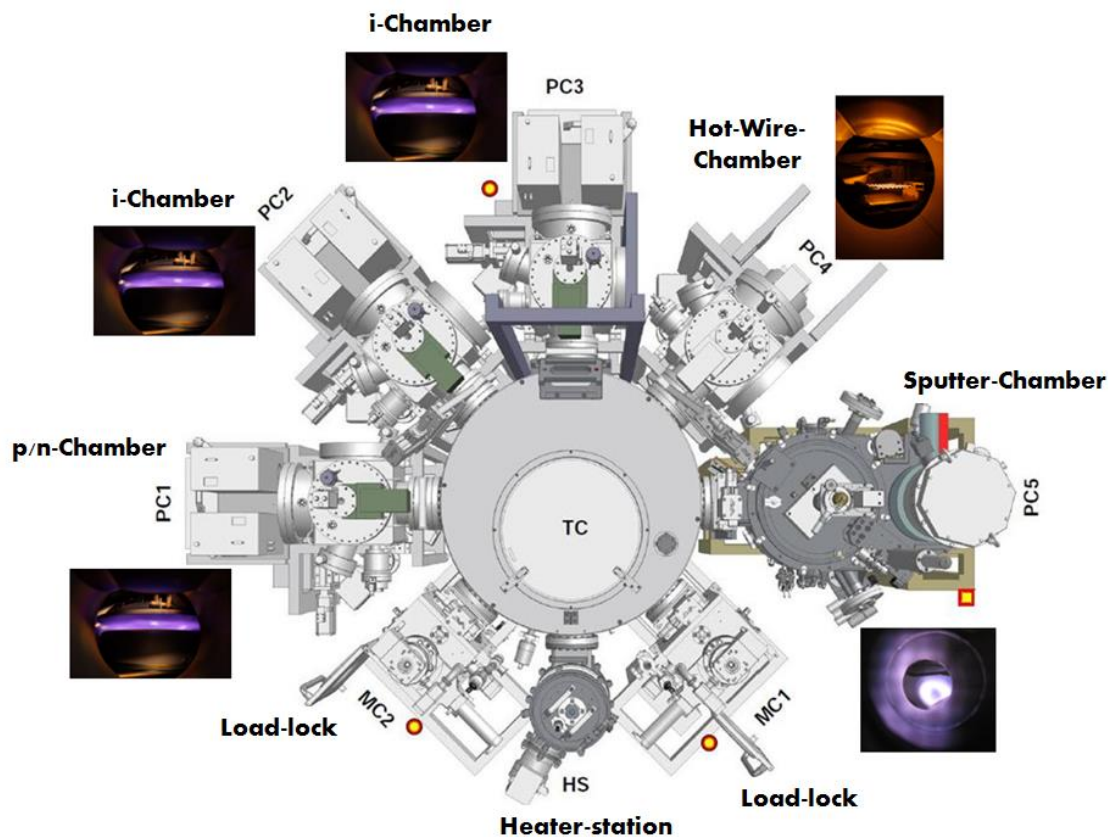


Fig. 2.6: Schematic of the cluster-tool deposition system used at Forschungszentrum Jülich (adapted from [42]).

Figure 2.7 shows schematically the structure of a process chamber. The chambers PC1, PC2 and PC3 have a parallel plate configuration. The power input is delivered by a copper strip connected below the RF / VHF electrode. The substrate holder, made of stainless steel, is located above the electrode and acts as a grounded electrode. A shutter, located just below the substrate is opened only when the plasma burns stable and homogeneously. The distance between the substrate and electrode can be varied between 5 mm and 20 mm. The heater is mounted over the substrate, which is pressed against the heater so that there is a sufficiently good thermal contact between heater and substrate. The working temperatures are measured by two thermocouples. One of the thermocouples is in the heater shed, the second is attached to the side of the heater.

The gas supply to the chambers is carried out either via showerhead mode or in the cross-flow mode. Because of the generally better layers homogeneity, all the samples prepared with the cluster tool system were processed in the showerhead mode.

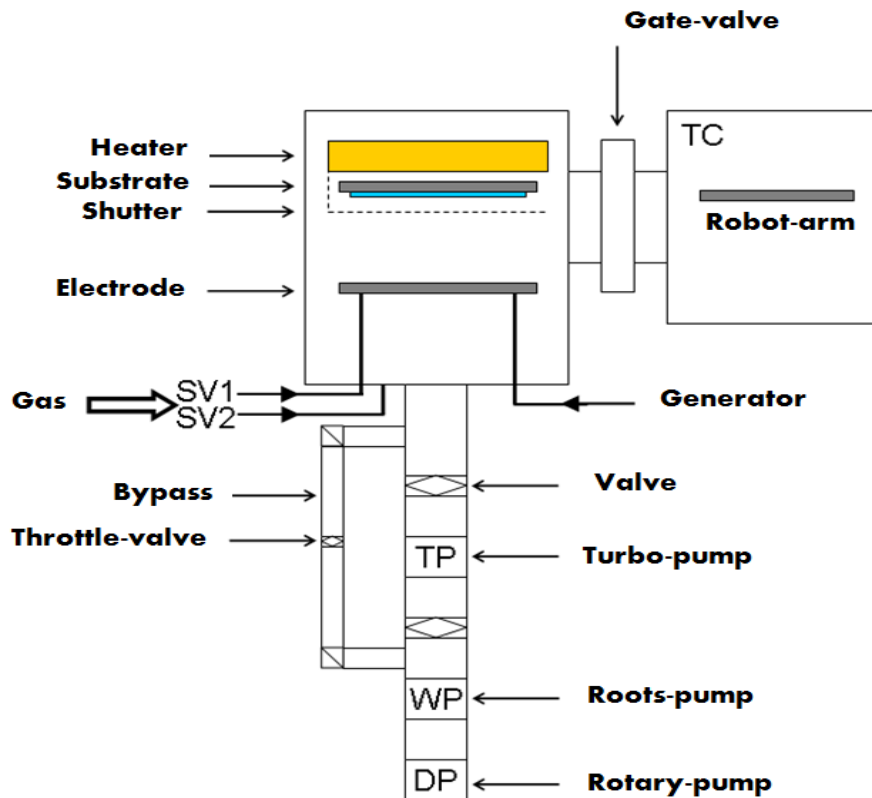


Fig. 2.7: Schematic of a process chamber in the cluster-tool deposition system (adapted from [42]).

For safety reasons, the process gases are stored outside the laboratory. Using appropriate gas lines, the process gases are conducted to a gas distribution system within the laboratory. The flow of any process gas can be set and regulated by a mass flow controller. The process gases are combined into each chamber by the valves SV1 and SV2. A separate argon (Ar) gas line is available in order to flush the line and the chamber after each process step. The flow can also be adjusted using a MFC.

2.4 Optical transmittance spectroscopy

The common parts of UV-VIS-NIR spectroscopy techniques are light sources, beam splitter or diffraction gratings, sample holders and detectors. The intensity (I_0) of the incident light after passing through the sample is changed to a lower value (I) due to the absorption within the sample and/or reflection at the interfaces. The transmission or absorption spectrum of a specific sample (thin film on a substrate) contains information about the optical parameters of the film when compared with a reference sample.

In this work, a dual beam UV-VIS-NIR spectrometer set-up is used to characterize silicon thin films. Reference sample (substrate) and the studied sample (substrate with

silicon film) are put into two different sample holders. The light beam of wavelength ranging from 250-3200 nm is split in two beams that simultaneously passed through each sample. The difference between the reference beam and the beam coming from the sample containing the film is recorded in the form of a spectrum. Depending on the film thickness, interference fringes appear in the recorded spectrum. The appropriate analysis of this spectrum yields the optical parameters of the film material. A typical transmission spectrum of a film on a glass substrate is shown in figure 2.8. Oscillations in the transmission spectra are observed due to interference effects in the film [20].

The optical parameters of the film can be calculated using the Swanepoel method [43] from the transmission spectra. Thickness (d), refractive index (n), and absorption coefficient (α) of the film can be evaluated using this method. The basic equation for interference fringes is:

$$2nd = m\lambda \quad (2.1)$$

where m is an integer for maxima and half integer for minima, n is refractive index, d is the thickness of the film, and λ is wavelength. The transmission T for the normal incidence resulted from the interference of the wave transmitted from three interfaces can be written as [43]:

$$T = T(n, x) = \frac{Ax}{B - Cx \cos(\phi) + Dx^2} \quad (2.2)$$

where

$$A = 16n^2s \quad (2.3a)$$

$$B = (n + 1)^3(n + s^2) \quad (2.3b)$$

$$C = 2(n^2 - 1)(n^2 - s^2) \quad (2.3c)$$

$$D = (n - 1)^3(n - s^2) \quad (2.3d)$$

$$\phi = 4\pi nd/\lambda \quad (2.3e)$$

$$x = \exp(-\alpha d) \quad (2.3f)$$

For maximum and minimum points of interferences $\cos(\phi) = 1$, so T_M and T_m curves as the upper and lower bounding functions of transmittance can be found by fitting the two below curves to these points as

$$T_M = \frac{Ax}{B-Cx+Dx^2} \quad (2.4)$$

$$T_m = \frac{Ax}{B+Cx+Dx^2} \quad (2.5)$$

If T_s , shown by dotted line in figure 2.8, is the maximum value of the transmission of substrate, then substrate refractive index s can be given by the following equation:

$$s = \frac{1}{T_s} + \left(\frac{1}{T_s^2} - 1 \right)^{1/2} \quad (2.6)$$

The upper bounding function T_M passes through the maxima of the spectrum and T_m through the minima as shown in figure 2.8.

From equations 2.4 and 2.5, we have

$$\frac{1}{T_m} - \frac{1}{T_M} = \frac{2C}{A} \quad (2.7)$$

The right hand side of equation 2.7 is independent of the thickness of the film. Substituting C and A from equation 2.3 into equation 2.7 leads to:

$$n = [N + (N^2 - s^2)^{1/2}]^{1/2} \quad (2.8)$$

where

$$N = 2s(T_M - T_m)/T_M T_m + (s^2 + 1)/2 \quad (2.9)$$

If n_1 and n_2 are the refractive indices calculated from two consecutive maxima or minima corresponding to two wavelengths of λ_1 and λ_2 , then the film thickness can be obtained from [43]:

$$d = \frac{\lambda_1 \lambda_2}{2(\lambda_1 n_2 - \lambda_2 n_1)} \quad (2.10)$$

The thickness obtained from equation 2.10 is very sensitive to the uncertainty in the value of the refractive index which is derived from equation 2.8.

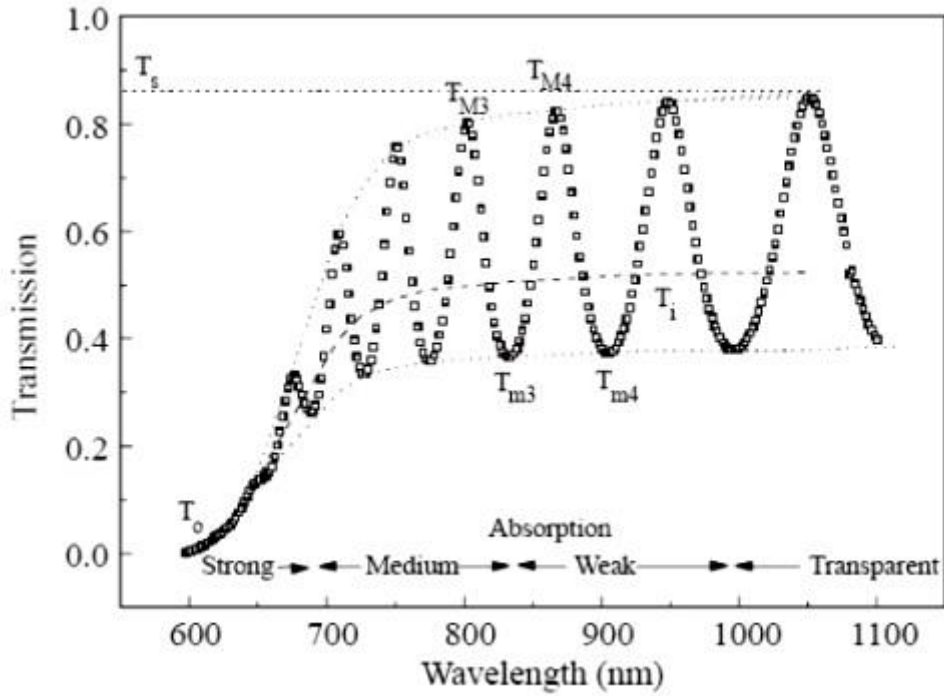


Fig. 2.8: Experimental transmission spectrum of a silicon thin film on glass substrate. T_{Mi} , T_{mi} are the maxima and minima (from [43]).

The absorption coefficient can be obtained from the formula:

$$\alpha d = -\ln \left[\frac{T}{(1-R)^2} \right] \quad (2.11)$$

where R is the reflectance. The value of the optical band gap (E_g), a parameter characteristic of amorphous silicon can be obtained by plotting the absorption coefficient as a function of photon energy using the Tauc equation [21, 22]:

$$\sqrt{\alpha h\nu} = B(h\nu - E_g^{opt}) \quad (2.12)$$

where E_g^{opt} denotes what is generally called “the Tauc optical gap” and B is an empirical constant. It defines the optical band gap in amorphous semiconductor materials. It should be borne in mind that the so called “Tauc-plot” shown in figure 2.9 is valid in a limited region of the photon energies, roughly between E_g^{opt} and below the E_1 transition (3.45 eV for a-Si:H) [23]. As one can see from figure 2.9, the Tauc-plot of the transmittance spectra of thin films contains interference fringes that make it difficult to obtain an accurate Tauc gap value. This results in an uncertainty in the obtained

optical band gap values for thin films. The correct procedure requires full modeling of the spectra which involves calculations of the complex dielectric function of the material in the vicinity of the optical gap. In this work we used envelope curves drawn by hand over the interference fringes in the measured spectra in order to reduce the uncertainty mentioned above.

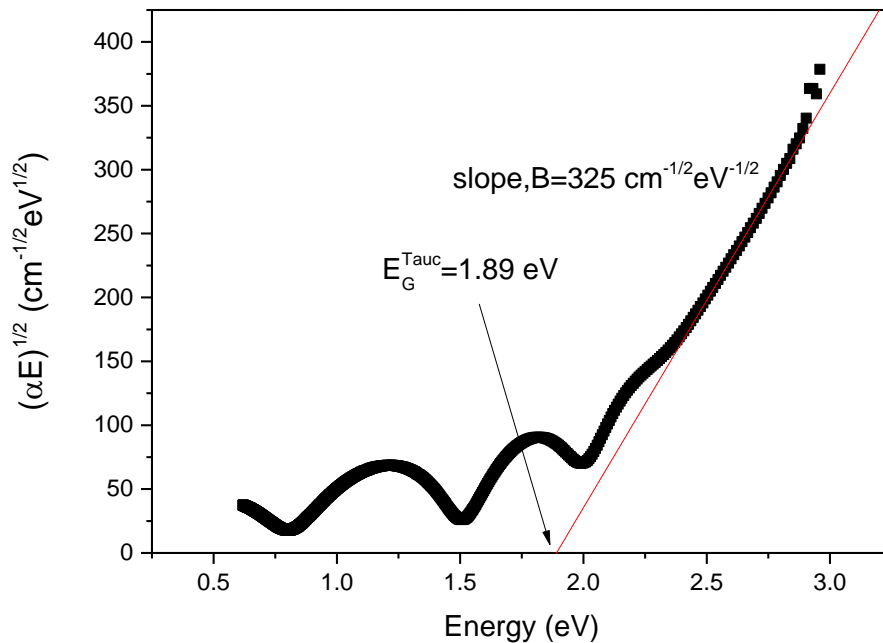


Fig. 2.9: Example of a Tauc-plot to obtain optical band gap and B .

The slope of the straight line drawn on to the x -axis gives the B value. In some cases, B values can be related to the photoconductivity of the materials. The intercept of the straight line with horizontal axis gives the Tauc-band gap value for the particular amorphous material.

2.5 Structural and chemical characterization

2.5.1 Raman Spectroscopy

Raman Spectroscopy is used to obtain information about the crystalline volume fraction of thin film silicon material [24]. Laser light with a well defined frequency is incident on the material. By far most of the photons scatter elastically (Rayleigh

scattering) and a small part of the light scatters inelastically, which leads to a frequency shift:

$$h\nu_s = h\nu_0 \pm \Delta E \quad (2.13)$$

where $h\nu_s$ is the energy of the scattered light, $h\nu_0$ the energy of the incident light and ΔE the energy shift that corresponds to the energy of a phonon that has been created (Stokes scattering) or annihilated (anti-Stokes scattering).

The Raman shift spectrum reflects the phonon density of states. Within the detected spectral range the transverse-optic (TO) mode of crystalline silicon is visible (520 cm^{-1}) as well as the transverse-acoustic (TA), longitudinal-acoustic (LA; 330 cm^{-1}), longitudinal-optic (LO; 445 cm^{-1}) and TO (480 cm^{-1}) modes of amorphous silicon. Consisting of amorphous tissue and crystallites, $\mu\text{c-Si:H}$ simultaneously shows a crystalline peak and an amorphous peak in the Raman spectrum. In addition, a third peak at around 500 cm^{-1} is often observed in the Raman spectra of $\mu\text{c-Si:H}$. This peak was previously attributed to the stacking faults or hexagonal silicon [24, 25].

Fitting three Gaussian peaks the Raman spectra is an easy way to determine the integrated intensities of crystalline and amorphous peaks. The integrated intensity ratio of the Gaussian peaks, X_c , can be used as a semi-quantitative value for crystalline volume fraction. This ratio is defined by the contributions of the different phases to the TO mode:

$$X_c = \frac{I_{510} + I_{520}}{I_{480} + I_{510} + I_{520}} \quad (2.14)$$

where I_x denotes the integrated intensity of the contribution centered around $x \text{ cm}^{-1}$. I_x can be determined by means of a deconvolution of the Raman spectrum. Note that X_c is only a semi-quantitative value, since the Raman cross sections are different for crystalline and amorphous phase, and may depend on the excitation wavelength. Furthermore, the absorption coefficient difference in the crystallites and in the amorphous phase makes it more difficult to determine the real crystalline volume fraction from Raman spectra. Still, Raman spectroscopy is a simple and useful method to provide the structure information of the material, and thus is widely used.

2.5.2 Fourier-Transform Infrared Spectroscopy (FTIR)

Various hydrogen related bonding configurations can be distinguished by Fourier-Transform Infrared Spectroscopy (FTIR). Vibrational modes of non-symmetric (polar) bonding configurations are reflected in the IR absorption spectra. The magnitude of the absorption related to a certain mode is a measure for the number of associated bonds present in the material. The proportionality constant is dependent on the oscillator strength of the bond.

The thin films to be analyzed are deposited on a low resistivity c-Si wafer. The measurements are performed with a spectrometer that is based on the principle of a Michelson interferometer: the absorption spectrum is obtained by Fourier-transforming the complex interference of two beams reflected at a fixed and a moving mirror, respectively.

The absorption spectrum of the sample is corrected for the absorption of the substrate that is measured as a reference. The recorded spectra are corrected for multiple reflections in the substrate [26] and coherent reflections within the layer [27]. Si–H bonds in the rocking mode at 640 cm^{-1} and the stretching mode at 2000 and 2100 cm^{-1} are analyzed. The hydrogen concentration is calculated from the rocking mode with the proportionality constant $2.1 \times 10^{19}\text{ cm}^{-2}$ [28].

The microstructure factor R^* is defined by the fraction of the Si–H stretching mode bonds that are in the 2100 cm^{-1} mode. The 2100 cm^{-1} mode is attributed to Si–H₂ bonds or to Si–H bonds at grain surfaces or large internal voids. A high microstructure factor is associated with an open material structure or to a high microcrystalline fraction.

2.6 Electrical Material Characterization

2.6.1 Dark Conductivity

In device-quality material, electronic transport in hydrogenated amorphous silicon layers (and also in hydrogenated microcrystalline silicon) is very similar to transport in classical, crystalline semiconductors.

It can therefore be well described by the so-called “standard transport model”. In this model, both free electrons, i.e. electrons within the conduction band, as well as free holes, i.e. holes within the valence band, travel by drift and/or by diffusion from one

place to the other. On the other hand, localized electrons and holes (i.e. electrons and holes trapped in their respective bandtails) do not contribute to the current. Thus, one has for the respective electrical current densities [3]:

$$J_n = q\mu_n^0 n_f E + D_n \partial n_f / \partial x \quad (2.15)$$

and

$$J_p = q\mu_p^0 p_f E - D_p \partial p_f / \partial x \quad (2.16)$$

where q is the unit charge (charge of an electron), μ_n^0 is the band mobility of electrons, μ_p^0 the band mobility of holes, n_f the density of free electrons, p_f the density of free holes, E the electric field prevailing at the point considered, D_n the diffusion constant of electrons, and D_p the diffusion constant of holes.

The measurement of the dark conductivity of thin-film silicon layers is a basic and important evaluation technique. For electrical measurements of the thin-film silicon layers deposited on glass and on plastics, two coplanar metallic contacts are evaporated parallel to each other. By applying a voltage V between the electrodes, and measuring the resulting electrical current I in the dark, assuming the cross-section to simply be the product of the thickness of the layer and of the side length of the rectangular contact pad, the dark conductivity σ_d can be determined by the following equation:

$$\sigma_d = \frac{Iw}{Vld} \quad (2.17)$$

where d is thickness, w is distance between the contacts, and l is contact length.

The value σ_d of the dark conductivity is generally found to vary exponentially with the absolute temperature T (in Kelvin), i.e. we generally have a temperature dependence of the form

$$\sigma_d(T) = \sigma_0 \exp \frac{-E_a}{kT} \quad (2.18)$$

where σ_0 is called the “conductivity prefactor”, k is the Boltzmann factor and E_a is denoted as “activation energy”.

By plotting the measured values $k \times \ln \sigma_d$ versus $(1/T)$, we obtain (more or less) a straight line. In a first approximation, the extrapolation of this line to $T = 0$ gives us the conductivity prefactor σ_0 , and the slope of this line, also called the activation energy E_a

of the dark conductivity, gives us the value $E_C - E_F$, or the value $E_F - E_V$, i.e. the position of the Fermi level E_F , with respect to the nearest band edge.

2.6.2 Photoconductivity

The photoconductivity is an optoelectronic phenomenon consisting in an increased electrical conductivity of a material when exposed to light. When the material absorbs electromagnetic radiation, i.e. photons, there is an increase of the number of free charge carriers (i.e. creation of electron-hole pairs) and, consequently, an increase in the electrical conductivity of the material. In order to produce the excitation of extra charge carriers, the light beam is focused on the sample surface and the photons should have enough energy to cause the transition of electrons from valance band to conduction band. This means that only the photons with energy higher than that of the optical gap are absorbed in substantial quantity.

The photoconductivity is given by the following formula:

$$\sigma_{ph} = q(\mu_e \Delta n + \mu_h \Delta p) \quad (2.19)$$

Δn and Δp denote the concentrations of the photogenerated carriers which are determined by the balance between the generation and recombination processes [29]. μ_e and μ_h are mobilities of electrons and holes, respectively. The recombination of charge carriers out of equilibrium is usually characterized by so called carrier lifetime. Strictly speaking, the lifetime can be introduced only for minority carriers and under some approximations [29]. If we assume that they are satisfied, the concentration of the (photogenerated) minority carriers, at steady state conditions can be expressed as:

$$\Delta n = G\tau_e \quad (2.20)$$

G is the generation rate of charge carriers per unit volume and τ_e is the electron lifetime (we just assumed that electrons are the minority carriers). The generated free carriers can recombine through recombination centers present in the material. The electronic states related to defects, voids, dangling bonds and other deep centers, act as recombination centers.

In the case of a-Si:H and μ c-Si:H films, it is known that the photoconductivity mechanism is dominated by the electrons, due to their higher mobility. Then eq. (2.19) can be written as:

$$\sigma_{ph} = Gq(\mu_e \tau_e) \quad (2.21)$$

However, in reality, the dependence of the photoconductivity on the generation rate, G , is not exactly linear as suggested by eq. (2.21). A more general power law has been established [30],

$$\sigma_{ph} \propto G^\gamma \quad (2.22)$$

where γ is a critical exponent of the power law. The values of γ for films of hydrogenated amorphous and microcrystalline silicon are around 0.5 and 1, respectively [29].

2.6.3 Constant Photocurrent Method (CPM)

The constant photocurrent method (CPM) allows to measure the absorption coefficient for values of $\alpha \cdot d \ll 1$ down to $\alpha \sim 10^{-2} \text{ cm}^{-1}$. Here, one measures the photoconductivity that has been induced by the absorption of the light at different wavelengths: under certain circumstances, the value of the photoconductivity of a semiconductor layer can be considered to be roughly proportional to the light absorbed and to the density of charge carriers generated within the layer. In the CPM measurement these circumstances are fulfilled because the generation rate is constant, which fixes the pseudo-Fermi levels for both electrons and holes (By means of an electronic regulation circuit, the photocurrent is kept constant and one correspondingly modulates the amplitude of the monochromatic light for which one wishes to measure the absorption. If the absorption coefficient is low at that specific wavelength, then a high light intensity is required to obtain the fixed value of the photocurrent; if, on the other hand, the absorption coefficient is high, then a low value of light intensity will be sufficient. As one keeps the photocurrent (i.e. the density of charge carriers) constant, it is not necessary to have an exact proportionality between the photoconductivity and the density of charge carriers. As both electrons and holes contribute to the

photoconductivity, although in a slightly different manner, the CPM technique depends, to a slight extent, on the position of the Fermi level E_F . The basic CPM technique is explained in more detail in [31].

A CPM spectrum can be divided into three parts: in the low energy range, the absorption by defects dominates the evolution of α . Towards higher energy, α increases exponentially with energy, this part is labeled Urbach tail. Here, mainly electron excitation from valence band tail to the conduction band take place. The reciprocal slope of the absorption coefficient in the Urbach tail region is known as Urbach energy E_U . The Urbach tail region is followed by higher band-to-band transitions with corresponding energies.

As a measure of the integrated defect density N_d in a-Si:H, one can take the absorption coefficient, α_d , at the photon energy of 1.2 eV [32]: $N_d = \alpha_d \times C_d$, where C_d is a correction factor [33]. Good values for the defect density and E_U in a-Si:H are around 10^{16} cm^{-3} and below 50 meV, respectively.

2.7 Solar Cell Characterization

2.7.1 Current-Voltage Measurements (IV)

The electrical output of solar cells is characterized by analyzing current density vs. voltage (JV) measurements. The J-V measurements are normally performed in a solar simulator under illumination calibrated to the AM1.5 spectrum [34] (integrated power is 100 mW/cm^2). Ideal solar cells show the behavior of an equivalent circuit (fig. 2.10) consisting of a photocurrent J_{ph} source, a diode and a resistance R_p in parallel, connected in series with a resistance R_s .

The current density is well described by [35]:

$$J(V) = -J_{ph} + J_0 \left[\exp\left(\frac{e(V-JR_s)}{nkT}\right) - 1 \right] + \frac{V-JR_s}{R_p} \quad (2.23)$$

where J_0 is the dark saturation current, n is the diode quality factor (close to 1 for diffusion-type cells and close to 2 for drift-type cells), k is the Boltzmann factor, and T the absolute temperature.

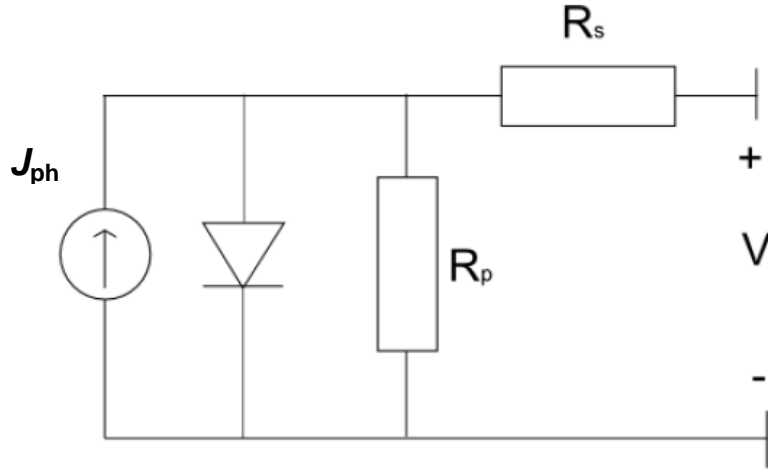


Fig. 2.10: Equivalent circuit of a solar cell with a diode, photocurrent source (J_{ph}), parallel (R_p) and series resistance (R_s).

J_0 and n are derived from the dark J - V measurements ($J_{ph} = 0$). From the J - V characteristic under illumination, one can determine several parameters (see figure 2.11):

- The efficiency η is defined as the ratio of the maximum power generated by the device (given by $P_{max} = J_{max} \times V_{max}$) and the incident radiation power. The efficiency under AM1.5 illumination is the ultimate parameter characterizing each solar cell.
- The fill factor FF defined as

$$FF = \frac{V_{max} \times J_{max}}{J_{sc} \times V_{oc}} \quad (2.24)$$

gives a description of the "rectangularness" of the light JV characteristic and is an integral measure of the collection efficiency at the maximum power point.

- The short-circuit current density J_{sc} is the maximum current density generated by the device.
- The open-circuit voltage V_{oc} (voltage at $J = 0$ mA/cm²), is the maximum voltage generated by the solar cell under illumination. In first approximation, the voltage can be calculated from equation 2.23, using the assumptions of a constant photocurrent and $J_{ph} = J_{sc}$. Hence it follows (the parallel resistance is neglected):

$$V_{oc} = \frac{nkT}{e} \ln \left(\frac{J_{sc}}{J_0} + 1 \right) \quad (2.25)$$

It is clear from eq.(2.25) that in order to achieve a high open-circuit voltage it is necessary to have a low dark saturation current. The slope of the J-V curve at J_{sc} is associated with the parallel resistance R_p and the slope at V_{oc} with the series resistance R_s . In order to achieve a high fill factor and V_{oc} , the series resistance should be as small and the parallel resistance as high as possible.

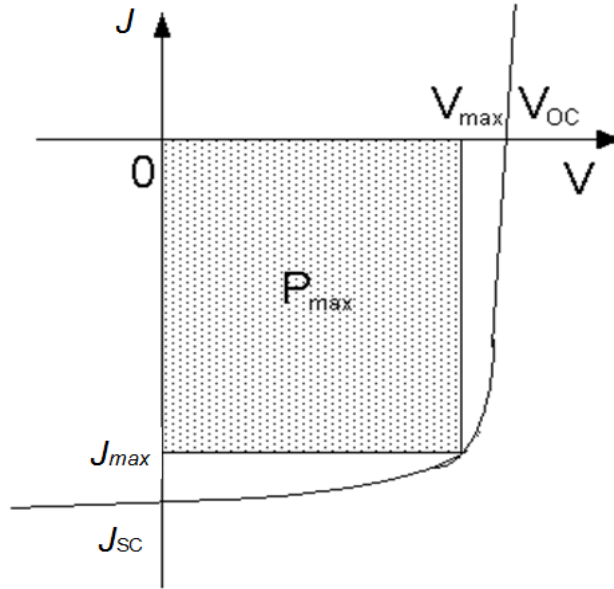


Fig. 2.11: Scheme of a light JV characteristic with important JV parameters (See text).

2.7.2 External Quantum Efficiency (EQE)

The External Quantum Efficiency (EQE) of solar cells is measured for light in the wavelength range 300–1100 nm by measuring the current that is generated by a monochromatic AC probe beam. The EQE is given by the number of collected electrons per incident photon:

$$EQE(\lambda) = \frac{J_{ph}(\lambda)/e}{\phi} \quad (2.26)$$

where e is the electron charge, J_{ph} the generated current density, and ϕ the photon flux incident on the sample. The total generated current density is given by the integral of the convolution of the EQE with the AM1.5 photon flux spectrum [35].

$$J_{ph} = e \cdot \int EQE(\lambda) \phi(\lambda) d\lambda \quad (2.27)$$

2.8 Piezoresistance

The application of pressure to the crystal structure of a semiconductor material temporarily alters its symmetry, and consequently modifies the conduction mechanism which is highly sensitive to these variations. The observed macroscopic effect is a resistivity variation [36]. This variation can be positive or negative; i.e., the pressure may cause either an increase or a decrease of resistivity, according to the material and the crystallographic direction along which it is applied.

The relation between resistivity and applied mechanical stress can be written as [37]:

$$\rho = \rho_0(1 + \pi_h \sigma_h) \quad (2.28)$$

where ρ_0 is sample resistivity at zero mechanical stress, σ_h is applied mechanical stress, and π_h depends upon the piezoresistivity coefficients π_{ij} through the relation:

$$\pi_h = \pi_{11} + 2(\pi_{44} + \pi_{12} - \pi_{11})(l^2 m^2 + l^2 n^2 + m^2 n^2) \quad (2.29)$$

in which l , m , n are the direction cosines of the direction h with respect to the crystallographic axes.

Piezoresistive effect in crystalline silicon is customarily measured using only two coefficients: π_l that relates the resistivity change due to stress in the longitudinal direction and π_t in the transverse direction. Therefore, the total resistivity change can be simplified considering only changes under longitudinal and transverse stress components:

$$\frac{\Delta\rho}{\rho_0} = \pi_l \sigma_l + \pi_t \sigma_t \quad (2.30)$$

The resistance variations of a sample of cross section A and length l , subjected to a mechanical stress along the longitudinal axis, are due to variations of the sample geometry and piezoresistivity effects [37]. We can therefore write:

$$\frac{\Delta R}{R_0} = \frac{\Delta l}{l} - \frac{\Delta A}{A} + \frac{\Delta\rho}{\rho} \quad (2.31)$$

where R_0 is sample resistance at zero stress, l is sample length, and A is sample cross section.

The dominant factor depends on the material type. For silicon the change in resistivity gives a larger contribution to the resistance changes than the change in dimensions of the resistor [36]. So that by introducing Young's modulus and considering that the components associated with dimension change can be written as a function of the strain, the equation (2.31) can be written as:

$$\frac{\Delta R}{R_0} = (1 + 2\nu)\varepsilon + (\pi_l E \varepsilon_l + \pi_t E \varepsilon_t) \quad (2.32)$$

where ν is the Poisson's ratio of the material, E is the Young's modulus, and ε is the strain.

Thus, the gauge factor, that is the ratio of relative change in electrical resistance to the mechanical strain ε , can be related to resistivity, strain and Poisson's ratio by the following equation [38]:

$$GF = \frac{1}{\varepsilon} \frac{\Delta \rho}{\rho_0} + (1 + 2\nu) \quad (2.33)$$

The piezoresistive effect has also been found in doped hydrogenated microcrystalline silicon thin films, $\mu\text{c-Si:H}$ [39, 40]. In particular, the combination of the mechanical properties of plastic substrates with the electrical properties of doped $\mu\text{c-Si:H}$ deposited at 100-150°C has proved to be a way to design new types of piezoresistive sensors [40, 41].

The piezoresistive behavior of n-type and p-type doped $\mu\text{c-Si:H}$ films deposited by rf-PECVD on Corning glass substrates at 200° C has been reported in the literature [39]. GF s between 16 and 23 and $-25 > GF > -40$ were obtained for p-type and for n-type films, respectively. These results show that the sign of the dominant piezoresistance coefficients of c-Si is preserved in high- T_{sub} microcrystalline silicon [40].

The piezoresistive property of p-type and n-type $\mu\text{c-Si:H}$ films deposited on plastic at 100° C by rf-PECVD and by HWCVD has also been reported [40]. For p-type films the GF was positive between 25–32 and for n-type films it was negative between 40 and 10.

The piezoresistive response characterization method is described in section 6.2.3.

References

- [1] R.C. Chittick, J.H. Alexander, H.F. Sterling, *J. Electrochem. Soc.* **116** (1969) p. 77.
- [2] W.E. Spear, P.G. LeComber, *Sol. State Comm.* **17** (1975) p. 1193.
- [3] A. Shah, ed., *Thin-film Silicon Solar Cells*, First edition, EPFL Press (2010).
- [4] H. Curtins, M. Favre, N. Wyrsh, M. Brechet, K. Prasad, A.V. Shah, In *Proceedings of 19th IEEE Photovoltaic Specialists Conference*, New Orleans, LA, USA (1987) p. 695.
- [5] H. Matsumura, K. Ohdaira, *Thin Solid Films*, **516** (2008) p. 537.
- [6] M. Kondo, T. Matsui, Y. Nasuno, H. Sonobe, S. Shimizu, *Thin Solid Films*, **501** (2006), p. 243.
- [7] Q. Wang, S. Ward, L. Gedvilas, B. Keyes, E. Sanchez, S. Wang, *Applied Physics Letters*, **84** (2004) p. 338.
- [8] K. Honda, K. Ohdaira, H. Matsumura, *Japanese Journal of Applied Physics*, **47** (2008), p. 3692.
- [9] K.K.S. Lau, K.K. Gleason, *Thin Solid Films*, **516** (2008) p. 678.
- [10] J. Doyle, R. Robertson, G.H. Lin, M.Z. He, A. Gallagher, *Journal of Applied Physics*, **64** (1988) p. 3215.
- [11] E.C. Molenbroek, A.H. Mahan, E.J. Johnson, A.C. Gallagher, *Journal of Applied Physics*, **79** (1996) p. 7278.
- [12] H.L. Duan, G.A. Zaharias, S.F. Bent, *Applied Physics Letters*, **78** (2001) p. 1784.
- [13] J.K. Holt, M. Swiatek, D.G. Goodwin, H.A. Atwater, *Journal of Applied Physics*, **92** (2002) p. 4803.
- [14] M. Kondo, T. Matsui, Y. Nasuno, H. Sonobe, S. Shimizu, *Thin Solid Films*, **501** (2006) p. 243.
- [15] W. Zheng, A. Gallagher, *Surface Science*, **600** (2006) p. 2207.
- [16] H. Umemoto, K. Ohara, D. Morita, Y. Nozaki, A. Masuda, H. Matsumura, *Journal of Applied Physics*, **91** (2002) p. 1650.
- [17] D.W. Comerford, J.A. Smith, M.N.R. Ashfold, Y.A. Mankelevich, *The Journal of Chemical Physics*, **131** (2009) p.44326
- [18] A.H. Mahan, A. Mason, B.P. Nelson, A.C. Gallagher, In *Proceedings of Materials Research Society Symposium*, **609** (2000), p. A6.6.1.
- [19] C.H.M. van der Werf, H. Li, V. Verlaan, C.J. Oliphant, R. Bakker, Z.S. Houweling, R.E.I. Schropp, *Thin Solid Films*, **517** (2009) p. 3431.
- [20] D.Y. Song, et al., *Appl. Surf. Sci.* **195** (2002) p. 291.
- [21] T.V. Herak, et al., *J. Non-Crystalline Solids*, **69** (1984) p. 39.
- [22] J. Robertson, *Phil. Mag. B*, **63** (1991) p. 47.
- [23] S. Adachi, et al., *Phys. Rev. B*, **66** (2002) p. 153201.

- [24] L. Houben, M. Luysberg, P. Hapke, R. Carius, F. Finger, and H. Wagner, *Philos. Mag. A* **77** (1998) p. 1447.
- [25] R. Kobliska and S. Solin, *Phys. Rev. B*, **8** (1973) p. 3799.
- [26] M.H. Brodsky, M. Cardona and J.J. Cuomo, *Phys. Rev. B*, **16** (1977) p. 3556.
- [27] N. Maley, *Phys. Rev. B*, **46** (1992) p. 2078.
- [28] A.A. Langford, M.L. Fleet, B.P. Nelson, W.A. Landford and N. Maley, *Phys. Rev. B*, **45** (1992) p. 13367.
- [29] S. M. Ryvkin, "Photoelectric Effects in Semiconductors", Consultants Bureau Publ., NY (1964).
- [30] R. Hulstorn, R. Bird, and C. Riordan, *Solar Cells*, **15** (1985) p. 365.
- [31] M. Vanecek, J. Kocka, J. Stuchlík and A. Tríska, *Solid State Communications*, **39** (1981) p. 1199.
- [32] N. Wyrsh, F. Finger, T.J. McMahon and M. Vanecek, *Journal of Non-Crystalline Solids*, **137&138** (1991) p. 347.
- [33] F. Siebke and H. Stiebig, In *Proceedings of Material Research Society Symposium*, **336** (1994) p. 371.
- [34] A. Rose, "Concepts in photoconductivity and applied problems", R. E. Krieger Publishers (1963).
- [35] A. Luque, ed., *Handbook of Photovoltaic Science and Engineering*, Ed. Wiley, UK, ISBN 0-471-49196-9 (2003).
- [36] C. S. Smith, *Phys. Rev.*, **94** (1954) p. 42.
- [37] A. Taroni, M. Prudenziati and G. Zanarini, *IEEE Transactions on Industrial Electronics and Control Instrumentation*, **17** (1970) p. 415.
- [38] S. M. Allameh, W.O. Soboyejo, T.S. Srivatsan, *Advanced Structural Materials: Properties, Design Optimization and Applications*, (2006) p. 63.
- [39] S. Nishida, M. Konagai, and K. Takahashi, *Jpn. J. Appl. Phys.*, **25** (1986) p. 17.
- [40] P. Alpuim, V. Chu, and J. P. Conde, *IEEE Sensors Journal*, **2**, no. 4 (2002) p. 336.
- [41] P. Alpuim, S.A. Filonovich, C.M. Costa, P.F. Rocha, M.I. Vasilevskiy, S. Lanceros-Mendez, C. Frias, A. Torres Marques, R. Soares and C. Costa, *Journal of Non-Crystalline Solids*, **354** (2008) p. 2585.
- [42] S. Michard, Diploma Thesis, Forschungszentrum Jülich, Germany (2012).
- [43] R. Swanepoel, *J. Phys. E*, **16** (1983) p. 1214.

Chapter 3

3 High-rate deposition of microcrystalline silicon thin films on plastics

High deposition rates of $\mu\text{c-Si:H}$ films on plastic were achieved at low substrate temperature (150°C) by standard Radio-frequency (13.56 MHz) Plasma Enhanced Chemical Vapor Deposition. Focus was on the influence of deposition pressure, inter-electrode distance (1.2 cm) and high power coupled to the plasma, on the hydrogen dilution ratios (HD) necessary to achieve the amorphous-to-nanocrystalline phase transition and on the resulting film deposition rate. For each pressure and rf-power, there is a value of HD for which the films start to exhibit a certain amount of crystalline fraction. For constant rf-power, this value increases with pressure. Within the parameter range studied the deposition rate was highest (0.38 nm/s) for $\mu\text{c-Si:H}$ films deposited at 6 Torr, 700 mW/cm^2 using HD of 98.5 %. Decreasing the pressure to 3 Torr (1.5 Torr) and rf-power to 350 mW/cm^2 using HD = 98.5 % deposition rate is 0.12 nm/s (0.08 nm/s). Raman crystalline fraction of these films is 72, 62 and 53 % for the 6, 3 and 1.5 Torr films, respectively.

3.1 Introduction

Hydrogenated amorphous silicon (a-Si:H) has been widely used in the manufacture of low cost solar cells and panels. The addition of a microcrystalline silicon ($\mu\text{-Si:H}$) bottom cell in high efficiency multi-junction solar cells [1-2] improves conversion efficiency and solar cell stability under illumination. It also brings about the need to increase the absorption layer deposition rate, since a much thicker $\mu\text{-Si:H}$ layer is required to absorb the same amount of light as a-Si:H does. Moreover, $\mu\text{-Si:H}$ films are normally deposited under conditions of very high hydrogen dilution of silane, which dramatically lowers the deposition rate under standard radio-frequency (13.56 MHz) Plasma Enhanced Chemical Vapor Deposition (rf-PECVD) conditions. Therefore, increasing the deposition rate, while keeping up the film electronic quality, is an essential step to enable industrial production at a competitive price of next generation thin-film Si solar cells. High deposition rates have been demonstrated using VHF-PECVD [3]. However, in large-area deposition systems, conventional rf-PECVD is preferred because it facilitates homogeneous deposition over large areas [4] and because it is familiar to the industry. Several groups reported in the literature the key role of using a high pressure deposition regime to achieve high quality solar cells at high deposition rates by rf-PECVD [5-6]. Using a small inter-electrode distance can also slightly increase the deposition rate [7] but, more important for industrial reactors, it avoids the use of large gas volumes and saves pumping power. The main effect of increasing the partial gas pressure is to increase the gas residence time (t_{res}), which is the time the gas molecules spend in the plasma volume before undergoing chemical reactions or being pumped away. The gas residence time needs to be considered in relation to the chemical decomposition time (t_{decomp}). Whereas the gas residence time depends on the chosen deposition conditions and can, within limits, be varied, the decomposition time is given by the specific chemical reactions.

For favorable chemical reactions leading to film growth, the gas residence time should match or even exceed the chemical decomposition time, i.e. $t_{\text{res}} \geq t_{\text{decomp}}$. In this case, t_{res} may be reduced to the limit of t_{decomp} by increasing the gas flow rate. Thereby more molecules, still with sufficient gas residence time, are supplied for decomposition; hence one will also have a higher deposition rate.

In the case of deposition conditions with gas residence times shorter than the decomposition time, i.e. $t_{\text{res}} \leq t_{\text{decomp}}$, an increase of t_{res} to match t_{decomp} may be desirable.

This can be easily achieved by increasing the pressure. As a consequence, the probability of more molecules being decomposed rises, and basically leads to a higher deposition rate. However, higher pressures imply higher collision rates, which may also result in gas phase reactions, and hence in powder formation. Thereby fewer reacted species reach the growing film, and this, in turn, tends to lower the deposition rate. In case of relatively small electrode spacings, the probability of chemical decomposition at the growing film surface, rather than in the plasma volume, may be higher and, thus, the deposition rate will be less adversely affected by powder formation.

Thin-film photovoltaics can only compete in a market dominated by highly efficient c-Si technology if they offer very low price and/or focus on niche markets. One way to achieve both goals is to use flexible, inexpensive plastic substrates which moreover lend themselves to inline high throughput fabrication processes.

This chapter describes the optimization of a-Si:H and $\mu\text{c-Si:H}$ intrinsic and doped layers deposited by rf-PECVD on plastic (PEN) at 150 °C. A small (1.2 cm) inter-electrode distance is used. Focus is placed in the influence of deposition pressure and power coupled to the plasma, on the deposition rate and film electronic quality.

3.2 Experimental details

Hydrogenated amorphous silicon and $\mu\text{c-Si:H}$ thin films are deposited by rf-PECVD on 125 μm thick plastic substrates (PEN, polyethylene naphthalate) using SiH_4 diluted in H_2 . Hydrogen dilution is defined as $\text{HD} = [F_{\text{H}_2}/(F_{\text{SiH}_4} + F_{\text{H}_2})] \times 100\%$, where F 's are gas flow rates, and values between 96 and 99% are used. Substrates are clamped to the top earthed electrode, placed 1.2 cm from the bottom powered electrode, in a parallel plate capacitor configuration, and heated to the deposition temperature $T_{\text{sub}} = 150^\circ\text{C}$. Three HD-series of films are prepared at deposition pressure $p_w = 1.5, 3$ and 6 Torr. In all series rf-power, P_{rf} , is 10 W, corresponding to a power density of 350 mW/cm^2 . The 6 Torr series is repeated using $P_{\text{rf}} = 20$ W (power density = 700 mW/cm^2).

Deposition rate, r_d , is derived from the thickness obtained by analysis of interference fringes in the UV-visible-NIR transmittance spectra and confirmed by profilometry. Film structure is studied by Raman and FTIR spectroscopy. The Raman crystalline fraction, X_c , and crystallite size, d_{nc} , of the films are calculated according to reference [8], as described in section 2.5.1. For the amorphous films, the bond angle deviation $\Delta\theta$

is related to the full width at half maximum (FWHM) Γ of the TO peak centered at 480 cm^{-1} . Room temperature dark conductivity, σ_{dk} , and secondary photoconductivity, σ_{ph} , are measured between coplanar Al contacts 6 mm long with 1 mm gap. Urbach tails and deep defect absorption are obtained from Constant Photocurrent Measurements (CPM).

3.3 Structural properties

Raman spectra of films deposited under HD = 96, 97, 98 and 98.5% at $p_w = 1.5$ Torr [fig. 3.1(a)], 3 Torr [fig. 3.1(b)] and 6 Torr [fig. 3.1(c)] show that for HD = 98% their structure is amorphous at 6 Torr and microcrystalline at 3 and 1.5 Torr, with $X_c = 34\%$ and 56% , respectively. It is concluded that the hydrogen induced amorphous-to-microcrystalline transition (a $\rightarrow\mu$ c) requires a progressively higher HD as the pressure is increased from 1.5 to 3 and 6 Torr. At 6 Torr the a $\rightarrow\mu$ c transition occurs only for HD = 98.5% after increasing rf-power to 20 W [fig.3.1(c)]. Films deposited at 6 Torr and $P_{\text{rf}} = 10$ W (shown only in fig. 3.2) are amorphous up to extreme HD = 99% at which the a $\rightarrow\mu$ c occurs ($X_c \sim 70\%$). This finding can be correlated with results in literature that show, in high H_2 diluted silane plasmas, a progressive shift in concentration of positive ion species from H^+ to SiH_m^+ as pressure increases in the range 0.1-10 Torr [9]. In fact, it has been shown that with the same type of plasma it is only the presence or absence of ions impinging at the growing film surface that determines whether it is amorphous or microcrystalline. It has to be emphasised that a high ionic concentration close to the film surface is not a problem for the film quality but it is the energy of those ions that may pose a problem [10]. In fact, a high ion flux with low kinetic energy obtained at high frequencies gives rise to enhanced surface diffusion of impinging species, even at a low substrate temperature, which is a necessary condition for good crystallinity. It is found that suppression of the ion energy is more effective for improving crystallinity, specially at high growth rates, and it is speculated that hydrogen ions etch the a-Si:H, whereas atomic hydrogen promotes the Si-network [11].

For all pressures and rf-powers studied the a $\rightarrow\mu$ c occurs abruptly, within a 0.5-1% interval in the HD scale. Microcrystalline samples deposited at 6 Torr have lower sized (< 5 nm) Si microcrystals, when compared to the films deposited at 1.5 and 3 Torr (crystallite size ~ 7 nm). This effect is clearly seen in the Raman spectra by the red shift of the crystalline peak.

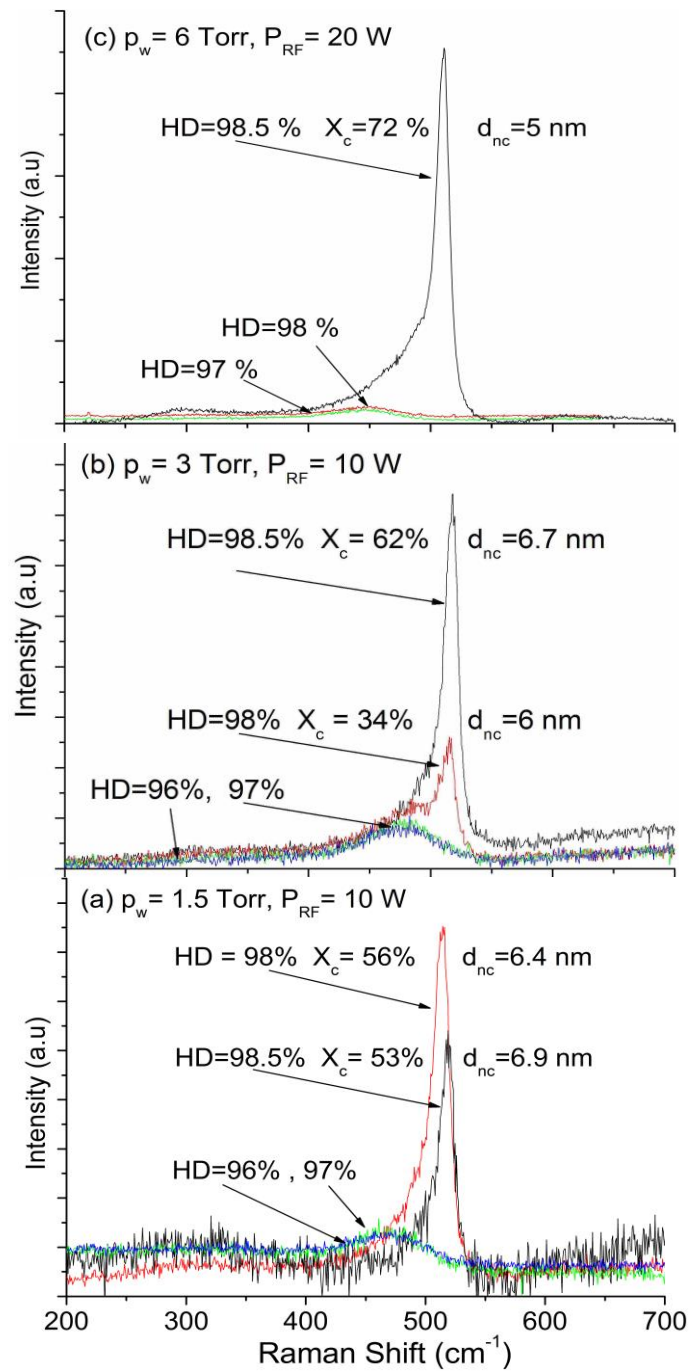


Fig. 3.1: Raman spectra for samples deposited on PEN at (a) $p_w = 1.5$ Torr and $P_{rf} = 10$ W, (b) $p_w = 3$ Torr and $P_{rf} = 10$ W and (c) $p_w = 6$ Torr and $P_{rf} = 20$ W, using different hydrogen dilutions: 96% (blue lines), 97% (green lines), 98% (black lines) and 98.5% (red lines), near the amorphous to microcrystalline transition point. X_c is crystalline fraction and d_{nc} is crystallite size [8].

Figure 3.2 shows the crystalline fraction as a function of HD, where we can see more clearly the occurrence of the a \rightarrow μ c for each series of the studied samples.

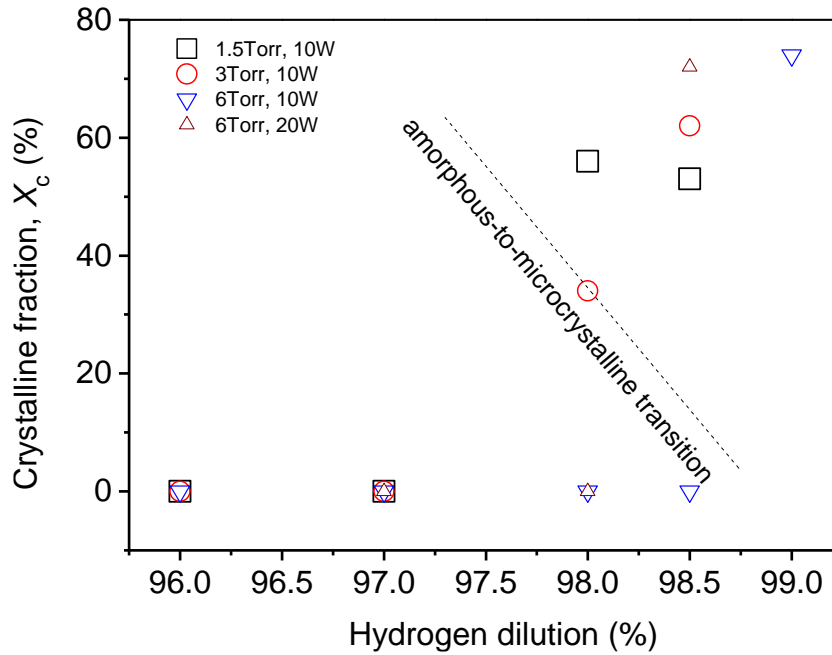


Fig. 3.2: Raman crystalline fraction, X_c , as a function of hydrogen dilution of silane. The dotted line roughly indicates the frontier between deposition conditions yielding amorphous and those yielding microcrystalline Si films on plastic substrates at $T_{\text{sub}} = 150^\circ\text{C}$.

3.4 Deposition rate

Figure 3.3 shows the deposition rate, r_d , as a function of HD for films deposited at 1.5 Torr ($P_{\text{rf}} = 10$ W), 3 Torr ($P_{\text{rf}} = 10$ W) and 6 Torr ($P_{\text{rf}} = 10$ and 20 W) (see also Table 3.1 in section 3.5). Also shown, for comparison, are HD series of films deposited at a larger inter electrode distance (4 cm) using high pressure (1.5 Torr) and high power (10 W) and using low pressure (160 mTorr) and low power (2 W \leftrightarrow 60 mW/cm²). In general, r_d increases with pressure and rf-power, and decreases with inter electrode distance. For example r_d increases from 0.04 to 0.1 nm/s at HD = 98.5%, $P_{\text{rf}} = 10$ W and $p_w = 1.5$ Torr, when the inter electrode gap decreases from 4 to 1.2 cm.

It is known that during the deposition process silylene (SiH_2) and silyl (SiH_3) radicals generated by the chemical reactions between the secondary species in the plasma, mainly determine the film growth rate. Even though silyl radicals will diffuse towards the film surface at both electrode distances, they have however less relative incorporation probability (0.1) into the film for the shorter distance [14]. This is because the survival rate of the much more reactive SiH_2 radicals, having the diffusion length around 0.5 cm and high incorporation probability (0.65-0.8) [13] into the film, is

favoured by the short distance between the electrodes. Possibly the silylene radicals are therefore playing an important role in increasing the deposition rate when the inter electrode gap is reduced.

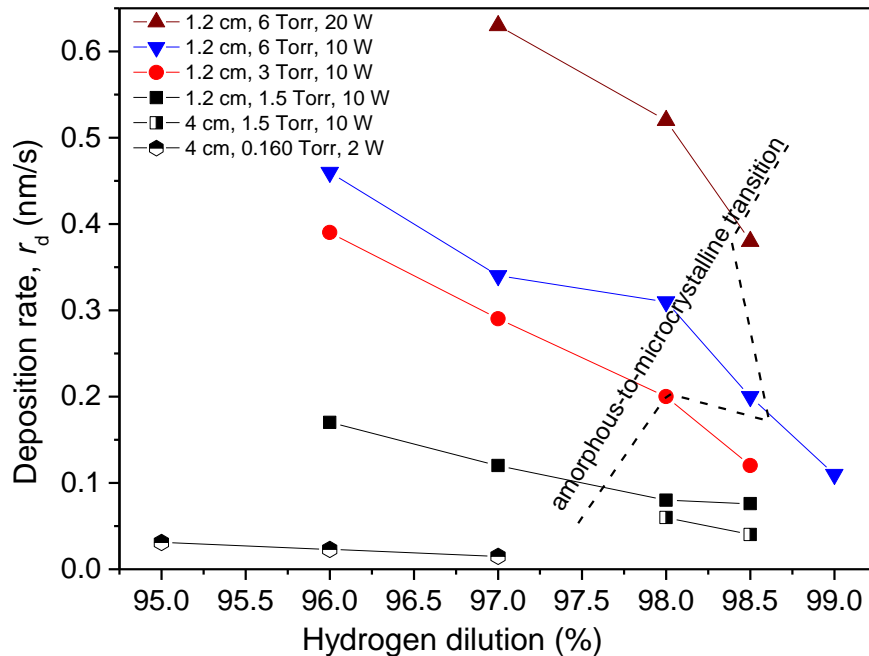


Fig. 3.3: Deposition rate as a function of HD for films deposited on plastic substrates at different pressures (0.160, 1.5, 3, and 6 Torr) and rf-powers (2, 10 and 20 W).

In figure 3.3, data points with abscissa HD = 98.5% correspond, with one exception at 6 Torr (10 W), to microcrystalline films with $X_c > 50\%$. Deposition rate increases approximately 10-fold from bottom to top, i.e. from 0.04 nm/s at 1.5 Torr (10 W) to 0.38 nm/s at 6 Torr (20 W). The transition from an amorphous film at $p_w = 6$ Torr (10 W) to a highly crystalline one ($X_c = 72\%$) at $p_w = 6$ Torr (20 W) might correspond to the threshold of a high-pressure SiH_4 depletion regime, thus inhibiting the H annihilation reaction ($\text{H} + \text{SiH}_4 \rightarrow \text{H}_2 + \text{SiH}_3$) and consequently increasing atomic H concentration, which induces the a \rightarrow μ c transition. It is found in ref. [14] that this high rate deposition regime for μ c-Si:H preserves the high electronic quality of the films.

3.5 Opto-electronic properties

Table 3.1 summarizes important optical and electronic properties of selected samples.

Table 3.1 Deposition conditions, structural and optoelectronic properties of selected intrinsic films deposited on PEN substrates.

Sample	p_w (Torr)	P_{rf} (W)	HD (%)	r_d (Å/s)	σ_d ($\Omega^{-1}\text{cm}^{-1}$)	σ_{ph} ($\Omega^{-1}\text{cm}^{-1}$)	$E_{a,d}$ (eV)	X_C (%)
S844	1.5	10	96	0.17	1.1×10^{-10}	2.1×10^{-4}	0.62	0
S847	3	10	98	0.2	4.2×10^{-10}	2.4×10^{-4}	0.64	34
S857	6	10	98	0.31	4.8×10^{-10}	4.8×10^{-4}	0.57	0
S887	6	20	98	0.52	1.2×10^{-11}	1.2×10^{-5}	0.74	0
S843	1.5	10	98.5	0.07	3.4×10^{-6}	1.0×10^{-4}	0.38	53
S846	3	10	98.5	0.12	4.8×10^{-6}	2.5×10^{-4}	0.42	62
S873	6	10	99	0.10	1.2×10^{-8}	3.9×10^{-5}	0.55	74
S874	6	20	98.5	0.38	3.1×10^{-7}	2.5×10^{-5}	0.47	72

Figure 3.4 shows the photo-to-dark conductivity ratio (photosensitivity, S) as a function of HD. Two groups of films can be identified: those obtained at lower H_2 dilution, with high photosensitivity, and those obtained at higher values of HD, with lower photosensitivity. The maximum value of photosensitivity ($S = 4 \times 10^6$) is obtained for the film deposited at 1.5 Torr, HD = 96% and $P_{rf} = 10$ W. Photosensitivity remains high ($\sim 10^6$) for HD up to 98.5% at 6 Torr (10 W). For deposition pressures of 1.5 and 3 Torr or 6 Torr (20 W) S drops abruptly at HD = 98 and 98.5%, respectively. If one combines the information conveyed in figure 3.4 with the results of the Raman analysis in section 3.3 one concludes that amorphous films are those that exhibit high S -values while a microcrystalline film structure is typical of the low photosensitivity samples, mainly because of their higher dark conductivity. The photosensitivity of films deposited at 6 Torr reaches its maximum value right before the $a \rightarrow \mu c$ transition. The amorphous films with high photosensitivity ($> 10^5$) are good candidates for the fabrication of the top solar cell in tandem or triple junction structures.

Figure 3.5 shows the results from CPM measurements made in a-Si:H films. The results show Urbach tails increasing with deposition pressure from 64 meV at 1.5 Torr to 81 meV at 3 Torr and 85 meV at 6 Torr. These values, particularly for the higher p_w -films, are rather high and one may speculate that they are a consequence of incorporation of dust from the plasma during deposition. Otherwise it is hard to understand how such broad band tails can coexist with the film high photosensitivity shown. Dangling bond concentration, obtained from the CPM spectra, is $\sim 3.5 \times 10^{17} \text{ cm}^{-3}$ in these films. Bond angle disorder, $\Delta\theta$, is 6.79, 6.94 and 6.96 for the films deposited at 1.5, 3 and 6 Torr, respectively.

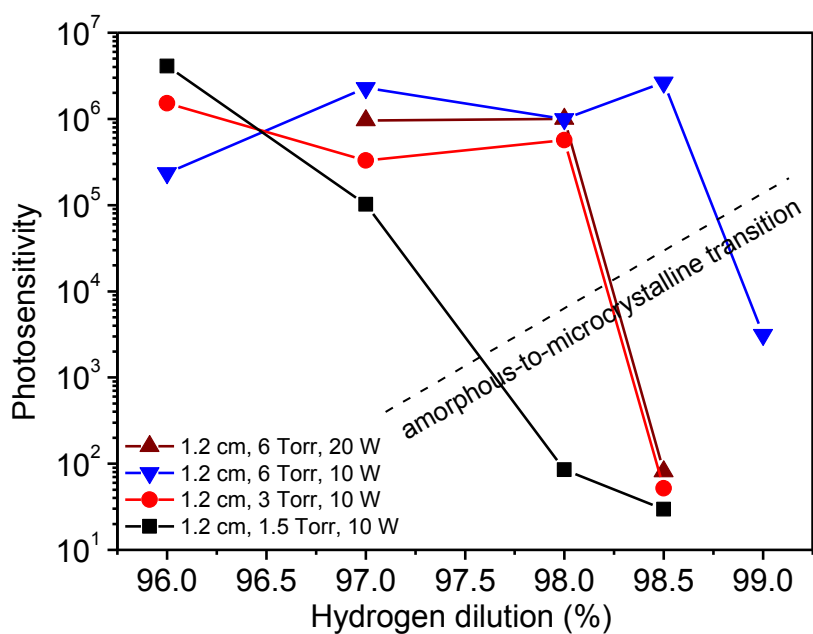


Fig. 3.4: Photosensitivity as a function of HD for films deposited on plastic substrates at different pressures (1.5, 3, and 6Torr) and rf-power (10W and 20W).

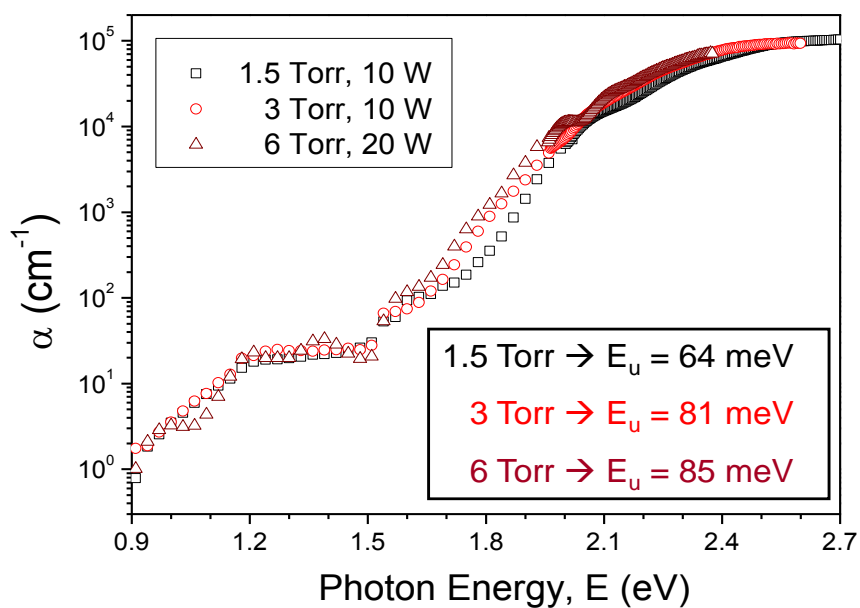


Fig. 3.5: CPM spectra of a-Si:H films deposited at different pressures (1.5, 3, and 6Torr) and rf-power (10W and 20W).

3.6 Doping

Unhydrogenated amorphous silicon films cannot be doped and therefore cannot be used to fabricate devices.

On the other hand, amorphous silicon layers deposited by PECVD from silane contain hydrogen atoms, which passivate a large part of their dangling bonds; such films can be doped by adding phosphine (PH_3) or diborane (B_2H_6) to the silane in order to obtain n- and p-type layers, respectively [15]. What one experimentally finds is, however, that the doping efficiency of phosphorous and boron atoms in hydrogenated amorphous silicon is much lower than in crystalline silicon. As the dopant level increases, the doping efficiency decreases even more. It is not possible by doping to push the Fermi level E_F to meet the band edges E_C and E_V .

This is accounted for in the theory of doping developed by R. Street for amorphous silicon [16] by the concept of compensation. It says that most of the active dopants (which are less than 1% of the P-content in the film, the remaining 99% staying in the 3-fold coordination configuration) are stabilized in the host four-fold configuration by electron transfer to a midgap localized defect states, where they do not contribute to the electrical conductivity. The process of doping itself generates deep defects in amorphous silicon, at a rate of almost one dangling bond (DB) by active dopant atom incorporated. In fact this number is 0.9 DB per 4-fold coordinated P-atom (even less when doping with Boron). As a consequence, for n-type doping, there is a slight excess of electrons relative to DBs and these electrons in excess are the only ones responsible for shifting the Fermi level towards the band edge. From all the electrons occupying band edge states, only a small fraction occupies states above the mobility edge: these are the only carriers that contribute to increase the electrical conductivity.

Despite all this, it is possible to increase the dark conductivity of the films by adding a dopant gas to the silane plasma; however, after reaching a certain doping level this effect stops: it is not possible to reach conductivities much higher than $10^{-2} \Omega^{-1}\text{cm}^{-1}$ for doped a-Si:H films [17]. The doped conductivity of p-type films is normally lower than that of n-type films due to the lower drift mobility of holes in the valence bandtail than of electrons in the conduction bandtail since the first is broader than the latter.

It is found that the doping process in $\mu\text{c-Si:H}$ is a mixture of the phenomena observed in a-Si:H and in c-Si. For low doping levels, of the order of the defect density in the material, i.e. around 10^{16} - 10^{17}cm^{-3} electrons or holes from the dopant atoms first have to fill up these defect states, just as in a-Si:H. For higher doping levels we observe a 1:1 relationship between the built-in doping atoms and carrier density, i.e. we have a substitutional doping process in the crystalline phase of $\mu\text{c-Si:H}$ similar to that in c-Si. In particular, one does not observe any self-compensation effect of the doping process

by thermal equilibrium between four-fold coordinated dopant states and defects. As a result, one can obtain considerably higher conductivities and carrier densities in $\mu\text{c-Si:H}$, as compared with a-Si:H : it is possible to reach conductivities as high as $10^2 \Omega^{-1} \text{cm}^{-1}$ for n- or p-type layers [15].

Phosphine (PH_3) or diborane (B_2H_6) are added to the reactive gas mixture, while keeping up the deposition conditions that yielded the best $\mu\text{c-Si:H}$ (higher X_C) and a-Si:H films (higher S) to obtain n- or p-type films, respectively. Results can be seen in figure 3.6 where σ_{dk} is plotted as a function of hydrogen dilution for films deposited at $p_w = 1.5, 3$ and 6 Torr, with $P_{\text{rf}} = 10$ W (350 mW/cm^2). For n-type films R , defined as the dopant-gas-to-silane flow rate ratio, is kept constant and equal to 2.5. For p-type films R is varied in the interval $[0.5, 2.5]$ ($R = 0.5, 1, 1.5, 2$ and 2.5).

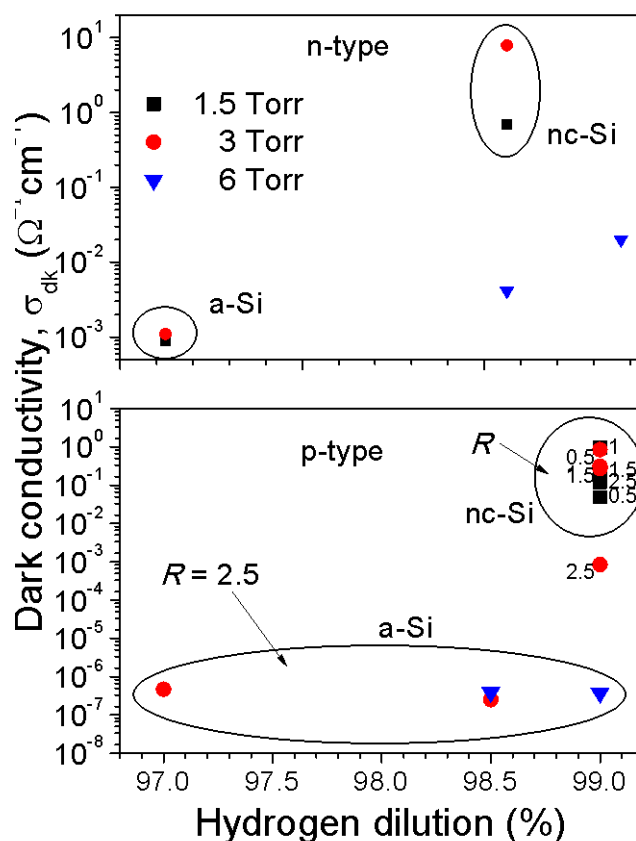


Fig. 3.6: Dark conductivity as a function of hydrogen dilution for p- and n-doped films deposited on PEN at different pressures (1.5, 3, and 6 Torr) and doping ratios (0.5, 1 and 2.5).

Highly conductive $\mu\text{c-Si:H}$ n-type films were obtained at 1.5 and 3 Torr, with conductivities of 0.7 and $8 \Omega^{-1} \text{cm}^{-1}$, respectively. At 6 Torr it was not possible to obtain highly doped films because their structure was strongly amorphized by the dopants [18] and the σ_{dk} was around $10^{-2} \Omega^{-1} \text{cm}^{-1}$ ($E_{\text{a,dk}} = 140 \text{ meV}$). The most strongly doped n-type

a-Si:H films were obtained at 1.5 and 3 Torr, with σ_{dk} around $10^{-3} \Omega^{-1}\text{cm}^{-1}$ ($E_{a,dk} \sim 0.25$ eV).

Highly conductive $\mu\text{c-Si:H}$ p-type films with $\sigma_{dk} \sim 1 \Omega^{-1}\text{cm}^{-1}$ ($E_{a,dk} \sim 30$ meV) were obtained at 1.5 and 3 Torr, using $R = 1$ and 0.5, respectively. At 6 Torr it was not possible to obtain p-type doped microcrystalline films because of the amorphization induced by the dopant atoms. The highest p-type conductivity obtained for a-Si:H films was $\sim 5 \times 10^{-7} \Omega^{-1}\text{cm}^{-1}$ ($E_{a,dk} \sim 0.5$ eV) for $R = 2.5$, obtained at all pressures studied.

3.7 Conclusions

The deposition rate of both a-Si:H and $\mu\text{c-Si:H}$ thin films can be increased consistently by: 1) decreasing the inter electrode distance, 2) increasing the deposition pressure, and 3) increasing the rf-power. The deposition rate decreases as the HD increases in all deposition conditions. For each pressure and rf-power used, there is a value of hydrogen dilution of silane for which the films undergo an amorphous-to-microcrystalline phase transition. The exact concentration of H_2 required for this transition to occur is a function of the deposition parameters and it increases when the working pressure increases, keeping other parameters constant. At 6 Torr it is necessary to increase simultaneously HD and rf-power in order to obtain $\mu\text{c-Si:H}$ films. The films obtained under such conditions are deposited at the highest microcrystalline deposition rate ($r_d = 0.38$ nm/s). The films with high photosensitivity ($>10^5$) are amorphous. The best $\mu\text{c-Si:H}$ have photosensitivity around 10^2 . The best mixed phase film is obtained at 6 Torr, 20 W and has photosensitivity in excess of 10^3 . n- and p-type $\mu\text{c-Si:H}$ films are obtained with $\sigma_{dk} = 7.8$ and $0.87 \Omega^{-1}\text{cm}^{-1}$, respectively. At 6 Torr, it is not possible to obtain highly doped microcrystalline films. n-type conductivity is $10^{-3} \Omega^{-1}\text{cm}^{-1}$ while p-type $\sigma_{dk} = 5 \times 10^{-7} \Omega^{-1}\text{cm}^{-1}$.

References

- [1] V. Shah, J. Meier, E. Vallat-Sauvain, N. Wyrsh, U. Kroll, C. Droz and U. Graf, *Sol. Energy Mater. Sol. Cells*, **78** (2003) p. 469.
- [2] S. Guha and J. Yang, *J. Non-Cryst. Solids*, **352** (2006) p. 1917.
- [3] O. Vetterl, F. Finger, R. Carius, P. Hapke, L. Houben, O. Kluth, A. Lambertz, A. Mück, B. Rech and H. Wagner, *Sol. Energy Mater. Sol. Cells*, **62** (2000) p. 97.
- [4] U. Kroll, D. Fischer, J. Meier, L. Sansonnens, A. Howling and A. Shah, *Mater. Res. Soc. Symp. Proc.* **557** (1999) p. 121.
- [5] L. Guo, M. Kondo, M. Fukawa, K. Saitoh and A. Matsuda, *Jpn. J. Appl. Phys.* **37** (1998) p. L1116.
- [6] B. Rech, T. Roschek, T. Repmann, J. Müller, R. Schmitz and W. Appenzeller, *Thin Solid Films*, **427** (2003) p. 157.
- [7] Y. Fukuda, Y. Sakuma, C.H. Fukai, Y. Fujimura, K. Azuma and H. Shirai, *Thin Solid Films*, **386** (2001) p. 256.
- [8] T. Kaneko, M. Wakagi, K. Onisawa, and T. Minemura, *Appl. Phys. Lett.*, **64** (1994) p. 1865.
- [9] S. Nunomura and M. Kondo, *Appl. Phys. Lett.* **93** (2008) p. 231502.
- [10] J. Perrin, M. Shiratani, P. Kae-Nune, H. Videlot, J. Jolly and J. Guillon, *J. Vac. Sci. Technol. A*, **16** (1998) p. 278.
- [11] H. Keppner, U. Kroll, P. Torres, J. Meier, D. Fischer, M. Goetz, T. Tschärner, A. Shah, *In Proceedings of 25th IEEE Photovoltaic Specialist Conference*, **669** (1996).
- [12] J. K. Rath, *Solar Energy Materials and Solar Cells*, **76** (2003) p. 431.
- [13] M. Hertl and J. Jolly, *J. Phys. D: Appl. Phys.* **33** (2000) p. 381.
- [14] M. Kondo, M. Fukawa, L. Guo and A. Matsuda, *J. Non-Cryst. Solids*, **266** (2000) p. 84.
- [15] A. Shah, ed., *Thin-film Silicon Solar Cells*, First edition, EPFL Press (2010).
- [16] M. Stutzmann, D. K. Biegelsen, R. A. Street, *Phys. Rev.* **B35** (1987) p. 5666.
- [17] W.E. Spear, P.G. LeComber, *Sol. State Comm.* **17** (1975) p. 1193.
- [18] P. Alpuim, M. Andrade, V. Sencadas, M. Ribeiro, S.A. Filonovich, S. Lanceros-Mendez, *Thin Solid Films*, **515** (2007) p. 7658.

Chapter 4

4 Amorphous silicon solar cells on flexible substrates

In order to improve the transparent contact layer in amorphous silicon solar cells fabricated on low-temperature plastic substrates, Al and Ga doped ZnO films were deposited at room temperature on plastic and glass and their optical, electronic and structural properties were correlated and optimized. Selected deposition conditions resulting from the study described in the previous chapter were used to fabricate amorphous silicon solar cells at a substrate temperature of 150 °C on PEN/TCO, in the superstrate p-i-n configuration. The efficiency is around 5%, limited by low current density and low fill factor. Amorphous silicon solar cells with efficiencies around 6.5% were also fabricated in the substrate n-i-p configuration on PI foils at a substrate temperature of 200 °C. Aiming to explore light trapping effects, plastic substrates were laser textured and their haze, total transmittance and reflectance were compared with those of untextured substrates. Although the haze increased dramatically, from 1.7 to 78.9%, the total transmittance of PET coated with ZnO:Ga decreased from 83.9%, in the untextured substrate, to 58.5% in the textured PET. The haze in reflected light of PET coated with Al increased from 4.3% to 66.2% after texturing but the total reflectance decreased from 70.1% to 36.8%. Therefore these substrates were not used for solar cell fabrication.

4.1 Introduction

Single junction amorphous silicon solar cells were fabricated on flexible plastic substrates in p-i-n configuration on PEN at 150 °C, and in n-i-p configuration on PI at 200 °C.

Another issue for fabrication on plastics is the deposition of the transparent and conductive oxide (TCO) used as contact window layer in a-Si:H solar cells. These layers are typically made on glass, at high temperature (> 150 °C) that is not compatible with plastic substrates. In this study, doped zinc oxide is deposited at room temperature directly on plastic. Aluminium and gallium are used as dopants and their effect on the structural, optical and electronic properties of the TCO are studied.

In order to increase the relatively low efficiency of a-Si:H solar cells it is crucial to develop light-trapping schemes that largely increase the optical path length inside the absorbing layer [1]. Excimer laser texturization of plastic substrates was carried out and the resulting optical characteristics of the substrates were characterized.

4.2 Experimental details

ZnO:Ga (GZO) and ZnO:Al (AZO) thin films are deposited at room temperature in vacuum under an Ar atmosphere with a base pressure of 2×10^{-6} Torr by DC magnetron sputtering keeping a target-to-substrate distance constant at 8 cm in all runs. For GZO deposition a 2-inch ZnO:Ga target, (zinc oxide/gallium, 95.5/4.5 wt.%), a working pressure of 4 mTorr and a target current density of 4.9 mA cm^{-2} have been used and a deposition rate of 0.47 nm/s is obtained. For AZO deposition a 4-inch ZnO:Al target, (zinc oxide/aluminium, 98.0/2.0 wt.%), a working pressure of 3 mTorr and a target current density of 2.5 mA cm^{-2} have been used and a deposition rate of 0.48 nm/s is obtained.

The texturing of plastic substrates, consisting of ablation at laser irradiation above the material damage threshold, is performed on polyester films (polyethylene terephthalate, PET) with thickness of 125 μm . Substrates are cleaned in ethanol in an ultrasonic bath for 10 min followed by 10 min in water. The light source is ArF Excimer Laser (193 nm). Fluence is controlled by an attenuator (Lasoptics) followed by imaging using a fly's eye homogenizer (EX-HS-700D) with 650 mm spherical focusing lens.

The sample is positioned on a holder with single axis servo motor at the focus of the homogenizer allowing movement in direction perpendicular to the incident beam. Laser repetition rate is always 1 Hz, fluence is varied as follows: 50, 60 and 70 mJ/cm², with the corresponding velocity 0.5, 0.5 and 1 mm/s.

Optical properties of the textured plastics substrates are measured in a dual beam Shimadzu spectrophotometer set-up in transmission and reflection modes. In specular transmittance, reference sample (non-treated PET) and the studied sample (laser treated PET) are put into two different substrate holders. The light beam of wavelengths ranging from 250-900 nm is split in two beams that simultaneously passed through each sample. The difference between the reference beam and the beam coming from the sample is recorded in the form of a spectrum. Diffuse transmittance measurements are performed using an integrating sphere. Integrating spheres are shells coated with a highly reflective material such as barium sulfate. The sphere has entrance and exit apertures for incident and emergent light, respectively. Detectors are positioned directly under or over an aperture in the bottom or top of the sphere, respectively.

Single junction p-i-n superstrate solar cells are fabricated at 150 °C by rf-PECVD (deposition system described in section 2.3.1) on 125 µm-thick PEN substrate covered with GZO. Table 4.1 shows the deposition parameters of the p-i-n junction. To complete the solar cell on plastic, thermally evaporated Al contacts are used, also acting as back reflectors. The substrate area is 3×3 cm² or 1.5×3.0 cm² and the area of the solar cells, defined by using a shadow mask during Al back contact deposition, is 0.126 cm² or 0.0314 cm². Selected solar cells are annealed at 150 °C in vacuum for 30 minutes to one hour.

Table 4.1: Deposition conditions for Si layers used in the solar cells fabrication.

Layer	T_{sub} (°C)	H ₂ dilution (%)	P_{RF} (mW/cm ²)	p_w (Torr)	$F_{\text{PH}_3}/F_{\text{SiH}_4}$ (%)	$F_{\text{B}_2\text{H}_6}/F_{\text{SiH}_4}$ (%)
intrinsic	150	96	350	1.5		
buffer a-Si:H	100	97	175	0.15		
n-type	150	96	350	1.5	2.5	
p-type	150	98.5	175	1.5		2.5

Amorphous silicon n-i-p substrate solar cells are fabricated on 125 µm-thick polyimide foils. The solar cells are prepared on 10×10 cm² foils. The substrate holder used for the fabrication procedure is a 10×10 cm² stainless steel sandwich mask

consisting of a back plate and a frame with 6 apertures of $4 \times 2.3 \text{ cm}^2$ each, as shown in fig. 4.1.

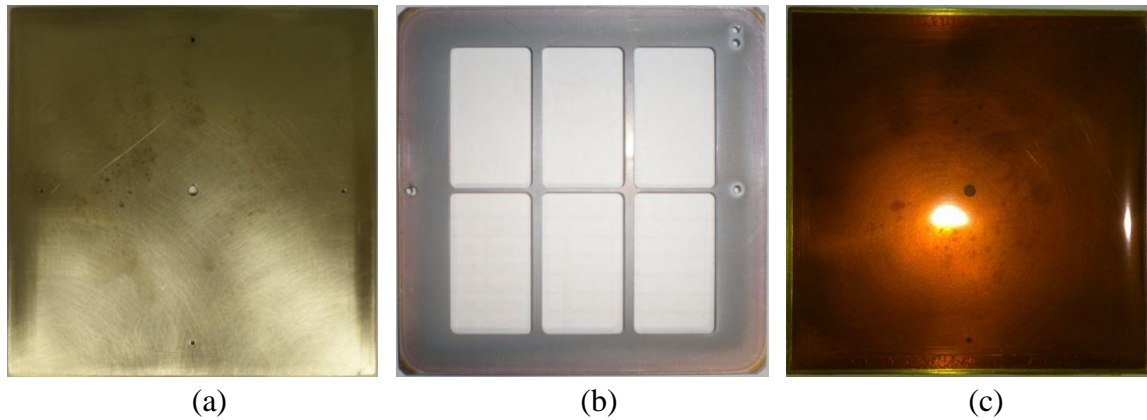


Fig. 4.1: Sandwich mask used to hold the polyimide substrate during depositions. **a)** back plate, **b)** frame and **c)** PI foil fixed on the back plate.

The substrates are covered with a thermally evaporated 700 nm Ag layer and an 80 nm sputtered ZnO:Ga, both deposited at room temperature. The thin film silicon layers are deposited in n-i-p sequence by standard rf-PECVD (13.56 MHz) using the cluster tool deposition system described in section 2.3.2. The substrate temperature is 200°C for intrinsic and doped layers. The power density and working pressure for deposition of intrinsic and doped layers are 42 mW/cm^2 and 1.2 Torr, respectively. The front transparent contacts made of 70 nm thick AZO layers are prepared by radio-frequency (RF) magnetron sputtering at 150°C using a ZnO:Al target (98/2 wt.%) in an argon atmosphere. The individual solar cells with an area of $1 \times 1 \text{ cm}^2$ are defined by using a shadow mask during AZO deposition on the $10 \times 10 \text{ cm}^2$ substrate. Front metal finger electrodes are prepared by silver evaporation. Finally, standard annealing procedure of finished solar cells is performed in air at 160°C for 30 minutes. The complete device layer sequence is: PI/Ag/GZO/n-i-p/AZO. For comparison solar cells are also deposited on glass substrates with corresponding layer sequences.

4.3 Doped ZnO films

Figure 4.2 shows the Raman spectra of ZnO films with thicknesses of $\sim 700 \text{ nm}$ doped with Al (top) and with Ga (bottom). The optical transmittance was higher than 80% in both films. The Raman characteristic 437 cm^{-1} peak of ZnO wurtzite structure, assigned to the non-polar optical phonon mode ($E_2\text{-high}$) is present in both spectra.

Likewise, a broad band in the spectral region close to the LO phonon frequencies of undoped c-ZnO (574 cm^{-1} for A_1 -mode and 583 cm^{-1} for E_1 -mode [2]) is well defined, though its profile and maximum peak position changes with the dopant atom. These modes are ascribed to defects of oxygen vacancies and interstitial Zn and free carriers [3].

It is known that most undoped ZnO material is strongly n -type. It has long been assumed that the dominant donor is a native defect, either the O vacancy V_O , or the Zn interstitial Zn_i [4]. Since the A_1 –LO-Raman mode of ZnO is related to the formation of the oxygen deficiency, interstitial zinc and free carrier density [5], the low resistivity of the GZO and AZO thin films obtained ($8.8\times 10^{-4}\ \Omega\text{ cm}$ and $2.6\times 10^{-3}\ \Omega\text{ cm}$, respectively) is ascribed to the high concentration of V_O , or/and Zn_i . It may be interesting to note that in spite of the low crystalline fraction of the ZnO:Ga sample deposited at RT (due to the small amplitude of the E_2 high mode) an extra mode at 510 cm^{-1} is present. This extra peak has no clear assignment. In ref. [6] the appearance of three new Raman modes at 512 , 594 , and 639 cm^{-1} in the Ga doped samples is observed and is consistent with previous experimental results on GZO thin films [2]. In figure 4.2, the presence of this mode in the ZnO:Ga spectrum and its absence from the ZnO:Al spectrum, support the hypothesis that it is due to the differences in mass and ionic radii between Ga and the host Zn atoms.

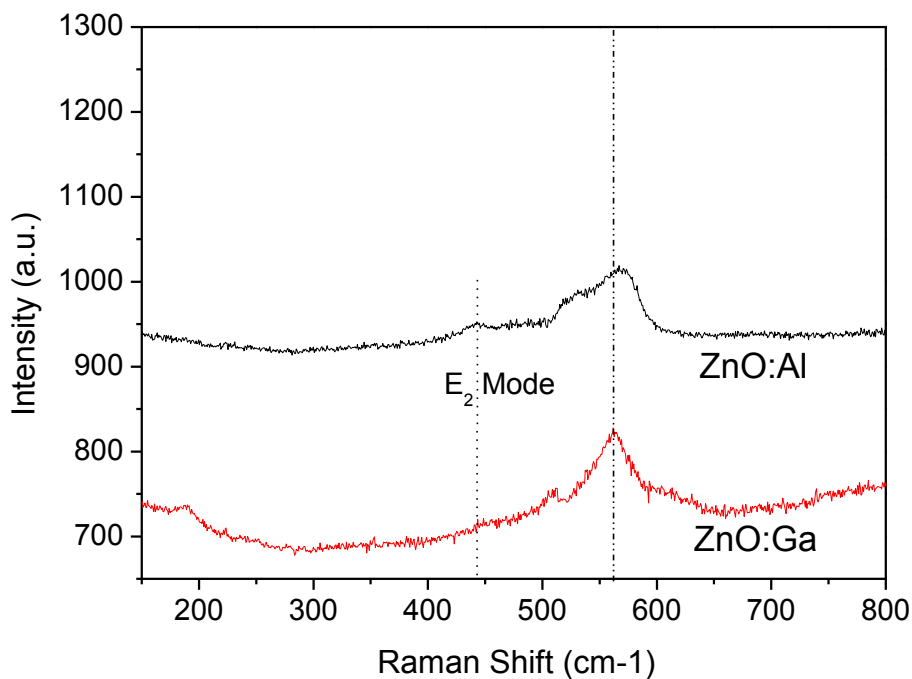


Fig 4.2: Raman spectra of $\sim 700\text{ nm}$ thick Ga (bottom) and Al (top) doped ZnO films.

4.4 p-i-n superstrate solar cells on PEN

As-deposited p-i-n solar cells showed conversion efficiency (η) between 1-3% under AM 1.5 conditions. Upon annealing at 150°C for 30 minutes to 1 hour in vacuum, conversion efficiency improved. Figure 4.3 shows the I-V curves of two p-i-n diode amorphous silicon solar cells deposited on PEN/GZO. The two curves correspond to solar cells differing in two respects. Firstly, their absorbing layers are different – SC88 has a 400 nm thick i-layer deposited by rf-PECVD (HD = 96%) and SC91 has a 350 nm thick i-layer deposited by HWCVD (HD = 50%). Secondly, their p-layers, both deposited by rf-PECVD, have different optical bandgaps – 1.89 eV for SC88 and 1.76 eV for SC91. Both cells have a 9 nm buffer layer inserted between the p and i-layers in order to prevent electron back diffusion into the p-layer and to protect the p-layer from atomic hydrogen attack during the i-layer deposition. This is crucial when depositing the i-layer by HWCVD, since the high concentration of atomic hydrogen produced by decomposition of SiH₄ and H₂ at the filament readily attacks the boron-doped layer and will destroy it in the absence of the protective buffer layer.

The parameters derived from the I-V plot are given in table 4.2. The HWCVD cell has a higher short-circuit current ($J_{sc} = -12.7 \text{ mA/cm}^2$), probably due to the thinner i-layer, which favors a fully depleted i-layer and an enhanced built-in electric field resulting in a higher carrier collection efficiency (see section 1.1.2). The rf-PECVD cell has higher V_{oc} (= 0.830 V), because the i-layer has the highest photosensitivity (see fig. 3.4) and the p-layer has the highest E_{opt} of the two. Solar cell SC88 has a higher shunt resistance under AM1.5 illumination (see table 4.2) which, together with its higher V_{oc} give a slightly better fill factor (FF = 54.2%) when compared to SC91 (FF = 51.0%).

In order to assess where the main conversion losses occur, external quantum efficiency (EQE) measurements are performed under: i) no bias; ii) a small reverse bias (-1V); and iii) a forward bias corresponding to the maximum operating power point (0.5-0.6V). Figure 4.4 shows the results for the solar cell SC91, with i-layer by HW. The EQE results for SC88 (i-layer by rf-PECVD) are not displayed here but they are essentially identical to those shown in fig. 4.4. Therefore, the discussion and main conclusions that will follow can also be applied *grosso modo* to solar cell SC88 as well. The EQE of a calibrated solar cell (R-SC) deposited on ITO/Glass substrate at 250 °C is also plotted as a reference.

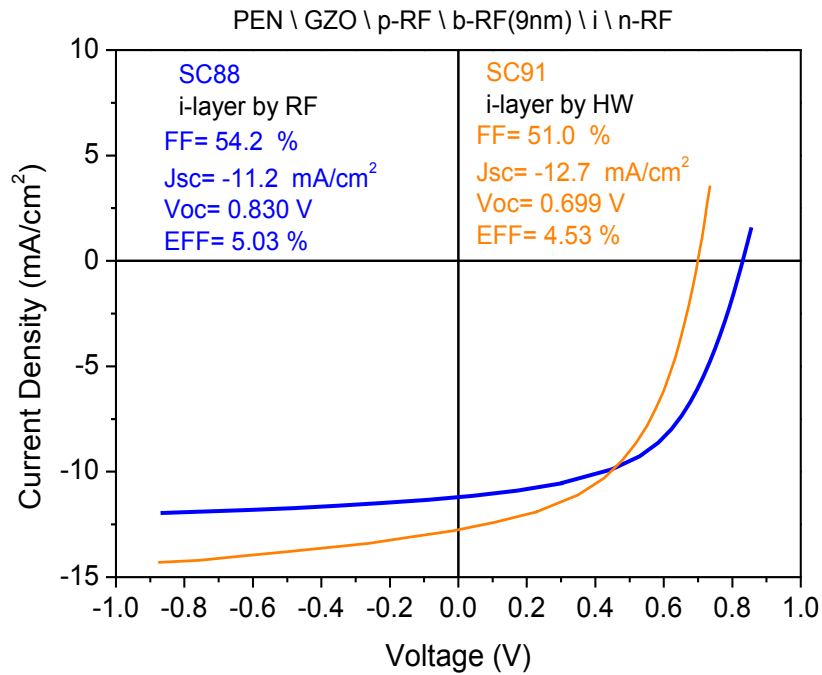


Fig. 4.3: AM1.5 I-V curves of p-i-n solar cells deposited on plastic (PEN).

Figure 4.4 shows that the maximal values of EQE (0.7) fall short of the value of 0.8 charge carriers collected per incident photon, which is typical of good a-Si:H solar cells. It is apparent that one main difference between the R-SC and the flexible solar cell is the response in the long wavelength part of the spectrum, which could be explained by a reduced hole mobility and a non-regulated light trapping mechanism in the flexible solar cells.

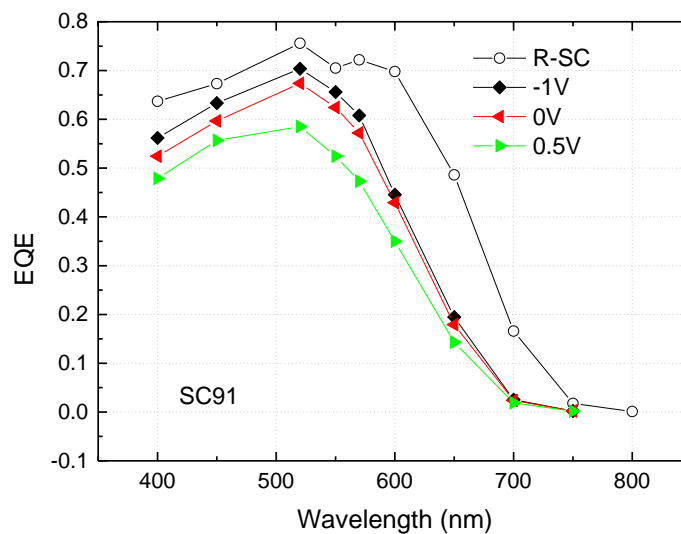


Fig. 4.4: External quantum efficiency (EQE) of SC91 (i-layer by HW) for three different bias levels: i) -1V; ii) 0V (no bias); and iii) 0.5V. The EQE of a reference, high-temperature a-Si:H solar cell deposited on glass is also shown (open marks) for comparison.

The relatively high EQE of the R-SC at short λ end of the spectrum suggests that the bandgap of p-layer in flexible solar cells has to be increased for the window layer to become more transparent in the UV and for better charge collection efficiency.

Table 4.2: Summary of electrical characteristics of selected flexible solar cells.

Cell	V_{oc} (V)	J_{sc} (mA/cm ²)	FF (%)	R_{sh} (Ω)	R_s (Ω)	η (%)
SC91	0.699	12.7	51.0	582	11	4.53
SC88	0.830	11.2	54.2	1145	17	5.03

4.5 n-i-p substrate solar cells on PI

Flexible thin film silicon solar cells are usually fabricated in the n-i-p deposition sequence in substrate configuration because it allows the use of opaque, light weight substrates, such as plastic sheets or metallic foils [7,8], and because in the substrate configuration the plastic is not exposed to the UV radiation coming from the Sun, which degrades most common polymers. The use of such substrates is of interest in thin film silicon solar cell technology because it reduces manufacturing cost by enabling roll-to-roll production [9]. Besides it opens new possibilities for applications, like better integration into buildings and textiles. The most used substrate materials for the fabrication of flexible thin film silicon-based solar cells include stainless steel substrates [10,11], polyimide (PI) [12], polyethylene terephthalate (PET) and polyethylene naphthalate (PEN) [13,14]. Among the organic polymer substrates, PI has the advantage of a higher melting point and glass transition temperature, with a smaller thermal shrinkage [15].

Figure 4.5 shows the I-V parameters of n-i-p substrate solar cells fabricated on glass and polyimide foil with different thicknesses for the p-layer.

The solar cells fabrication procedure is described in section 4.2. The device structure and deposition parameters of all layers are the same for the cells on both substrates. Only the p-layer thickness is varied from 10 to 40 nm.

The best efficiencies in the flexible solar cells were around 6 – 6.5% for p-layer thicknesses of 20 and 25 nm. The V_{oc} is around 20-30 mV lower for the flexible solar cells in comparison with the cells on glass, and for p-layers below 20 nm, V_{oc} drops down abruptly for both substrates. Current-density (J_{SC}) decreases consistently with p-layer thickness due probably to increased absorption losses in the p-layer. The series

resistance is high all over the range for both substrates, suggesting that the contact layers may have poor quality and/or the *i*-layer is too thick (~400 nm).

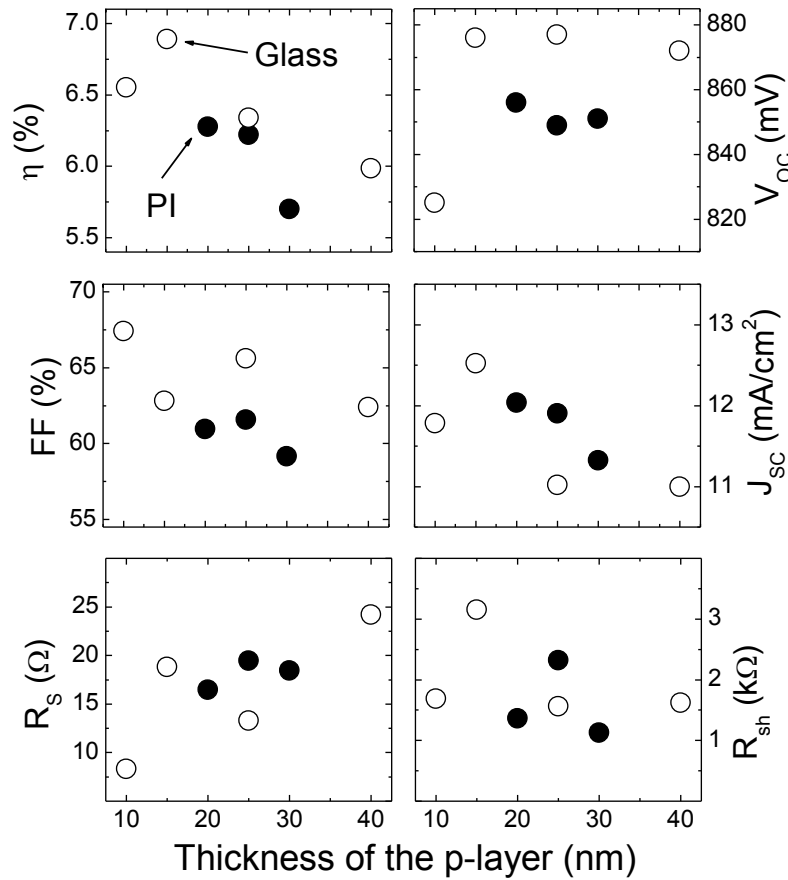


Fig. 4.5: I-V parameters of solar cells with different p-layer thicknesses deposited on PI/Ag/ZnO (full symbols) and glass/Ag/ZnO (open symbols).

Comparing the obtained solar cells parameters for both substrates, we see that the main difference is related to V_{oc} and FF , which is intrinsically linked to V_{oc} . There are, therefore, some basic limitation on the V_{oc} values of amorphous solar cells, i.e.: the relatively high reverse saturation current prevailing in actual amorphous silicon solar cells, because of recombination/generation within the *i*-layer; the difficulty in displacing the Fermi-level by doping in amorphous silicon layers, because of the presence of bandtails. In spite of these reasons, the relatively low V_{oc} values obtained in amorphous silicon solar cells (despite a band gap higher than 1.7 eV) are not fully understood. They do constitute, however, a major limitation for applications [16]. Also, the effect of the PI substrate on V_{oc} limitation would need more attention in this case.

4.6 Laser texturing of PET substrates

The p-i-n amorphous Si thin film solar cell has a number of interfaces. The presence of interface electronic states, particularly in the p/i interface causes open-circuit voltage limitation [17]. In fact, using a buffer layer to passivate these interface states may help increase V_{oc} [18]. Since we intend to use textured substrates in order to enhance the optical absorption, the topography of all layers will be affected by the appearance of surface roughness, which can be more or less severe depending on the deposition conditions [19]. The goal is to obtain optical scattering for different wavelengths of light for the improvement of the photoresponse of the device. Looking at actual V_{oc} values obtained during the last two decades for amorphous silicon solar cells, one notes that there remains in principle still a lot to be gained for V_{oc} , as discussed in section 4.5. So far, however, in spite of many attempts, no V_{oc} values higher than about 1V were obtained for a-Si:H cells, and most practically usable cells have V_{oc} values which are just around 0.85-0.9 V. The FF value, on the other hand is linked to V_{oc} , and is also reduced in cells characterized by large numbers of interface states and dangling bonds which lead to an increase in recombination losses. One therefore cannot expect to increase the FF value if one increases the roughness of the interfaces. However J_{sc} can be increased due to the enhanced optical path length resulting from scattering in the rough interfaces. This effect can actually overcome the lost due to the lowering of the FF with an overall result of improving the conversion efficiency of the a-Si:H solar cell.

From the main parameters defining solar cell performance the largest margin for further improvement lies clearly, for all types of thin film silicon solar cells, in J_{sc} . If one wants, however, to keep cell thickness reasonably low, this can only be done by optical means, i.e. by light trapping. This is a complex optical problem: it requires suitably textured layers and very low optical absorption in all transparent layers.

In order to investigate how textures realized on plastic substrates affect the cell efficiency, two types of samples are prepared: for use in substrate configuration (n-i-p) solar cells, laser textured PET substrates are covered by an Al reflecting contact deposited by thermal evaporation; and for application in superstrate configuration (p-i-n) solar cells, textured PET substrate is coated with a transparent front contact (ZnO:Ga) by sputtering. These samples are characterized by reflectance and transmittance measurements as described in section 4.2.

Figures 4.6 and 4.7 show the transmittance of light, in the optical wavelengths, of 125 μm thick PET substrates covered with ~ 700 nm of ZnO:Ga. Some substrates were laser treated, previously to ZnO deposition, using different irradiation conditions, summarized in table 4.3. Figure 4.6 shows the transmittance of scattered light whereas figure 4.7 shows the total transmittance, i.e., the sum of the scattered light and the specular light transmittances.

The maximal scattered transmittance of laser irradiated substrates is found at around 550 nm (fig. 4.6), which closely matches the maximum irradiance of the solar spectrum. However, the total transmittance data (fig. 4.7) reveals that the laser treated substrates are less transparent than untreated ones. This fact might be caused by carbonized not transparent material that stays on the surface of the substrate upon laser texturing and/or because of increased absorption in the ZnO:Ga due to internal reflection induced by the texture.

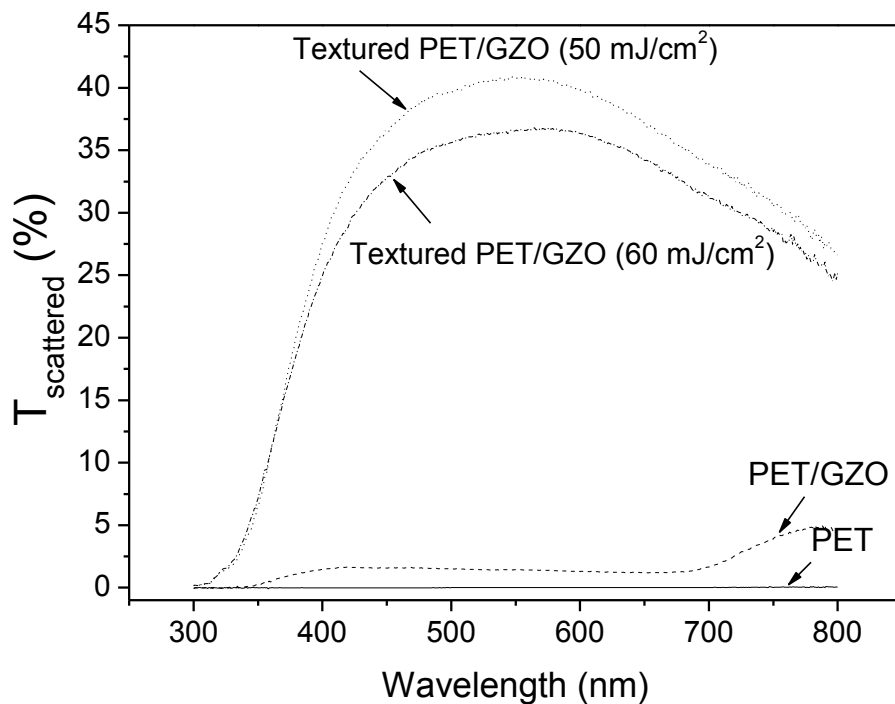


Fig. 4.6: Transmittance of scattered light by 125 μm thick PET substrates covered with ~ 700 nm of ZnO:Ga. Two of the substrates are laser textured using fluences of 50 and 60 mJ/cm^2 before GZO deposition. The transmittance of a bare PET substrate is given for comparison.

The transmittance data for scattered light of flat, uncoated PET and of PET coated with GZO without laser treatment is included in fig. 4.6, for comparison. Bare PET has a transmittance of scattered light that is close to zero. When PET is covered with GZO, which increases its surface roughness, the scattered transmittance increases to $\sim 2\%$ in the range up to 700 nm and to close to 5% in the range 750-800 nm. The total

transmittance (scattered + specular) of the untreated PET/GZO substrates shown in fig. 4.7 is very high, close to that of uncoated PET, except for the displacement to slightly higher wavelengths of the absorption edge in the GZO coated substrates.

Table 4.3: PET substrate roughness after laser irradiation.

Energy (mJ/cm ²)	Velocity (mm/s)	RMS roughness, R_a (nm)	
		uncoated	Al-coated*
60	0.5	26.1	111.2
50	0.5	53.5	102.5

* 180 nm thick.

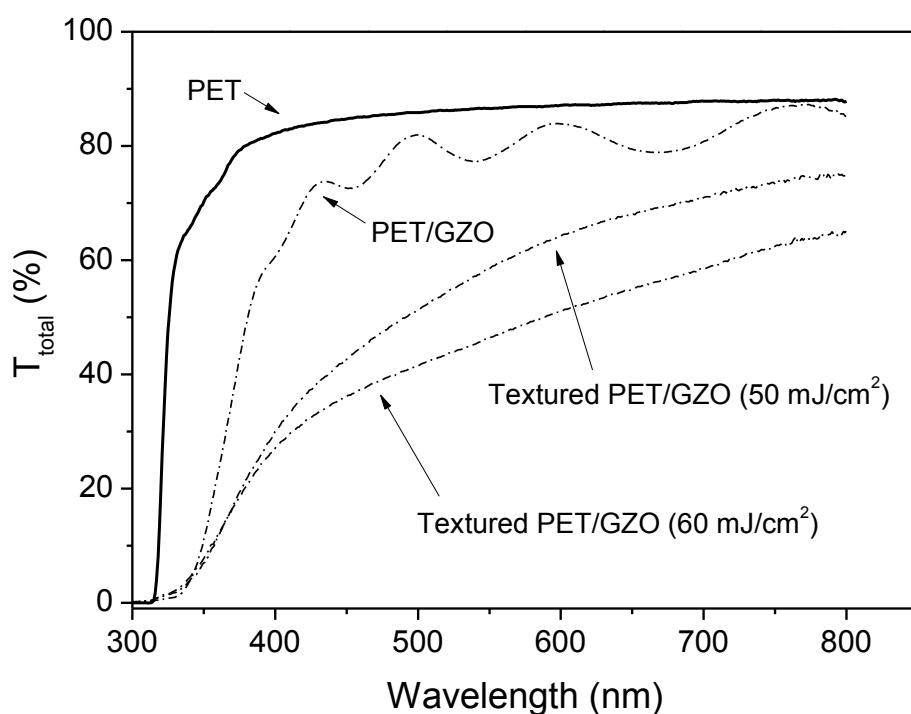


Fig. 4.7: Total transmittance for the same group of samples shown in fig. 4.6

Figures 4.8 and 4.9 show the scattered and specular reflectance, respectively, of Al-coated PET substrates. It can be seen that the scattered reflectance of Al-coated PET substrates increases from ~3% in untreated substrates, to 30% at 550 nm on laser textured PET substrates, using a fluence of 60 mJ/cm².

However, the total reflectance (scattered + specular) decreased from 70% to ~30% as a consequence of the laser treatment of the plastic substrates (see fig. 4.9).

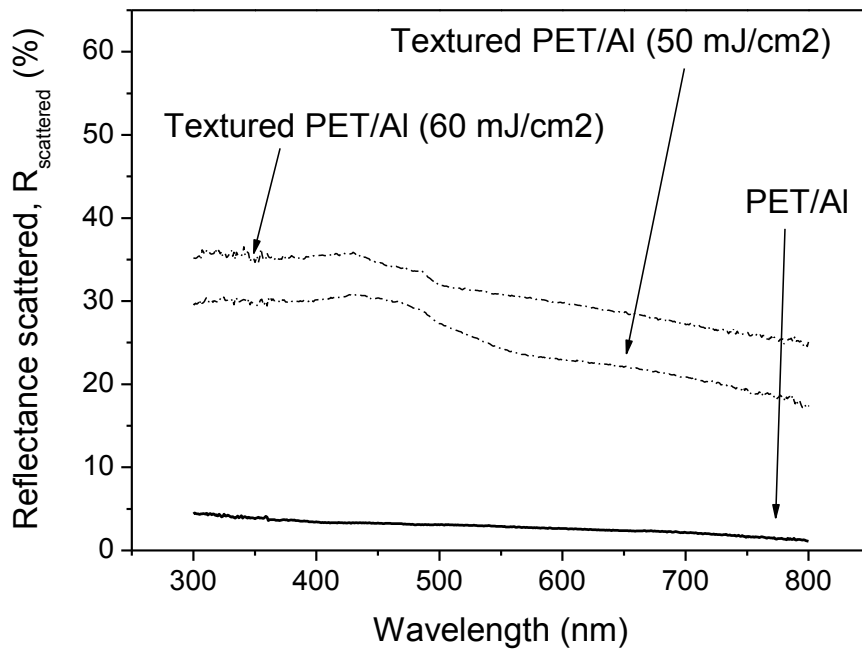


Fig. 4.8: Reflectance of scattered light by 125 μm thick Al-coated PET substrates. Two of the substrates are laser textured using fluences of 50 and 60 mJ/cm^2 before Al deposition. The reflectance of an untreated Al-coated PET substrate is given for comparison.

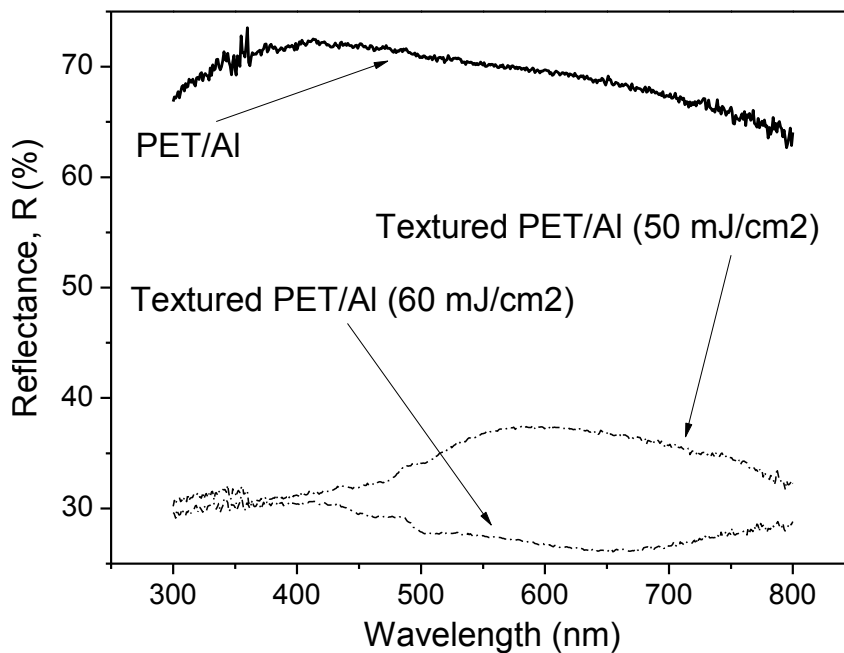


Fig. 4.9: Total reflectance for the same group of samples shown in fig. 4.8.

In order to assess the effect of the roughness induced by the laser treatment on the absorption of the solar cell active layer in superstrate configuration, laser irradiated PET substrates coated with 700 nm ZnO:Ga were covered with a 250 nm thick a-Si:H layer deposited by PECVD using the same deposition conditions for all samples: $T_{\text{sub}} = 130$

$^{\circ}\text{C}$, $P = 8 \text{ W}$, $p_w = 400 \text{ mTorr}$, $F_{\text{SiH}_4} = 40 \text{ sccm}$; and characterized by transmittance measurements in the range of wavelengths from 300-1600 nm.

Figure 4.10 shows the scattered transmittance of the samples treated with 50 mJ/cm^2 and 60 mJ/cm^2 , after deposition of the amorphous silicon layer. In order to study the influence of the ZnO:Ga layer in the scattering process, a sample irradiated with 50 mJ/cm^2 , also covered with a-Si:H and without ZnO is included for comparison. Figure 4.11 shows the total transmittance for the same samples shown in fig. 4.10 and a non-irradiated sample as reference. All spectra of samples containing a-Si:H films exhibit modulation in the spectral transmittance due to interference fringes that form from multiple reflections at the film interfaces, as discussed in section 2.4. Figure 4.10 reveals that the sample irradiated with 50 mJ/cm^2 promotes more scattering at most wavelengths, including in the infrared part of the spectrum, when compared to the one irradiated with 60 mJ/cm^2 .

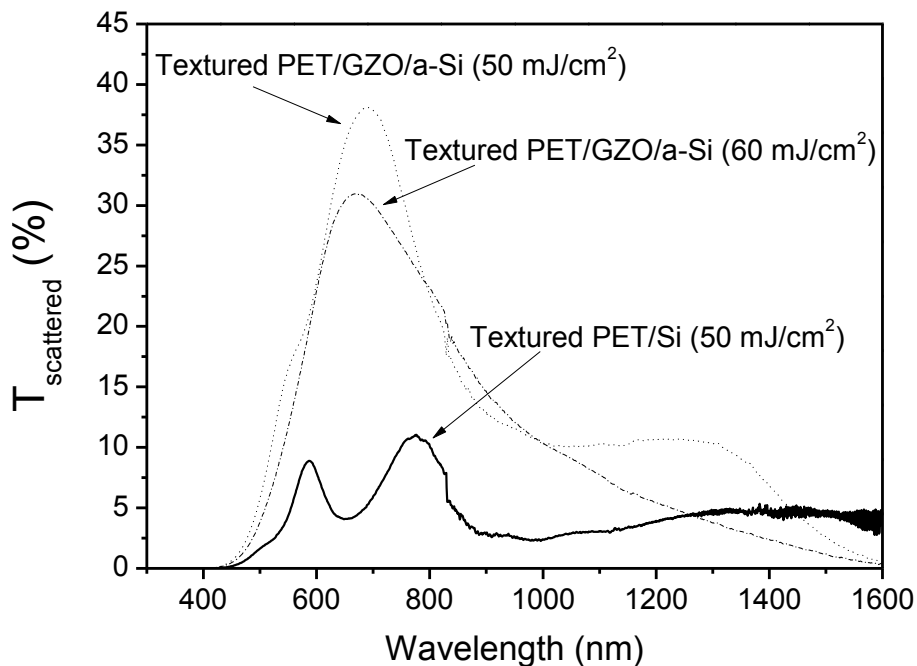


Fig. 4.10: Transmittance of scattered light by $125 \mu\text{m}$ thick PET substrates covered with $\sim 700 \text{ nm}$ of ZnO:Ga and 250 nm of a-Si:H. Two of the substrates are laser textured using fluences of 50 and 60 mJ/cm^2 before GZO deposition. The transmittance of a substrate treated with 50 mJ/cm^2 and covered only with a-Si is given for comparison.

Independently of the texture, the ZnO layer increases the absorption of the sample, as we can see by comparing the sample without ZnO with any of the others that have a ZnO layer as shown in fig. 4.11. Even the sample PET/GZO/a-Si:H without laser

texturization has a lower total transmittance as compared to the laser treated PET/a-Si:H sample.

Comparing the samples with and without ZnO treated with 50 mJ/cm^2 , we see a drastic reduction in scattered transmittance (from 38 to 6% at 700 nm) and an increase in total transmittance (from 46 to 82% at 780 nm) for the sample without ZnO. It shows that the ZnO layer is also playing an important role in the scattering process. The texture of the substrate increases the roughness of the ZnO and consequently the scattering at the ZnO/a-Si (or ZnO/air) interface. When the ZnO is absent the texture of the substrate is not enough to promote scattering.

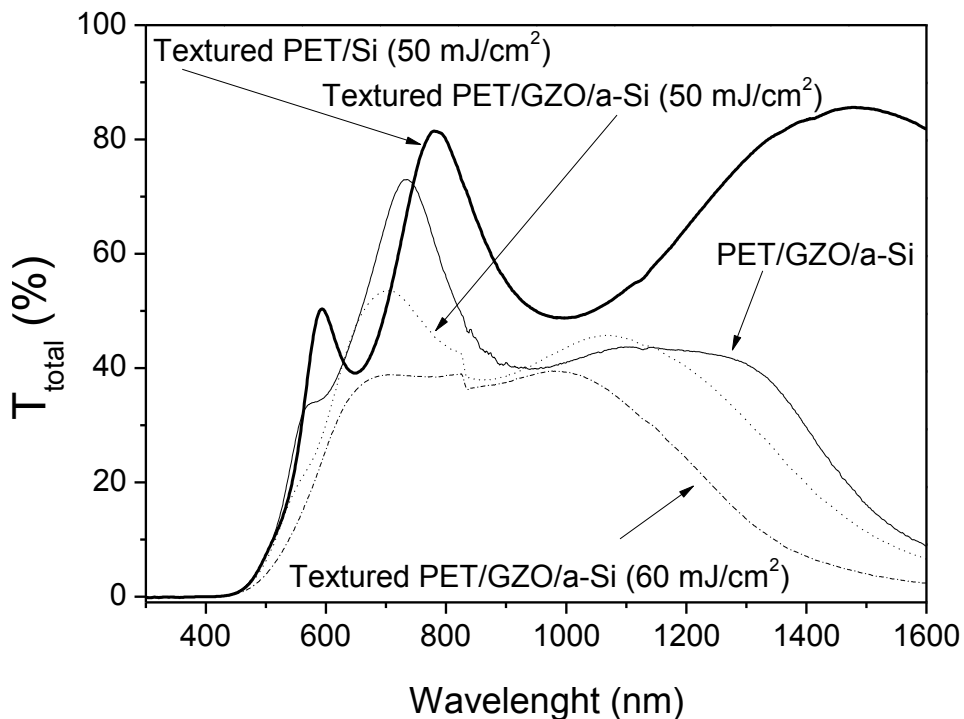


Fig. 4.11: Total transmittance for the same group of samples shown in fig. 4.10

On the other hand, scattering at the rough ZnO/a-Si (or ZnO/air) interface increases the probability of total internal reflection and light absorption within the ZnO layer. This increase of parasitic absorption induced by the texture could explain the lower transparency after the laser treatment. The haze and roughness for the textured samples covered with ZnO and a-Si:H can be seen in figures 4.12 and 4.13. Figure 4.12 shows the haze ($T_{\text{scattered}}/T_{\text{total}}$) of the same samples from figures 4.10 and 4.11, where it is clearly seen that the haze increases dramatically in the samples with ZnO.

Figure 4.13 shows the haze as a function of roughness for four different wavelengths of a set of samples irradiated with different laser fluences. It shows that there is a trend

for the haze to be maximal at the roughness value of 30 nm independently of the wavelengths region. It is also seen that the haze is higher for the visible region of the spectrum (500 and 800 nm).

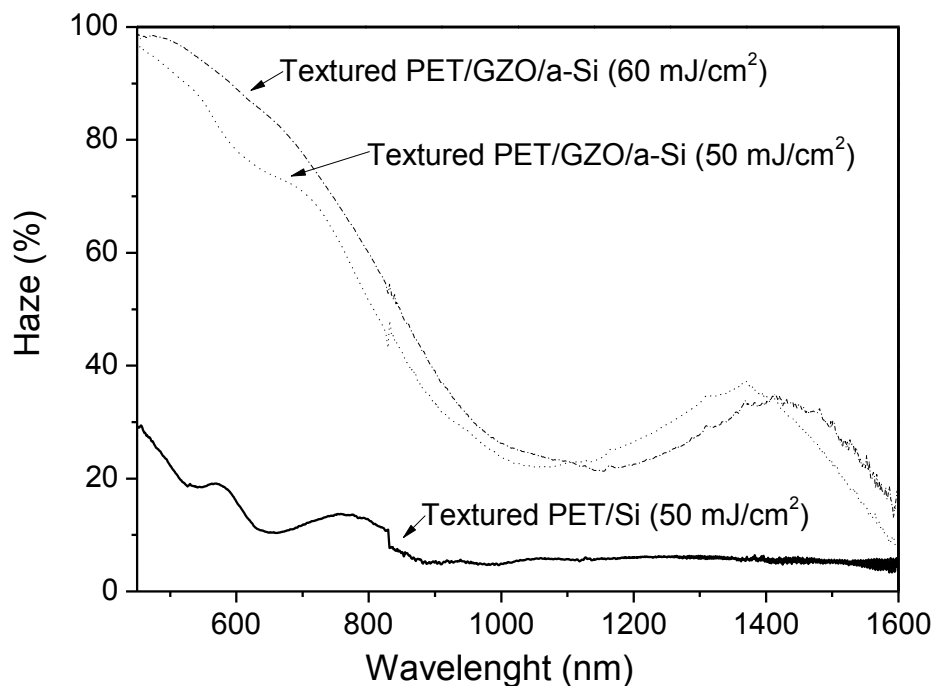


Fig. 4.12: Haze for the same group of samples shown in figs. 4.10 and 4.11.

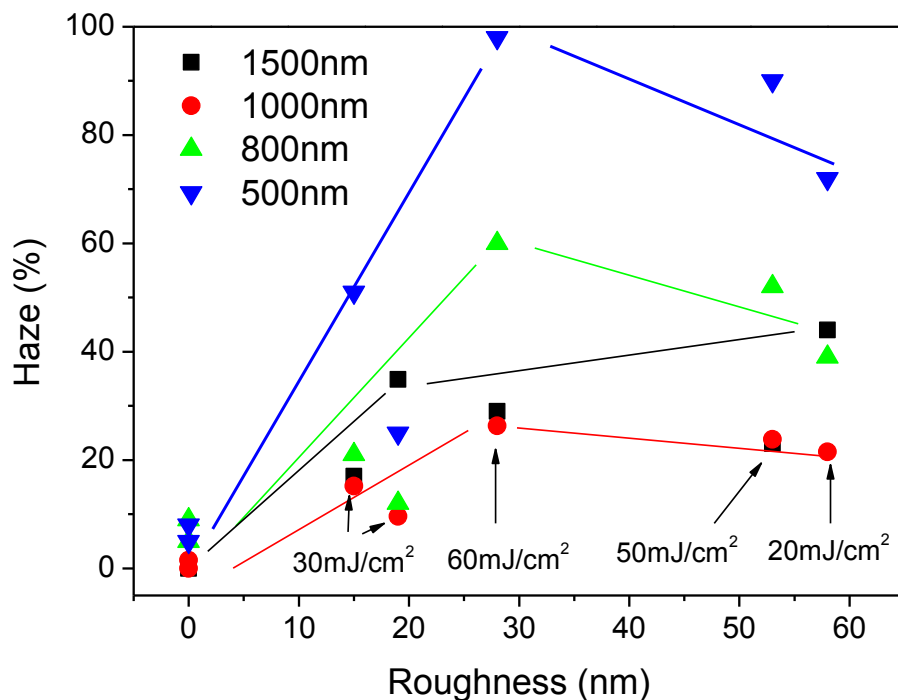


Fig. 4.13: Haze as a function of roughness for four different wavelengths of a set of samples irradiated with different laser fluences. Lines are just guides to the eye.

4.7 Conclusions

ZnO films doped with Ga and Al were deposited at room temperature on PEN and PET substrates with optical transmittance in the visible ~80%. The resistivity of ZnO:Ga films is $8.8 \times 10^{-4} \Omega \cdot \text{cm}$ and that of ZnO:Al is $2.6 \times 10^{-3} \Omega \cdot \text{cm}$. Films are polycrystalline with a low crystalline fraction.

Flexible amorphous superstrate p-i-n solar cells were fabricated on PEN with efficiencies of ~4.5 - 5%, and substrate n-i-p solar cells on PI with efficiencies of ~6 - 6.5%. The efficiencies were limited by low current-densities (J_{sc}) and low fill factors (FF), with high series resistances (R_s).

Laser texturing of plastic substrates increased dramatically the scattered transmittance (from 1.5 to >40%) and scattered reflectance (from 3 to 30%). However, the total transmittance and total reflectance decreased markedly in both cases.

References

- [1] J. Escarre et al, *Solar Energy Materials and Solar Cells*, **87** (2005) p. 333.
- [2] C. Bundesmann et al., *Appl. Phys. Lett.* **83** (10) (2003) p. 1974.
- [3] J.M. Calleja, M. Cardona, *Phys. Rev. B*, **16** (1977) p. 3753.
- [4] G.Heiland et al., *Solid State Physics*, ed. F.Seitz and D.Turnbull, Academic, New York, **8** (1959) p. 191.
- [5] S.K. Sharma and G.J. Exarhos, *Solid State Phenom.* **55** (1997) p. 32.
- [6] M. Snure, A.Tiwari, *J. Appl. Phys.* **104** (2008) p. 73707.
- [7] A. Banerjee, S. Guha, *Journal of Applied Physics*, **69** (1991) p. 1030.
- [8] T. Söderström, F.-J. Haug, X. Niquille, C. Ballif, *Progress in Photovoltaics: Research and Applications*, **17** (2009) p. 165.
- [9] J. Bailat, V. Terrazzoni-Daudrix, J. Guillet, F. Freitas, X. Niquille, A. Shah, C. Ballif, T. Scharf, R.Morf, A. Hansen, D. Fischer, Y. Ziegler, A. Closset, In *Proceedings of 20th European PVSEC* (2005) p. 1529.
- [10] J. Yang, A. Banerjee, S. Guha, *Applied Physics Letters*, **70** (1997) p. 2975.
- [11] K. Saito, M. Sano, H. Otsoshi, A. Sakai, S. Okabe, K. Ogawa, In *Proceedings of 3rd World PVSEC*, Osaka, Japan (2003) p. 2793.
- [12] M. Tanda, K. Tabuchi, M. Uno, S. Kato, Y. Takeda, S. Iwasaki, Y. Yokohama, T. Wada, M. Shimosawa, Y. Sakakibara, A. Takano, H. Nishihara, H. Enomoto, T. Kamoshita, In *Proceedings of 31st IEEE PVSC*, Lake Buona Vista, USA (2005) p. 1560.
- [13] F.-J. Haug, T. Söderström, M. Python, V. Terrazzoni-Daudrix, X. Niquille, C. Ballif, *Solar Energy Materials and Solar Cells*, **93** (2009) p. 884.
- [14] P. Alpuim, G.M. Junior, S.A. Filonovich, P. Roca i Cabarrocas, J.-E. Bouree, E.V. Johnson, Y.M. Soro, In *Proceedings of 23rd European PVSEC* (2008) p. 2455.
- [15] K. Tao, D. Zhang, L. Wang, J. Zhao, H. Cai, Y. Sui, Z. Qiao, Q. He, Y. Zhang, Y. Sun, *Solar Energy Materials and Solar Cells*, **94** (2010) p. 709.
- [16] A. Shah, ed., *Thin-film Silicon Solar Cells*, First edition, EPFL Press (2010).
- [17] L. Jiang, J.H. Lyou, S. Rane, E.A. Schiff, Q. Wang, and Q. Yuon, In *Proceedings of Materials Research Society Symposium*, **609** (2000).
- [18] Q.Wang, E. Iwaniczko, Y. Xu, W. Gao, B.P. Nelson, A.H. Mahan, R.S. Crandall, and H.M. Branz, In *Proceedings of Materials Research Society Symposium*, **609** (2000).
- [19] M. Zeman, R.A.C.M.M. Van Swaaij, M. Zuiddam, J.W. Metselaar, and R.E.I. Schropp, In *Proceedings of Materials Research Society Symposium*, **557** (1999) p. 725.

Chapter 5

5 Microcrystalline silicon solar cells on flexible PI substrate

In thin film silicon solar cells on opaque substrates in n-i-p deposition sequence where the textured TCO (transparent conductive oxide) layer serves as a back reflector, one can independently optimize the morphology of the TCO layer without compromise on transparency and conductivity of this layer and further adjust the electro-optical properties of the back contact by using additional layers on top of the textured TCO. In the present work, we use this strategy to obtain textured back reflectors for solar cells in n-i-p deposition sequence on non-transparent flexible plastic foils. Gallium doped ZnO (ZnO:Ga) films were deposited on polyimide substrates by DC magnetron sputtering at a temperature of 200°C. A wet-chemical etching step was performed by dipping the ZnO:Ga covered foil into a diluted HCl solution. The textured ZnO:Ga is then coated with a highly reflective Ag/ZnO double layer. On this back reflector we develop thin film silicon solar cells with a microcrystalline silicon absorber layer. The current density for the cell with the textured ZnO:Ga layer is ~ 23 mA/cm², 4 mA/cm² higher than the one without such layer, and a maximum efficiency of 7.5% is obtained for a 1cm² cell.

5.1 Introduction

For high efficiency of amorphous (a-Si:H) and microcrystalline ($\mu\text{-Si:H}$) thin film silicon solar cells, light trapping of the incident light within the silicon absorber layers becomes crucial in order to further reduce the cell thickness, which leads to reduction of the light-induced degradation effects for a-Si:H material [10] and more effective cycle times in production for both a-Si:H and $\mu\text{-Si:H}$ solar cells [2]. Light scattering at the interfaces is usually achieved by texturing the front TCO electrodes and/or the back reflectors [11–14]. Some TCO materials already have a suitable texture in the as-deposited state. On plastic foils, ZnO textured in the as-deposited state obtained by LP-CVD or 2D periodic structures have been used to provide light trapping in the active layers of n-i-p devices [2,7]. Sputter-deposited ZnO can be textured by a post-deposition wet-chemical etching step [15,16]. For the n-i-p deposition sequence in substrate configuration where the textured TCO serves as a back reflector, this approach has the advantage of using an optimized morphology of the TCO layer, where the electro-optical properties can be adjusted by using additional layers on top of the textured TCO. This technique has been used successfully for solar cells in both p-i-n and n-i-p deposition sequence on transparent glass substrates [11,17]. In the present work, we use this strategy to obtain textured back reflectors for n-i-p solar cells on flexible polyimide foil.

5.2 Experimental details

Microcrystalline thin film silicon solar cells are prepared on $10\times 10\text{ cm}^2$ and $125\text{ }\mu\text{m}$ thick PI foils. The substrates for smooth cells are covered with a thermally evaporated 700 nm Ag layer and an 80 nm sputtered ZnO:Ga, both deposited at room temperature. In order to obtain rough cells, an 800 nm ZnO:Ga layer is deposited directly on PI by DC magnetron sputtering at a substrate temperature of $200\text{ }^\circ\text{C}$. This layer is textured by a post-deposition wet-chemical etching in a 0.5% diluted HCl solution for 30 seconds. The back contact is finalized with an additional highly reflecting Ag/ZnO double layer that conformally covers the textured ZnO:Ga surface.

The thin film silicon layers are deposited in n-i-p sequence by plasma enhanced chemical vapor deposition (PECVD) using very high frequency excitation (81.36 MHz).

The substrate temperature is 200 °C for intrinsic and doped layers. The power density and chamber pressure for deposition of intrinsic layers are 210 mW/cm² and 7.5×10⁻¹ Torr, respectively. Doped layers are deposited at power densities and pressures of 470 mW/cm² and 2.3 Torr for n-layers, and 140 mW/cm² and 7.5×10⁻¹ Torr for p-layers. The hydrogen dilution or silane/hydrogen gas mixture is, alternatively, defined in this chapter as silane concentration SC, i.e. the ratio between the silane gas flow to the process chamber and the total gas flow ($SC = [SiH_4] / ([SiH_4] + [H_2])$). A low SC is equivalent to a high hydrogen dilution. For the intrinsic layers, SC is varied between 5% and 7%.

The front transparent contacts made of 70 nm thick ITO layers are prepared by radio-frequency (RF) magnetron sputtering at room temperature using a In₂O₃:SnO₂ target (95/5 wt.%) in an argon/oxygen atmosphere with relative oxygen content, defined as $[O_2] / [O_2 + Ar]$, of 0.1%.

The individual solar cells with an area of 1×1 cm² are defined by using a shadow mask during ITO deposition on the 10×10 cm² substrate. Front metal finger electrodes are prepared by silver evaporation. Finally, standard annealing procedure of finished solar cells is performed in air at 160°C for 30 minutes. The complete device layer sequences are for smooth cells: PI/Ag/ZnO:Ga/n-i-p/ITO and for rough cells: PI/textured ZnO:Ga/Ag/ZnO:Al/n-i-p/ITO. Figure 5.1 shows schematics of the solar cells on PI on smooth (fig. 5.1a) and rough (fig. 5.1b) back reflectors.

For comparison solar cells are also deposited on glass substrates with the same layer sequences.

The solar cell parameters open circuit voltage (V_{oc}), fill factor (FF) and short circuit current density (J_{sc}) are determined from current-voltage (I-V) measurements under simulated AM1.5G illumination at 25 °C. The external quantum efficiency (EQE) is obtained from spectral response measurements in the range of 300-1100 nm. The integrated current from the EQE curves under short circuit conditions is used to calculate the conversion efficiency in order to avoid possible effects from current collection around the 1cm² solar cells or from imprecision in determination of the cell area.

Raman spectroscopy is used to evaluate the crystalline volume fraction of the intrinsic layers in the solar cells. Raman measurements are performed directly on the solar cells using a frequency-doubled Nd:YAG laser with excitation wavelength of 532 nm.

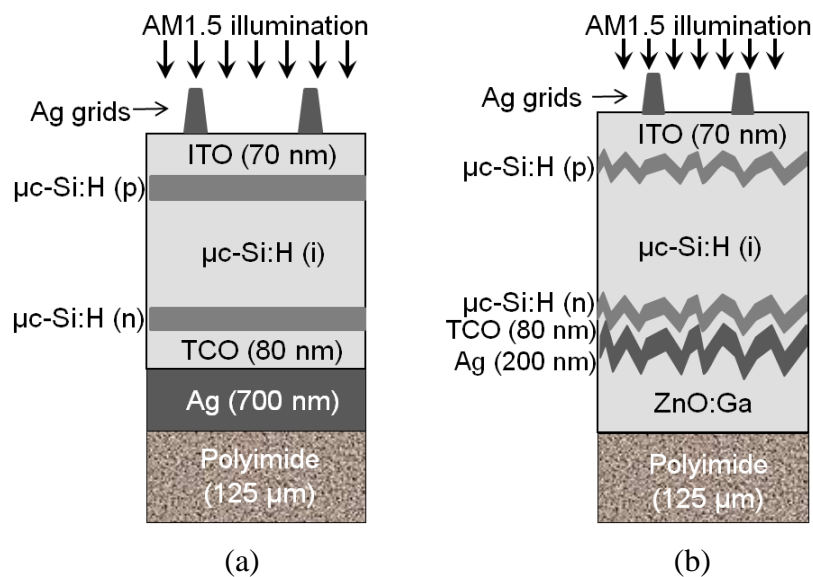


Fig. 5.1: Structures of the solar cells on PI without (a) and with (b) textured ZnO:Ga layer.

5.3 n-i-p solar cells on smooth PI substrate

Figure 5.2 shows the performance parameters of solar cells deposited on the smooth PI/Ag(700 nm)/ZnO(80 nm) substrate as a function of silane concentration (SC) of the *i*-layer. For reference and in order to assess the effect of the substrate on the performance of the solar cells, we prepared identical cells on smooth glass covered with a standard Ag/ZnO back reflector, optimized for glass substrate. We observed a similar trend of the performance parameters for the cells on PI when compared to the ones on glass. However, the V_{oc} was around 20-40 mV lower for the cells on PI. A reason for the lower V_{oc} could be the higher *i*-layer crystallinity of the cells deposited on PI as measured by Raman spectroscopy on the solar cells. This is shown in fig. 5.3. Why the PI substrate possibly promotes the growth of films with higher crystalline volume fraction is not clear at the moment. Despite of the apparent higher crystallinity in the *i*-layer of the solar cells prepared on PI with respect to the ones prepared on glass, the J_{sc} is lower for cells deposited at SC below 6% where one would instead expect higher carrier mobility and carrier collection at higher crystallinity. We speculate that this results from absorption losses in the Ag/ZnO back contact [11], which is not optimized for the PI substrate foil. The cell deposited with SC of 6.1% showed the highest V_{oc}

(505 mV) and FF of 70.7%. For this reason we chose the deposition conditions of this cell for further optimization of the solar cells on PI with rough TCO.

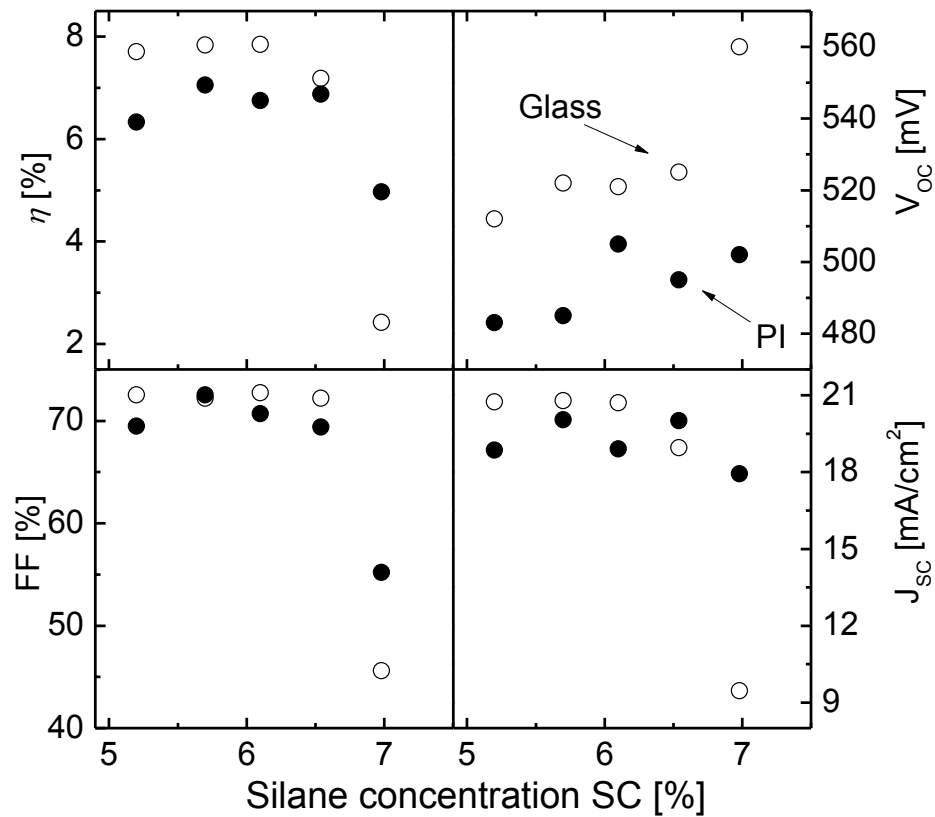


Fig. 5.2: I-V parameters of solar cells with different *i*-layer silane concentrations deposited on PI/Ag/ZnO (full symbols) and glass/Ag/ZnO (open symbols).

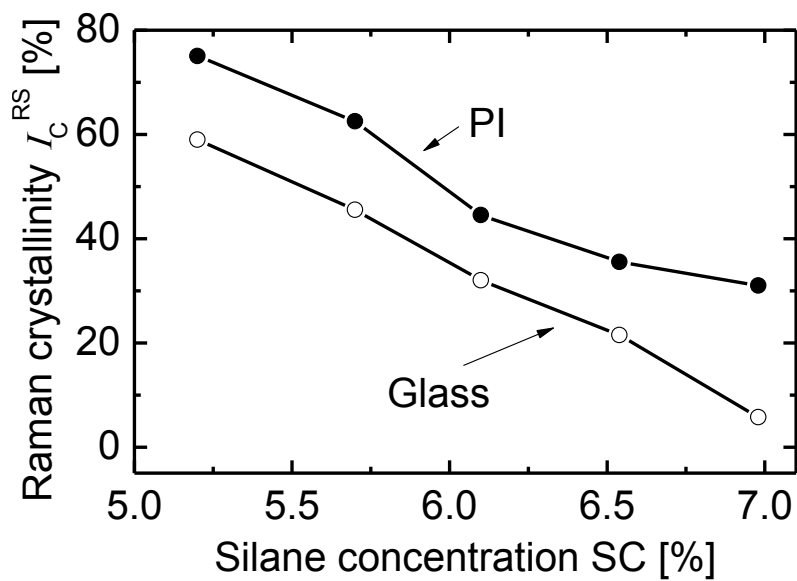


Fig. 5.3: Raman crystallinity as a function of the *i*-layer silane concentration of solar cells deposited on PI (full symbols) and glass (open symbols). Lines are guides to the eye.

Figure 5.4 shows the I-V curve of the solar cell on smooth PI and on glass substrate with an *i*-layer thickness of 1.8 μm deposited at SC = 6.1%, which yields a current density of 18.9 mA/cm^2 on PI and 20.7 mA/cm^2 on glass.

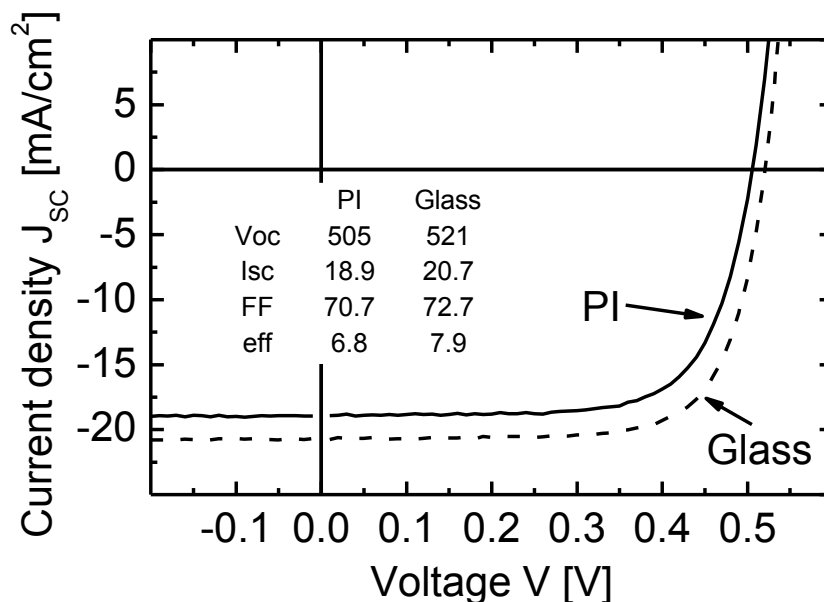


Fig. 5.4: Comparison of the I-V curves of solar cells on PI/Ag/ZnO (plain curve) and glass/Ag/ZnO (dashed curve).

5.4 n-i-p solar cells on PI with textured ZnO:Ga

To further enhance the current of cells on PI, ZnO:Ga layers were developed for application as textured back reflector [18]. This development was first carried out on glass and later transferred to application on the PI substrate¹.

Figure 5.5 shows the EQE of a solar cell prepared on ZnO:Ga deposited on PI, textured by post-deposition wet-chemical etching in HCl solution for 30 seconds, and covered with a highly reflecting Ag/ZnO double layer. For comparison the EQE of the cell on flat PI is shown. We observe a strong increase in EQE especially above 600 nm for the cell with the textured ZnO:Ga layer accompanied by efficient reduction of interference fringes. The cell on structured TCO delivers a current density of $\sim 23 \text{ mA}/\text{cm}^2$, more than $4 \text{ mA}/\text{cm}^2$ higher than the one on flat PI, and an efficiency of 7.5%

¹ These layers were developed on the scope of another PhD thesis and more details can be found in reference [18]. It was not possible to obtain the values of thickness and roughness of the ZnO:Ga layers on PI, because of the experimental challenges of performing these kind of measurements on flexible substrates.

is achieved for a 1 cm² cell. However, the FF decreased from 70.7% to 68%, and the V_{oc} was 30 mV lower. These reductions in FF and V_{oc} are expected and related to the roughness of the substrate [19]. The improvement in current was observed essentially for wavelengths above 650 nm, corresponding to the light trapping region for microcrystalline solar cells [11].

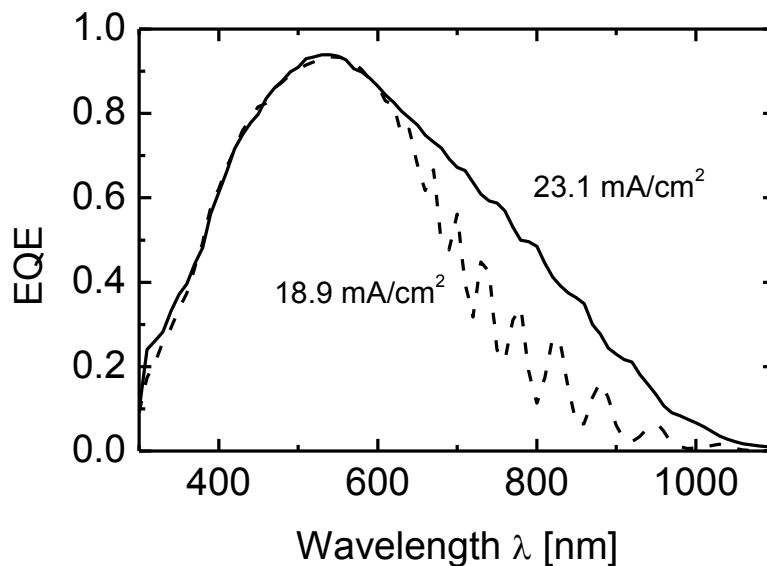


Fig. 5.5: Comparison of EQE's of solar cells on PI/Ag/ZnO (dashed line) and PI/textured ZnO:Ga/Ag/ZnO (full line).

Figure 5.6 shows the corresponding IV curve of this cell and, for comparison, the curve of an identical cell deposited on a standard textured TCO/Ag/ZnO back reflector on glass. One can clearly see the pronounced difference in V_{oc} , with lower value for the cell on PI, as discussed in section 5.3.

Table 5.1: I-V parameters of solar cells under AM1.5 illumination.

Substrate type	V_{oc} (mV)	J_{SC} (mA/cm ²)	FF (%)	η (%)
Smooth glass	521	20.7	72.7	7.9
Smooth PI	505	18.9	70.7	6.8
Glass+rough TCO	525	22.8	71	8.5
PI+rough ZnO:Ga	475	23.1	68	7.5

Results presented above and summarized in table 5.1 showed that the well-established technology of post-deposition texturing of TCO films as scattering layers to

promote light trapping in thin film silicon solar cells can be successfully transferred to application with flexible plastic substrates.

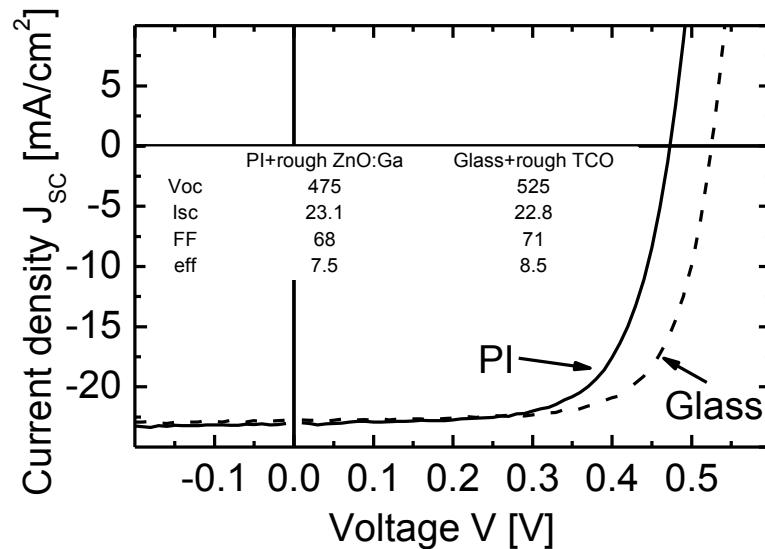


Fig. 5.6: Comparison of the I-V curves of solar cells on PI/textured ZnO:Ga /Ag/ZnO (plain curve) and glass/textured TCO/Ag/ZnO (dashed curve).

5.5 Conclusions

We have presented our development of microcrystalline single-junction n-i-p thin film silicon solar cells on flexible polyimide substrate. The results of solar cells on smooth PI showed similar behavior in terms of performance parameters in comparison to cells deposited on smooth glass. The V_{oc} was around 20-40 mV lower for the cells on PI, which is related to higher *i*-layer crystallinity of cells on PI. We developed a textured ZnO:Ga layer to promote light trapping in the solar cells on PI that yield more than 23 mA/cm² on absorbers of 1.8 μm thickness with cell efficiencies of up to 7.5%.

References

- [1] A. Banerjee, S. Guha, *Journal of Applied Physics*, **69** (1991) p. 1030.
- [2] T. Söderström, F.-J. Haug, X. Niquille, C. Ballif, *Progress in Photovoltaics: Research and Applications*, **17** (2009) p. 165.
- [3] J. Bailat, V. Terrazzoni-Daudrix, J. Guillet, F. Freitas, X. Niquille, A. Shah, C. Ballif, T. Scharf, R. Morf, A. Hansen, D. Fischer, Y. Ziegler, A. Closset, In *Proceedings of 20th European PVSEC (2005)*, p. 1529.
- [4] J. Yang, A. Banerjee, S. Guha, *Applied Physics Letters*, **70** (1997) p. 2975.
- [5] K. Saito, M. Sano, H. Otsoshi, A. Sakai, S. Okabe, K. Ogawa, In *Proceedings of 3rd World PVSEC, Osaka, Japan (2003)* p. 2793.
- [6] M. Tanda, K. Tabuchi, M. Uno, S. Kato, Y. Takeda, S. Iwasaki, Y. Yokohama, T. Wada, M. Shimosawa, Y. Sakakibara, A. Takano, H. Nishihara, H. Enomoto, T. Kamoshita, In *Proceedings of 31st IEEE PVSC, Lake Buona Vista, USA (2005)* p. 1560.
- [7] F.-J. Haug, T. Söderström, M. Python, V. Terrazzoni-Daudrix, X. Niquille, C. Ballif, *Solar Energy Materials and Solar Cells*, **93** (2009) p. 884.
- [8] P. Alpuim, G.M. Junior, S.A. Filonovich, P. Roca i Cabarrocas, J.-E. Bouree, E.V. Johnson, Y.M. Soro, In *Proceedings of 23rd European PVSEC (2008)* p. 2455.
- [9] K. Tao, D. Zhang, L. Wang, J. Zhao, H. Cai, Y. Sui, Z. Qiao, Q. He, Y. Zhang, Y. Sun, *Solar Energy Materials and Solar Cells*, **94** (2010) p. 709.
- [10] D.L. Staebler, C.R. Wronski, *Applied Physics Letters*, **31** (1977) p. 292.
- [11] J. Müller, B. Rech, J. Springer, M. Vanecek, *Solar Energy*, **77** (2004) p. 917.
- [12] S. Fay, L. Feitknecht, R. Schlüchter, U. Kroll, E. Vallat-Sauvain, A. Shah, *Solar Energy Materials and Solar Cells*, **90** (2006) p. 2960.
- [13] J. Hüpkes, B. Rech, O. Kluth, T. Repmann, B. Zwaygardt, J. Müller, R. Drese, M. Wuttig, *Solar Energy Materials and Solar Cells*, **90** (2006) p. 3054.
- [14] T. Tohsophon, J. Hüpkes, H. Siekmann, B. Rech, M. Schultheis, N. Sirikulrat, *Thin Solid Films*, **516** (2008) p. 4628.
- [15] O. Kluth, B. Rech, L. Houben, S. Wieder, G. Schöpe, C. Beneking, H. Wagner, A. Löffl, H. Schock, *Thin Solid Films*, **351** (1999) p. 247.
- [16] W. Böttler, V. Smirnov, J. Hüpkes, F. Finger, *Journal of Non-Crystalline Solids* (2012) doi:10.1016/j.jnoncrysol.2011.12.100.
- [17] W. Böttler, V. Smirnov, A. Lambertz, J. Hüpkes, F. Finger, *Phys. Status Solidi C*, **7** (2010) p. 1069.
- [18] M. Warzecha, PhD Thesis, Forschungszentrum Jülich, Germany (2012).
- [19] T. Söderström, F.-J. Haug, V. Terrazzoni-Daudrix, C. Ballif, *Journal of Applied Physics*, **103** (2008) p. 114509.

Chapter 6

6 Shape sensors based on piezoresistive doped $\mu\text{-Si:H}$

This chapter describes the manufacture of a thin *skin-like* piezo-resistor strain-sensing membrane and the miniaturization of piezoresistive sensor arrays based on n-type hydrogenated microcrystalline silicon thin films ($\mu\text{-Si:H}$) deposited on flexible polyimide substrates (PI). The $\mu\text{-Si:H}$ thin films, prepared by hot-wire chemical vapor deposition, have a piezoresistive gauge factor (GF) of -32.2.

Six of the sensors batch processed on the 15 μm -thick membrane were cut and used in a test structure to track the simulated movement of the head of a bedridden patient. The sensors were glued to both sides of a 3 mm-thick acrylic rectangular plate, to collect strain data from the tensile and compressive surfaces of the plate upon bending. The sensor output electrical signal was obtained by inserting the sensors into Wheatstone bridge circuits and recording the output voltage of the bridge as a function of the sensor/plate deformation. The results using quarter-, half- and full-bridge configurations were compared.

In order to give a further step toward a shape sensitive electronic textile, nine sensors were glued and interconnected using a machine sewed conductive thread and preliminary tests on their output response under random loading conditions were performed.

Test structures, consisting of microresistors having lateral dimensions in the range from 50 to 100 μm and thickness of 120 nm were defined in an array by reactive ion etching. Metallic pads, forming ohmic contacts to the sensing elements, were defined by a lift-off process.

6.1 Introduction

The piezoresistive property of crystalline silicon has long been known to scientists and engineers [1] and most strain gauge sensors use that property as their operation principle [2]. More recently, the piezoresistive effect has also been found in doped hydrogenated microcrystalline silicon thin films ($\mu\text{c-Si:H}$) [3,4]. In particular, the combination of the mechanical properties of plastic substrates with the electrical properties of doped $\mu\text{c-Si:H}$ deposited at 100-150°C opened a way to design new types of piezoresistive sensors [3,6].

The piezoresistive property of doped $\mu\text{c-Si:H}$ deposited at low substrate temperature ($\leq 150^\circ\text{C}$) on flexible polyimide (PI) and polyethylene naphthalate (PEN) substrates by hot-wire chemical vapor deposition (HWCVD) was investigated in previous studies [3,5] and the results showed that GF is positive for p-type films and is negative for n-type films. It is consistent with the idea that because the films are semi-crystalline and isotropic, at least within planes parallel to the substrate, they retain the sign of the largest (in absolute value) piezoresistive coefficient of c-Si which is $\pi_{44}=138\times 10^{-11} \text{ Pa}^{-1}$ for p-type and $\pi_{11}=-102\times 10^{-11} \text{ Pa}^{-1}$ for n-type material. π_{11} denotes the fractional change in resistivity for a stress parallel to the current flow, while π_{44} denotes the fractional change in resistivity for a shear stress (perpendicular to the current flow). These studies are now extended to flexible piezoresistive sensor fabrication by manufacture of a thin “skin-like” piezo-resistor sensing membrane followed by cutting and transfer to other surfaces. Strain sensors fabricated using the first of these approaches are characterized in the static and quasi-static actuation modes and are reported here. A large sensor in the shape of a strip is used to monitor the movements of a plastic plate that simulates the movements of the head of a bedridden patient. Piezoresistive sensors are embedded in a textile fabric in order to obtain a shape sensitive electronic textile to be tested in a clinical environment with the aim to perceive levels of discomfort in patients that have lost the ability to change their posture by analysing the movements of the body that healthy people usually do under similar conditions.

6.2 Experimental details

6.2.1 Film preparation

Films are deposited in a load-locked high-vacuum system composed of twin chambers for HWCVD and rf-PECVD. N-type $\mu\text{-Si:H}$ films are deposited by HWCVD from gaseous mixtures of silane ($F_{\text{silane}} = 1.86$ sccm), hydrogen ($F_{\text{H}_2} = 33.9$ sccm) and phosphine – 98% diluted in hydrogen ($F_{\text{PH}_3/\text{H}} = 1.862$ sccm) resulting in a 95% hydrogen diluted reactive gas mixture. A working pressure of 40 mTorr is used. The substrate holder is placed 7 cm above a single S-shaped tantalum filament, 0.5 mm thick and 14 cm long. The filament is resistively heated ($T_{\text{fil}} \sim 1750$ °C) for deposition, using a DC power supply ($I_{\text{fil}} = 14$ A) that pyrolytically decomposes the reactant gases at the filament surface. Substrates are polyimide foils (PI) with area 33×33 mm². Substrate temperature is 150 °C for all depositions.

6.2.2 Sensor fabrication

Large-area sensors are fabricated by deposition through 0.4 mm-thick stainless steel masks on a 15 μm -thick PI membrane. The first mask is used for definition of the piezoresistive element island (3×3 mm²). In the next step, Al is thermally evaporated through a second mask that defines the parallel contacts overlapping the island, the 200 μm -wide interconnects, and the pads. Piezoresistor dimensions are set by the gap between the parallel contacts (1 mm), the width of the island (3 mm) and the thickness of the films (~ 100 nm). The squared plastic substrates are then cut into individual sensors. Each sensor sits on a piece of 15 μm -thick PI with area $\sim 5 \times 5$ mm².

6.2.3 Piezoresistive response characterization

Piezoresistive gauge factor, GF , is measured by four-point bending tests, where each sensor is glued to a larger piece of 125 μm thick polyimide that is inserted in a Shimadzu-AG-IS 500 N Testing Instrument with characteristic lengths 10-30 mm (distance between the inner and the outer points of application of the force). Control software is Trapezium2 from Shimadzu Corp. Four other sensors are glued onto an acrylic plate, with dimensions 250 mm \times 90 mm \times 3 mm, two of them attached to the upper surface of the plate and another two to the bottom surface. The bendable acrylic

plate is used to simulate the surface of a supporting cushion of a virtual bedridden patient, with the width of a human head (250 mm). The movement of the human head is represented by the up-and-down displacement of the inner bars of the 4-point instrument, and its contact area with the cushion is the 10 mm region between the inner points. For each piezoresistor, the relative resistance change, $\frac{\Delta R}{R_0}$, where R_0 is the undeformed resistance of the sensor and ΔR is the change in resistance upon bending, is related to the applied strain, ε , by the equation $\frac{\Delta R}{R_0} = GF\varepsilon$. In four-point bending experiments, the shape of the bended specimen can be calculated from the theory of pure bending of a plate to a cylindrical surface, valid between the inner loading points [7]. In this region, the radius of curvature, r , is constant and given by:

$$r = \frac{3al - 4a^2}{6z} \quad (1)$$

where z is the displacement of the inner loading bars, a is the distance between the outer and inner loading bars and l is the distance between outer bars in the four-point bending system (see fig. 6.1).

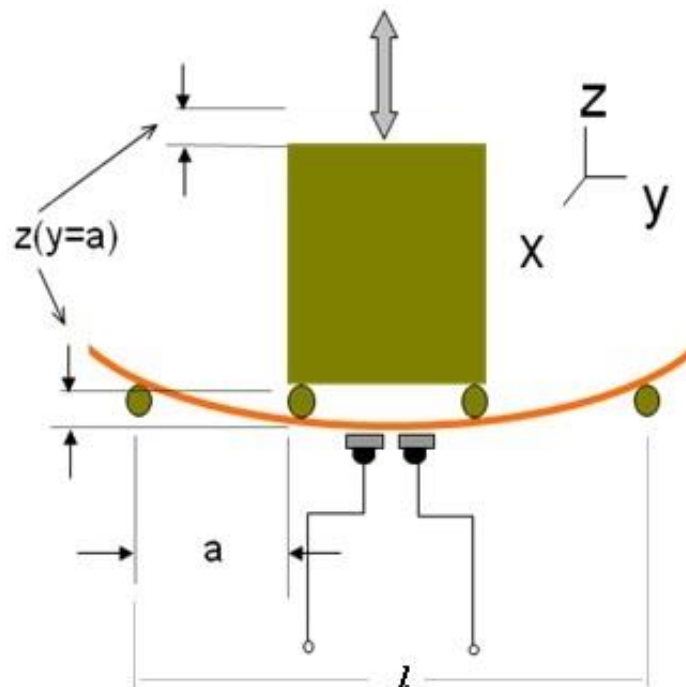


Fig. 6.1: Schematic diagram of the 4-point bending instrument (Shimadzu-AG-IS 500 N) and contacts used to characterize the piezoresistive response of the sensors. The outer and inner loading bars are represented by green circles and the contacts by gray rectangles and lines in lower part of figure.

Assuming that the neutral plane of the sensor (substrate + film) is symmetrically placed between the two free surfaces of the substrate and no slip occurs at the film-substrate interface, the strain in the film in the longitudinal direction is:

$$\varepsilon = \frac{3dz}{3al - 4a^2} \quad (2)$$

where d is the substrate thickness.

For the first set of experiments (measurement of the GF of the sensors) $a = 10$ mm and $l = 3a$ and thus eq. (2) yields, upon substitution:

$$\varepsilon = \frac{3dz}{5a^2} \quad (3)$$

For the second set of experiments (simulation of the movement of a bedridden patient), $a = 10$ mm and $l = 10.5a$ and thus, upon substitution in eq. (2), one obtains:

$$\varepsilon = \frac{3dz}{27.5a^2} \quad (4)$$

The signal of the sensors is the output voltage of a Wheatstone bridge circuit in which the sensors are inserted in the quarter-, half- or full-bridge configuration (see table 6.1). A NI-USB 6210 data acquisition module connected to a PC laptop completed the setup. In some experiences the resistance of the sensors is directly monitored by connecting the sensor pads to a digital multimeter that communicated with the PC laptop through a GPIB connection.

The sensitivity of the Wheatstone bridge circuit can be expressed in terms of the change in bridge output voltage due to a small change in the resistance of one of the bridge arms, generally the unknown resistance arm, i.e. ΔR_x . A general expression for the change in output voltage of the bridge, ΔV_{out} , with respect to a small change in R_x is:

$$V_{out} = -V_{in} \frac{R}{(R+R_x)^2} \Delta R_x \quad (5)$$

where V_{in} is the input voltage, and R and R_x are the known and unknown resistances of one bridge arm, respectively.

The maximum sensitivity is achieved when the resistors in the bridge have the same resistance. Hence by letting $R = R_x$ in eq. (5) we get an alternate expression for the bridge sensitivity:

$$\frac{\Delta V_{out}}{\Delta R_x} = -\frac{V_{in}}{4R_x} \quad (6)$$

One of the problems of strain measurement is thermal effect. Besides external force, changing temperatures elongate or contract the measuring object with a certain linear expansion coefficient. Accordingly, a strain gauge bonded to the object bears thermally-induced apparent strain. Other interference effects can affect the strain measurement, e.g. humidity, hydrostatic pressure, magnetic fields, radiation, etc. –Some of these effects can be compensated by the appropriate use of the Wheatstone bridge circuit. If, for example, the temperature variation occurs during the mechanical loading of the structural part, the strain signal will be a composite with one component of the desired effect from the mechanical stress, ε_M , and with other component of the undesired effect from the thermal expansion, ε_W :

$$\frac{\Delta R}{R_0} = GF(\varepsilon_M + \varepsilon_W) \quad (7)$$

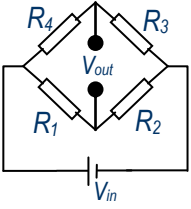
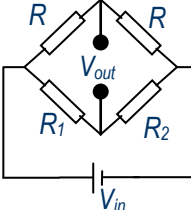
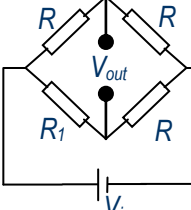
If four strain gauges are applied to the specimen and connected into a full bridge as shown in table 6.1, we have:

$$\frac{V_{in}}{V_{out}} = \frac{GF}{4} [(\varepsilon_M + \varepsilon_W)_1 - (-\varepsilon_M + \varepsilon_W)_2 + (\varepsilon_M + \varepsilon_W)_3 - (-\varepsilon_M + \varepsilon_W)_4] = \frac{GF}{4} 4\varepsilon_M \quad (8)$$

We can see that the thermal component in the total strain, ε_W , has the same sign for all strain gauges, provided they are all subjected to the same change in temperature. The interference effect, ε_W , has been compensated. The same method of compensation can be used for a half bridge, but cannot be implemented with the quarter bridge. The only way to overcome this is to use a “compensating strain gauge” to expand the quarter bridge into a half bridge. It is very important to select and apply the compensating strain gauge correctly in order to achieve the correct result. The compensating strain gauge must have the same physical properties as the “active” strain gauge; be applied in a spot where it will be subjected to the same interference effect as the active strain gauge; and

only be subjected to the interference effect and never to the quantity to measured or its side effects.

Table 6.1: Number and position of sensors, output voltage and circuit diagram for several bridge configurations used in this work.

Configuration	Number of sensors	Circuit	Output voltage, V_{out}	V_{out} (measured @ $z=10$ mm)
Full bridge	2 ($\epsilon < 0$) + 2 ($\epsilon > 0$)		$V_{out} = (GF \times \epsilon) V_{in}$	150 mV
Half bridge	1 ($\epsilon < 0$) + 1 ($\epsilon > 0$)		$V_{out} = \frac{GF \times \epsilon}{2} V_{in}$	89 mV
Quarter bridge	1 ($\epsilon < 0$) or 1 ($\epsilon > 0$)		$V_{out} = \frac{GF \times \epsilon}{4} V_{in}$	44 mV

6.3 skin-like piezoresistive sensing membranes

Figure 6.2 shows on the right axis the resistance of a “skin-like” sensing membrane as a function of time, during a four-point bending experiment consisting of 5 loading cycles. The membrane is glued to the tensile surface of a $33 \text{ mm} \times 10 \text{ mm}$ piece of $125 \mu\text{m}$ -thick polyimide with appropriate size and enough rigidity to be inserted in the 4-point bending set up.

The left axis shows the displacement of the inner loading bars, z . It can be seen that the resistance instantaneously adjusts to the displacement while the graphs are half a period out of phase. This is due to the negative gauge factor of the n-type sensor placed

on the tensile surface. When the sensor is placed on the compressive surface, the two graphs are in phase.

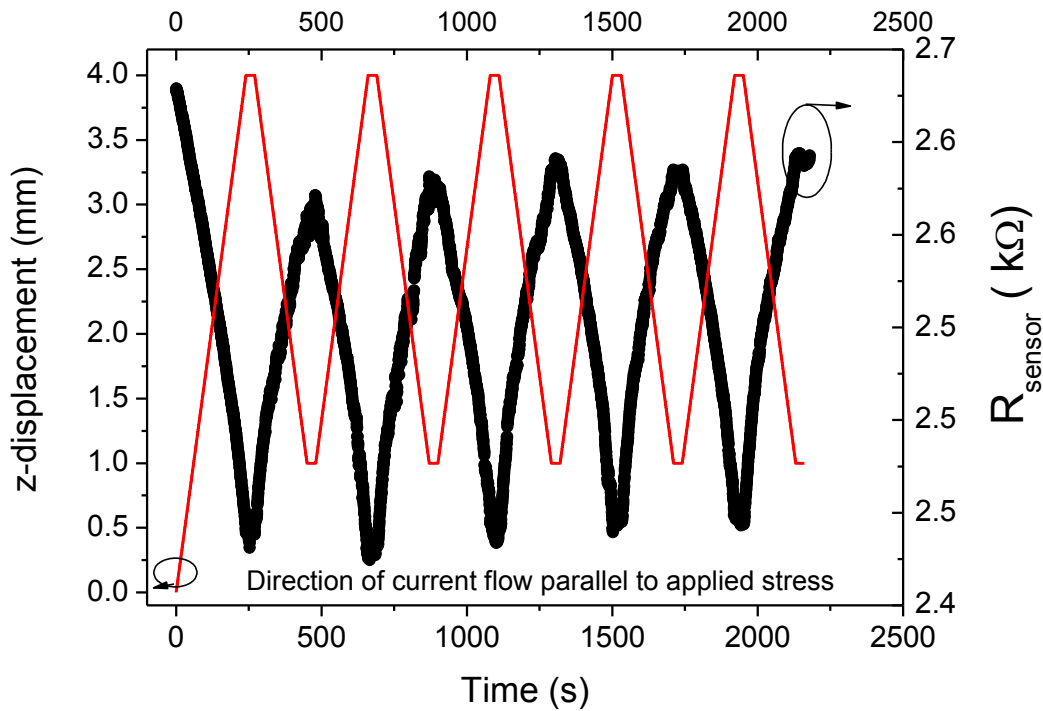


Fig. 6.2: Sensor resistance (R , right axis) and displacement of the inner loading bars (z , left axis) as a function of time in a five-cycle load-unload 4-point bending experiment.

Using the data in fig. 6.2 and eq. 3 one can calculate the relative resistance change of the sensor as a function of strain. This is plotted in fig. 6.3 which shows the data collected from the sensor under tensile ($\epsilon > 0$) and compressive strain ($\epsilon < 0$). The sensor behaves in a very symmetric way around the nominally unstrained state with a $GF \sim -30$ ($GF_{\text{compressive}} = -32.2$ and $GF_{\text{tensile}} = -29.2$). The small difference between the tensile and compressive values is due to micro-cracks that develop in the sensor and the aluminum pads that get more open or more closed, under traction or compression, respectively. These results show that very thin piezoresistive sensing membranes can be transferred to other surfaces without loss of gauge factor. This approach paves the way for successful development of new applications in the field of electro-textiles and other smart materials.

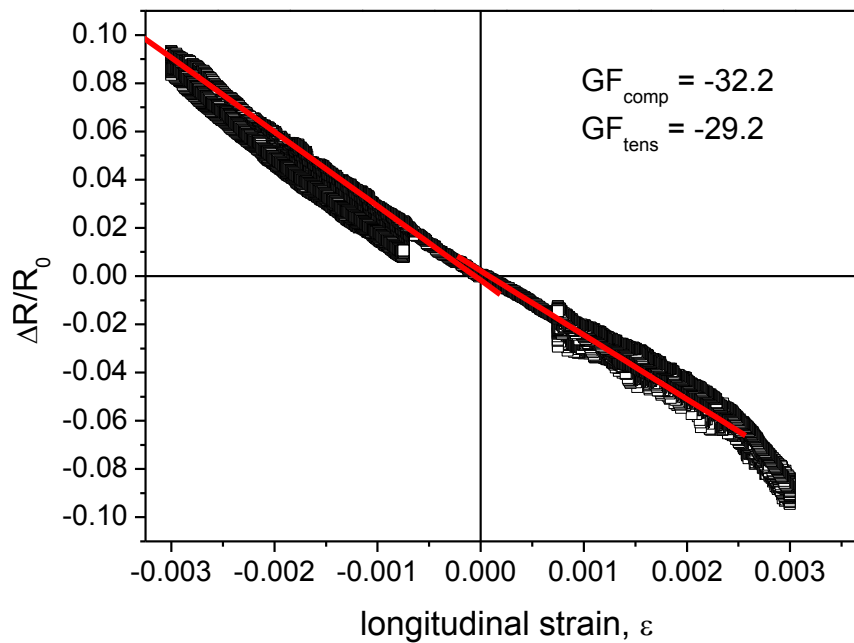


Fig. 6.3: Relative resistance change as a function of strain in 4-point bending experiments. Gauge factor is -32.2 for negative strain and -29.2 for positive strain.

6.4 Test structures for smart textiles

The fabrication of electronic systems onto substrates which are not only flexible, but also conformable to the human body, represents a breakthrough in many areas of application, such as virtual reality, teleoperation, telepresence, ergonomics, and rehabilitation engineering [8]. The possibility of realizing sensing textiles by coating traditional fabrics with smart materials (piezoresistive, piezoelectric, and piezocapacitive polymers and inorganic thin films) has opened up a means of implementing a new type of man-machine interface technology [9,10]. The innovation in this field is originated by the development of a new generation of textile sensors, combining electronics and informatics novelties, leading to the integration of multiple, smart functions into textiles based sensing interfaces, aiming to the reduction of any impediment. Smart fabrics allow the monitoring of patients over extended period, in a natural context, in biomedicine [11].

The 15 μm thin piezoresistive membranes are glued to an acrylic plate which, when actuated by the inner bars of the bending apparatus, simulated the movement of a bedridden patient's head on the surface of a hard cushion (see fig. 6.4).

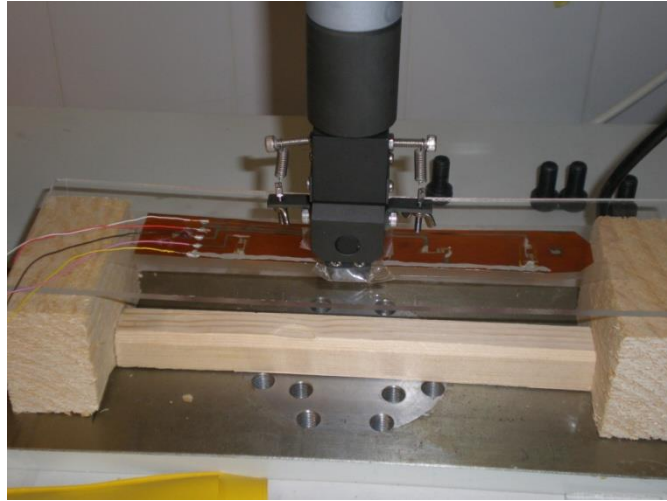


Fig. 6.4: Apparatus to simulate the movement of a bedridden patient's head on the surface of a hard cushion.

Figure 6.5 shows the resulting voltage output when the sensors are connected in the quarter- (a), half- (b), and full (c) bridge configurations, for the same amount of displacement. In the quarter-bridge circuit (see table 6.1), only one sensor is used and it is arbitrarily placed on the compressive surface of the acrylic plate, at its center. As the acrylic is loaded cyclically by the Shimadzu loading cell, the output voltage [fig. 6.5-(a)] followed the movement because of the strain induced in the sensor. The peak-to-peak voltage, corresponding to the swing between the unloaded plate condition and the maximal applied deflection, is $V_{pp} = 44 \text{ mV}$.

For the half-bridge circuit, a second sensor is added parallel to the first one (see table 6.1), but glued to the tensile surface of the acrylic plate. In this way, the two sensors are expected to undergo the same amount of strain, but with opposite signals (- for the first, + for the second). V_{out} of the bridge in this configuration is expected to be twice the value read in the quarter-bridge configuration, for the same amount of deflection. Figure 6.5(b) shows that, *grosso modo*, this is indeed the case, since V_{out} oscillates now with $V_{pp} = 89 \text{ mV}$.

Finally, the full-bridge configuration uses a second pair of piezoresistors (table 6.1) side by side with the first ones, one on the tensile and the other on the compressive surface, that are connected to opposite branches of the Wheatstone bridge and in the reverse order of the other two. In this way the output voltage of the bridge is expected to duplicate, when compared to the half-bridge V_{out} . Figure 6.5(c) shows that the behaviour of the bridge using the four piezoresistors behaves as expected, with the output voltage oscillating with $V_{pp} \sim 150 \text{ mV}$.

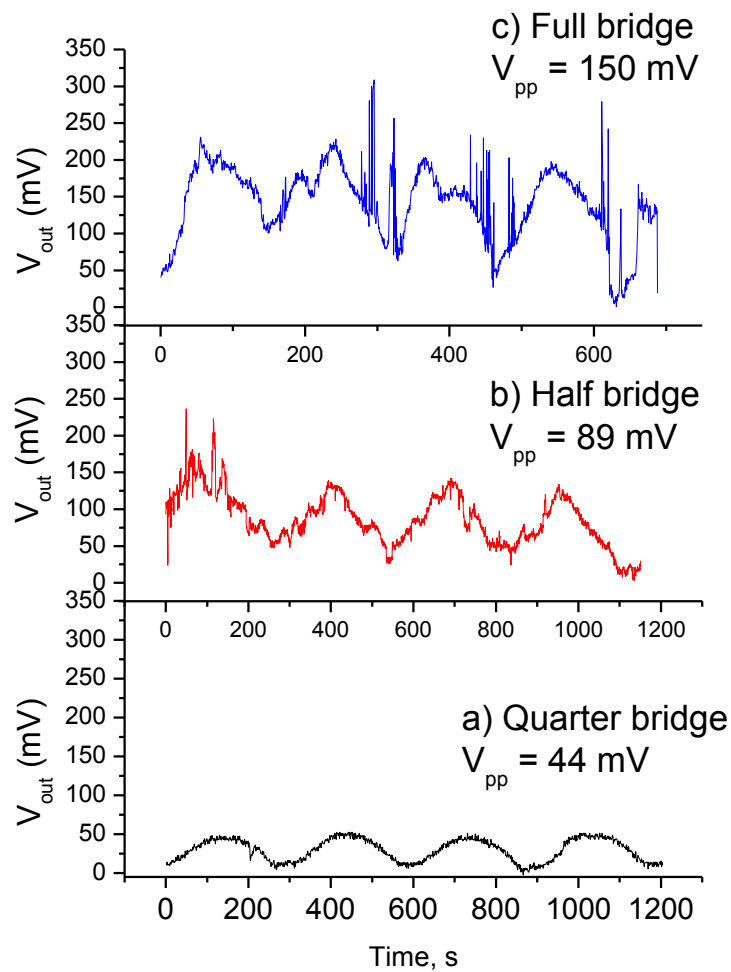


Fig. 6.5: Sensor output voltage for a) quarter-, b) half-, and c) full bridge configurations.

Figure 6.6 shows one attempt to integrate the piezoresistive sensors in a textile fabric where nine sensors are machine sewed using conductive threads. The signal of each sensor is monitored in a separate channel while the fabric is deformed under pressure of the body. The results are displayed in the right part of the figure. Although the loading conditions were quite random and some of the sensors were not responding steadily due to problems in the gluing process, it is possible to observe that several sensors responded in real time to the applied loads. Therefore it is worth improving the technological details in order to obtain a higher percentage of working sensors after the gluing and sewing process steps.

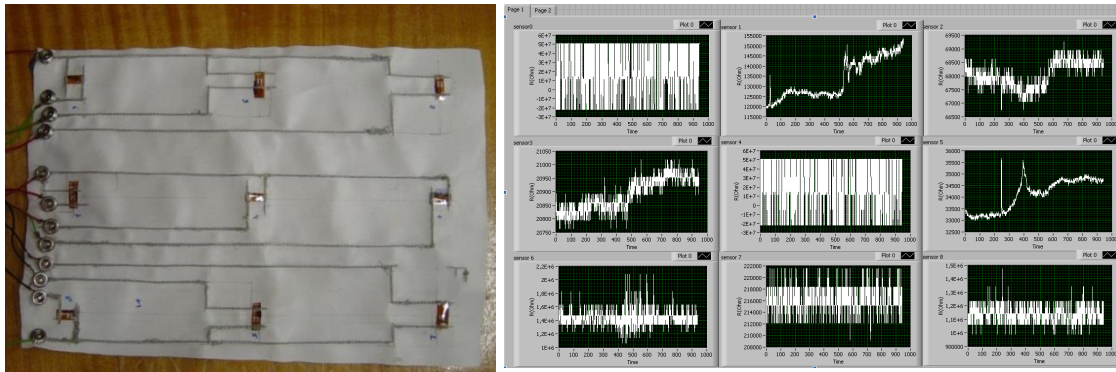


Fig. 6.6: (Left) fabric with 9 sensors glued and interconnected by machine sewed conductive threads; (Right) Sensor's output voltage for random loading conditions.

6.5 Sensor array fabrication

This section describes the fabrication of micro-devices using standard lithographic techniques with minor adaptations due to the chemistry of the plastic substrates. $\mu\text{-Si:H}$ films deposited on square shaped (side length = 35 mm) polyimide (PI) flexible substrates with thickness $d_s = 125 \mu\text{m}$ are patterned by photolithography into strain sensing microresistors in an array with seven lines and four columns. The PI substrates are glued with photoresist (PR) to a 2" Si carrier wafer for processing. Each sensing element consists of rectangular islands with lateral dimensions (length \times width) in the range from $210 \mu\text{m} \times 70 \mu\text{m}$ to $450 \mu\text{m} \times 150 \mu\text{m}$, connected to metallic leads at each end of the island and extending to large pads ($3 \text{mm} \times 2 \text{mm}$). Two masks are used to define the sensors: first, a bright field mask defined the semiconductor islands pattern; second, a dark field mask defined the electrically conductive leads and pads in a lift-off process, using a positive PR (AZ Electronic Materials GmbH).

A reactive ion etching (RIE) step is used to etch the $\mu\text{-Si:H}$ islands on the PI substrate. Under the processing conditions used (pressure = 55 mTorr, Power = 150 W, CHF_3 flow = 50 sccm, SF_6 flow = 5 sccm and O_2 flow = 5 sccm), the Si etch rate is approximately 28nm/min.

The metallic leads and pads, consisting of a tri-layered film of Ta 10 nm/ Al 40 nm/ Ta 5 nm, are deposited by ion beam deposition followed by lift-off in acetone soak.

Figure 6.7 shows the piezoresistive response, under loading by 4-point bending cycles (Shimadzu-AG-IS 500 N), of one $\mu\text{-Si:H}$ microresistor with thickness 120 nm, belonging to a larger array fabricated on a 125 μm thick polyimide substrate. Figure 6.7(a) shows the microresistor width \times length dimensions of $100 \times 100 \mu\text{m}^2$. The bright

parts of the optical micrograph are the metallic leads and the darker zone is the PI substrate. Figure 6.7(b) shows the resistance, R (thick line, left axis), and the vertical displacement, z (thin line, right axis), of the inner loading bars of the 4-point bending bridge (4PBB) as a function of time. The 4PBB is operated in a quasi-static mode (velocity of the loading bars $v = 1\text{mm/min}$) during a four-cycles loading experiment. The microresistors stand in the region between the inner loading bars of the 4PBB, on the tensile surface of the specimen. In that region the longitudinal strain in the film as a function of the displacement of the bars, assuming that the neutral plane of the sensor is symmetrically placed between the two free surfaces of the substrate, is given by eq. (2), with $l = 25\text{ mm}$ and $a = 7.5\text{ mm}$. Using eq. (2), the resistance of the microresistor can be plotted as a function of the applied strain, which is done in fig. 6.7(c). The slope of the graph is the longitudinal GF of the $n^+\text{-}\mu\text{-Si:H}$ sensing element. Here, longitudinal means that resistor current and applied strain are parallel. From the figure, $GF = -28.1$. Notice the minus sign of the GF , meaning that the resistance of the sensor decreases (increases) when tensile (compressive) strain is applied to the substrate. Hence the phase opposition between the two graphs of fig. 6.7(b).

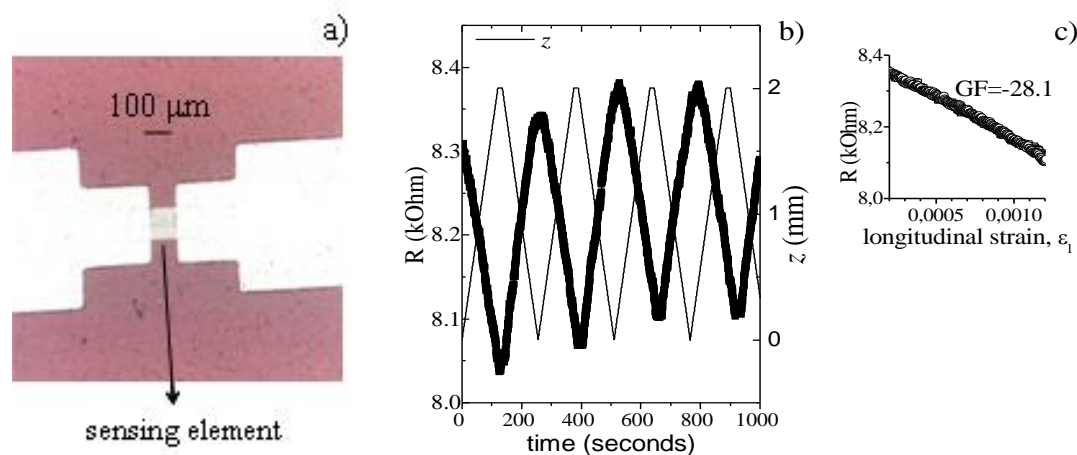


Fig. 6.7: Piezoresistive response, under 4-point bending loading cycles of one $\mu\text{-Si:H}$ microresistor with dimensions $W \times L = 100 \times 100\ \mu\text{m}^2$ and thickness 120 nm on a $125\ \mu\text{m}$ thick polyimide substrate. a) Optical micrograph of sensor and metallic leads; b) Sensor resistance, R (left axis) and vertical displacement of loading bars, z (right axis) as a function of time; c) Sensor resistance, R , as a function of strain, ε , calculated from data in b) using eq. (2). The slope is the GF (-28.1).

6.6 Conclusions

High-gauge factor ($GF = -32.2$) piezoresistive n-type sensors were fabricated using flexible thin-film silicon technology on plastic. $15\ \mu\text{m}$ -thick membrane sensors were

batch fabricated and successfully transferred to large-area surfaces. This concept allows to add sensing capabilities to many different materials and surfaces, namely to textiles. The sensor's output voltage using quarter-, half, and full-bridge configurations were dynamically tested and the results follow the predictions made by circuit analysis for conventional, rigid sensors. Nine sensors were incorporated in fabrics and interconnected using machine sewed conductive threads. Their response to a random distributed load is registered. Microresistors, with $GF = -28.1$, were fabricated on plastic substrates using standard lithographic techniques.

References

- [1] C.S. Smith, Phys. Rev. **94** (1954) p. 42.
- [2] M. Elwenspoek, R. Wiegerink, Mechanical Microsensors, Springer, New York (2001) p. 87.
- [3] P. Alpuim, V. Chu, J.P. Conde, IEEE Sens. J. **2** (2002) p. 336.
- [4] S. Nishida, M. Konagai, K. Takahashi, Jpn. J. Appl. Phys. **25** (1986) p. 17.
- [5] P. Alpuim, M. Andrade, V. Sencadas, M. Ribeiro, S.A. Filonovich, S. Lanceros-Mendez, Thin Solid Films, **515** (19) (2007) p. 7658.
- [6] P. Alpuim, S.A. Filonovich, C.M. Costa, P.F. Rocha, M.I. Vasilevskiy, S. Lanceros-Mendez, C. Frias, A. Torres Marques, R. Soares, C. Costa, Journal of Non-Crystalline Solids, **354** (19-25) (2008) p. 2585.
- [7] S.P. Timoshenko, Strength of Materials, R.E. Krieger Publ. Comp., Malabar, Flo. **93** (1958) p. 218.
- [8] V. J. Lumelsky, M. S. Shur, S. Wagner, IEEE Sensors J. **1** (2001) p. 41.
- [9] D. De Rossi, A. Della Santa, A. Mazzoldi, Mater. Sci. Eng. C, **7** (1999) p. 31.
- [10] F. Lorussi, W. Rocchia, E. P. Scilingo, A. Tognetti, D. De Rossi, IEEE Sensors J. **4** (2004) p. 807.
- [11] Proceedings of 3rd IEEE-EMBS International Summer School and Symposium on Medical Devices and Biosensors, MIT, Boston, USA (2006).

Chapter 7

7 Conclusions

This work showed that it is possible to deposit $\mu\text{c-Si:H}$ and a-Si:H thin films on low temperature plastics at high deposition rates, while keeping up the electronic quality for application in flexible thin-film silicon solar cells and other devices.

Flexible single junction solar cells were successfully fabricated on transparent (PEN) and opaque (PI) plastic substrates at low temperatures of 150°C for PEN and 200°C for PI. The p-i-n superstrate configuration was used for solar cells on PEN and efficiencies of $\sim 5\%$ were achieved. In the case of PI, solar cell efficiencies of around 7.5% were obtained using n-i-p substrate configuration. Different light trapping strategies were developed for transparent and opaque substrates. Laser texturing of PET substrates was studied and wet-chemical etching of the TCO back contact was applied for solar cells on PI.

Also, flexible piezoresistive sensors with high gauge factor have been fabricated on very thin ($15\ \mu\text{m}$) PI films and on thicker ones ($125\ \mu\text{m}$). These $15\ \mu\text{m}$ sensors were transferred to large area surfaces and incorporated in textiles in an attempt of a smart textile prototype. The main conclusions of this thesis are summarized in the following paragraphs.

7.1 High-rate deposition of silicon thin films on plastics

The deposition rate of both $\mu\text{c-Si:H}$ and a-Si:H thin films can be increased consistently by: 1) decreasing the inter electrode distance, 2) increasing the deposition pressure, and 3) increasing the rf-power. The deposition rate decreases as the HD increases in all deposition conditions. For each pressure and rf-power used, there is a

value of hydrogen dilution of silane for which the films undergo an amorphous-to-microcrystalline phase transition. The exact concentration of H_2 required for this transition to occur is a function of the deposition parameters and it increases when the working pressure increases, keeping other parameters constant. The films deposited at 6 Torr and 20 W had the highest microcrystalline deposition rate ($r_d = 0.38$ nm/s). The films with high photosensitivity ($>10^5$) are amorphous. The best $\mu\text{-Si:H}$ had photosensitivity around 10^2 . The best mixed phase film was obtained at 6 Torr, 20 W and had photosensitivity in excess of 10^3 . n- and p-type $\mu\text{-Si:H}$ films were obtained with $\sigma_{dk} = 7.8$ and $0.87 \Omega^{-1}\text{cm}^{-1}$, respectively. At 6 Torr, it was not possible to obtain highly doped microcrystalline films. n-type conductivity was $10^{-3} \Omega^{-1}\text{cm}^{-1}$ while p-type $\sigma_{dk} = 5 \times 10^{-7} \Omega^{-1}\text{cm}^{-1}$.

7.2 Flexible thin film silicon solar cells

Flexible amorphous superstrate p-i-n solar cells were fabricated on PEN with efficiencies of ~4.5 - 5%, and substrate n-i-p solar cells on PI with efficiencies of ~6 - 6.5%. In both cases, texturing schemes for light trapping were absent and the efficiencies were limited by low current-densities and low fill factors, with high series resistances.

Microcrystalline single-junction n-i-p thin film silicon solar cells on flexible smooth polyimide substrate showed similar behavior in terms of performance parameters in comparison to cells deposited on smooth glass. The V_{oc} was around 20-40 mV lower for the cells on PI, which is related to higher *i*-layer crystallinity of cells on PI. A textured ZnO:Ga layer was developed to promote light trapping in the solar cells on PI that yield more than 23 mA/cm^2 on absorbers of $1.8 \mu\text{m}$ thickness with cell efficiencies of up to 7.5%.

Laser texturing of plastic substrates increased dramatically the scattered transmittance (from 1.5 to >40%) and scattered reflectance (from 3 to 30%). However, the total transmittance and total reflectance decreased markedly in both cases.

7.3 Flexible $\mu\text{c-Si:H}$ piezoresistive sensors

High-gauge factor ($GF = -32.2$) piezoresistive n-type sensors were fabricated using flexible thin-film silicon technology on plastic. 15 μm -thick membrane sensors were batch fabricated and successfully transferred to large-area surfaces. This concept allows to add sensing capabilities to many different materials and surfaces, namely to textiles. The sensor's output voltage using quarter-, half, and full-bridge configurations were dynamically tested and the results follow the predictions made by circuit analysis for conventional, rigid sensors. Nine sensors were incorporated in fabrics and interconnected using machine sewed conductive threads. Their response to a random distributed load was registered. Microresistors, with $GF = -28.1$, were fabricated on plastic substrates using standard lithographic techniques.